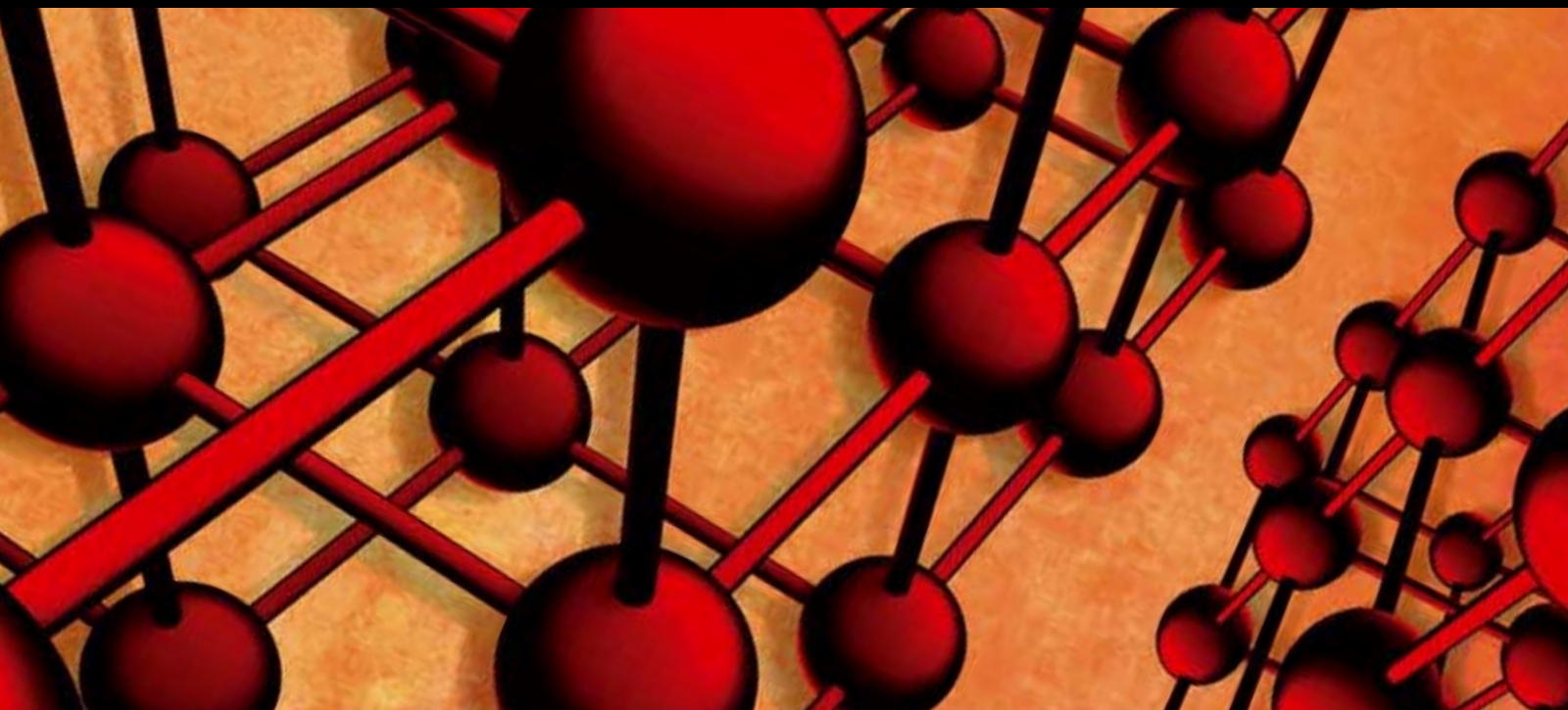


Advances in Materials Science and Engineering

# Advances in Metallic Materials Processing

Guest Editors: Jyotsna Dutta Majumdar, Igor Smurov, Shoujin Sun, and Indranil Manna





---

# **Advances in Metallic Materials Processing**

Advances in Materials Science and Engineering

---

## **Advances in Metallic Materials Processing**

Guest Editors: Jyotsna Dutta Majumdar, Igor Smurov,  
Shoujin Sun, and Indranil Manna



---

Copyright © 2011 Hindawi Publishing Corporation. All rights reserved.

This is a special issue published in volume 2011 of “Advances in Materials Science and Engineering.” All articles are open access articles distributed under the Creative Commons Attribution License, which permits unrestricted use, distribution, and reproduction in any medium, provided the original work is properly cited.

## Editorial Board

Marcel Ausloos, Belgium  
Robert S. Averbach, USA  
V. P. S. Awana, India  
Amit Bandyopadhyay, USA  
Z. Barber, UK  
Mark Blamire, UK  
Susmita Bose, USA  
Steve Bull, UK  
David Cann, USA  
Daolun Chen, Canada  
Manish U. Chhowalla, USA  
Paolo Colombo, Italy  
Martin Crimp, USA  
Jie Dai, Singapore  
C. K. Das, India  
Chris Davies, Australia  
J. Paulo Davim, Portugal  
Seshu Babu Desu, USA  
Yong Ding, USA  
Jianwen Ding, China  
Shi Xue Dou, Australia  
Chunying Duan, China  
Nadia El-Masry, USA  
David Field, USA  
Qiang Fu, China  
John W. Gillespie, USA  
Jeffrey T. Glass, USA  
Zhennan Gu, China  
Hiroki Habazaki, Japan

Richard Hennig, USA  
Dachamir Hotza, Brazil  
Chun-Hway Hsueh, USA  
Rui Huang, USA  
Shyh-Chin Huang, Taiwan  
Jacques Huot, Canada  
Hamlin Jennings, USA  
William A. Jesser, USA  
A. Jorio, Brazil  
Kazuro Kageyama, Japan  
S. Komarneni, USA  
Prashant Kumta, USA  
Pearl Lee-Sullivan, Canada  
Pavel Lejcek, Czech Republic  
Markku Leskela, Finland  
Jing Li, USA  
Jun Li, Singapore  
Yuanhua Lin, China  
Meilin Liu, Georgia  
Zhimin Liu, China  
M. A. Loi, The Netherlands  
Hai Lu, China  
Yiu-Wing Mai, Australia  
Peter Majewski, Australia  
A. S. H. Makhlof, Germany  
R. S. Mishra, USA  
S. Miyazaki, Japan  
Paul Munroe, Australia  
Korukonda Linga Murty, USA

Luigi Nicolais, Italy  
Tsutomu Ohzuku, Japan  
Xiaoqing Pan, USA  
Ganapathiraman Ramanath, USA  
Raju V. Ramanujan, Singapore  
Jainagesh A. Sekhar, USA  
You Song, China  
Charles C. Sorrell, Australia  
Steven L. Suib, USA  
Wen-Hua Sun, China  
Sam-Shajing Sun, USA  
Achim Trampert, Germany  
An Pang Tsai, Japan  
Vladimir Tsukruk, USA  
Krystyn Van Vliet, USA  
Stan Veprek, Germany  
Rui Vilar, Portugal  
Lianzhou Wang, Australia  
Kunpeng Wang, China  
John Wang, Singapore  
Jörg M. K. Wiezorek, USA  
Aiguo Xu, China  
Jenn-Ming Yang, USA  
Yadong Yin, USA  
Jihong Yu, China  
Guan-Jun Zhang, China  
Dao Hua Zhang, Singapore  
Ming-Xing Zhang, Australia

# Contents

**Advances in Metallic Materials Processing**, Jyotsna Dutta Majumdar, Igor Smurov, Shoujin Sun, and Indranil Manna  
Volume 2011, Article ID 180623, 2 pages

**Synthesis and Characterization of High-Entropy Alloy  $Al_xFeCoNiCuCr$  by Laser Cladding**, Xiaoyang Ye, Mingxing Ma, Wenjin Liu, Lin Li, Minlin Zhong, Yuanxun Liu, and Qiwen Wu  
Volume 2011, Article ID 485942, 7 pages

**Metallurgical Aspects of Laser Surface Processing of PM Cr-V Ledeburitic Steel**, Peter Jurči, Jiří Cejp, and Jan Brajer  
Volume 2011, Article ID 563410, 8 pages

**Influence of Welding Parameters on Weld Formation and Microstructure of Dual-Laser Beams Welded T-Joint of Aluminum Alloy**, Min Li, Zhuguo Li, Yong Zhao, Hao Li, Yuhua Wang, and Jian Huang  
Volume 2011, Article ID 767260, 6 pages

**Direct Laser Cladding of Cobalt on Ti-6Al-4V with a Compositionally Graded Interface**, Jyotsna Dutta Majumdar  
Volume 2011, Article ID 509017, 4 pages

**Precise Hole Drilling in PMMA Using 1064 nm Diode Laser CNC Machine**, Jinan A. Abdulnabi, Thaier A. Tawfiq, Anwaar A. Al-Dergazly, Ziad A. Taha, and Khalil I. Hajim  
Volume 2011, Article ID 137407, 5 pages

**The Fabrication of Automobile Components by Applying Electromagnetic Stirring in Semisolid Process**, H. H. Kim and C. G. Kang  
Volume 2011, Article ID 232640, 12 pages

**Industrial Semi-Solid Rheocasting of Aluminum A356 Brake Calipers**, U. A. Curle, J. D. Wilkins, and G. Govender  
Volume 2011, Article ID 195406, 5 pages

**The Influence of Prior Natural Aging on the Subsequent Artificial Aging Response of Aluminium Alloy A356 with Respective Globular and Dendritic Microstructures**, Heinrich Möller, Gonasagren Govender, Pierre Rossouw, and Waldo Stumpf  
Volume 2011, Article ID 375150, 6 pages

## Editorial

# Advances in Metallic Materials Processing

**Jyotsna Dutta Majumdar,<sup>1</sup> Igor Smurov,<sup>2</sup> Shoujin Sun,<sup>3</sup> and Indranil Manna<sup>1,4</sup>**

<sup>1</sup> Department of Metallurgical and Materials Engineering, Indian Institute of Technology, Kharagpur 721302, West Bengal, India

<sup>2</sup> Laboratory of Diagnostics and Engineering of Industrial Processes (DIPI Lab), Ecole Nationale d'Ingénieurs de Saint-Etienne (ENISE), 58 rue Jean Parot, 42023 Saint-Etienne, France

<sup>3</sup> Faculty of Engineering and Industrial Sciences, Swinburne University of Technology, Melbourne, VIC 3122, Australia

<sup>4</sup> Central Glass and Ceramic Research Institute, 196 Raja SC Malik Road, Kolkata 700032, India

Correspondence should be addressed to Jyotsna Dutta Majumdar, jyotsna@metal.iitkgp.ernet.in

Received 20 July 2011; Accepted 20 July 2011

Copyright © 2011 Jyotsna Dutta Majumdar et al. This is an open access article distributed under the Creative Commons Attribution License, which permits unrestricted use, distribution, and reproduction in any medium, provided the original work is properly cited.

Besides chemistry, processing route influences the microstructures and properties of metallic materials significantly. The emerging processing (fabrication) routes capable of tailoring the microstructures and hence properties of metallic materials include semisolid processing, spray forming, melt spinning, and laser materials processing. Although the present issue was initially proposed to present the articles based on all novel processing routes and its status on understanding the properties of materials, however, the topics and papers are not extensive representation of all the areas of advanced metallic materials processing. Furthermore, advanced processing of nonmetallic materials like polymeric materials is also included in the special issue. The special issue contains eight papers, out of them three articles present research works related to semisolid processing and five contributions on laser materials processing including one on processing of polymeric materials. The contributions from the authors who have expertise in different areas of materials processing are gratefully acknowledged. Needless to mention that without the time and efforts spent by the reviewers, the special issue would not have been presented in this form. The prompt reply and reminder by Ms. Doaa Shokry, Hindwai Publishers, is gratefully acknowledged.

Laser materials processing is a promising route, where a high-power laser beam is used as a source of heat for processing of materials. Faster processing speed, refinement and homogenization of microstructure, narrow heat affected zone, and processing of any materials are the notable advantages associated with laser materials processing. The first five articles are based on application of laser materials processing for the development of novel materials.

Laser surface cladding involves melting of clad material coating using laser beam and applying it on the surface with a minimum dilution at the interface. The first paper is on “Synthesis and characterization of high-entropy alloy AlXFeCoNiCuCr by laser cladding” by X. Ye et al. presented development of high entropy alloy (AlXFeCoNiCuCr) coating on AISI 1045 steel substrate by laser surface cladding technique. The characteristics of the clad layer in terms of microstructure, chemical composition and constituent phases are reported. The clad layers exhibited higher hardness at higher Al atomic content. AlFeCoNiCuCr clad layer also exhibited increased high temperature (400°C–700°C) hardness.

Laser surface melting is a promising technique in improving the hardness, wear and corrosion resistance of surface by grain refinement and homogenization of microstructure. The second paper entitled “Metallurgical aspects of laser surface processing of PM Cr-V ledeburitic steel” by P. Jurči et al. reported on laser surface melting of Vanadis 6 ledeburitic steel. Laser surface melting and subsequent rapid solidifying led to softening of the material due to the presence of retained austenite which could be improved by subsequent tempering which was concluded to be a challenge for the future investigations. The mechanism of melting and solidification was presented in details.

Laser-assisted welding offers the advantages of development of weld zone with improved properties and flexibility in welding of a wide varieties of materials including dissimilar materials. The third paper concerns “Influence of welding parameters on weld formation and microstructure of dual laser beams welded T-joint of aluminum alloy” by M. Li

et al. In this paper, a detailed investigations of the effect of the distance between two laser beams ( $d$ ), welding speed ( $v$ ), laser power ( $P$ ), and the laser beam offset toward the stringer (BOF) on the weld appearance, microstructure, and hardness of the 1.8 mm thick 6061 aluminum alloy plates in T-joint configuration has been undertaken using dual lasers. It was observed that at the optimized parameters, the welded T-joint showed good weld appearance without macrodefects; the microhardness of welds ranged from 75 to 85 HV<sub>0.3</sub>, and the tensile strength was about 254 MPa with the fracture at the heat affected zone (HAZ) on the stringer side.

Direct laser cladding involves building the near net shape component by laser melting of materials in the form of powder or wire and its subsequent application on a dummy substrate in a layer by layer fashion. In the fourth paper, application of DLD on the development of compositionally graded hip and femoral coupons with the cobalt ball on Ti-6Al-4V femoral with a graded interface has been attempted using a continuous wave CO<sub>2</sub> laser. Graded interface was developed by depositing a thin copper layer on Ti-6Al-4V substrate prior to multiple laser cladding of cobalt on it. Presence of copper interlayer was found to suppress the formation of brittle intermetallics of Ti and Co. The effect of process parameters on the microstructures, compositions and phases of the interface was studied in detail. Finally, the mechanical and electrochemical properties of the interface processed under optimum process parameters are reported.

The fifth paper on "Precise hole drilling in PMMA using 1064 nm diode laser CNC machine" by J. A. Abdalnabi et al. presented in brief the laser hole drilling of polymethylmethacrylate (PMMA) of 2.5 mm thickness using 1064 nm diode laser of 5 W output power. The effect of laser parameters on the drilling quality was investigated and supported by the predicted results of the analytical model.

Semisolid metal (SSM) processing is a unique manufacturing technique to fabricate near-net shape products for a variety of industrial applications. The objective is to achieve a semisolid structure which is free of dendrites and with the solid present in a near spherical form. In the present issue, three articles are presented on processing of materials by semisolid processing.

Application of electromagnetic stirring (EMS) is capable of modifying the microstructure of alloy before or during the forming process. In the sixth paper, H. H. Kim and C. G. Kang reported on "The fabrication of automobile components by applying electromagnetic stirring in semisolid process". In this article, the effect of electromagnetic stirring on the microstructure and properties of rheocasted A356 aluminum alloy was investigated in detail. It was observed that a significant improvement in mechanical property was achieved in the final product.

In the seventh paper, U. A. Curle et al. presented the a detailed description of industrial semisolid casting trials of aluminum A356 brake calipers in the paper entitled "Industrial semisolid rheocasting of aluminum A356 brake calipers". The process stability was determined by consecutive visual pass castings and determining the common defects between trials by X-ray examination and pressure testing of

heat treated castings from the consecutive visual passed castings.

In the last paper of the special issue "The influence of prior natural aging on the subsequent artificial aging response of aluminium alloy A356 with respective globular and dendritic microstructures", H. Möller et al. presented an interesting observation on the effect of microstructural change associated with semisolid processing on its heat treatment behavior and its difference with the same for dendritic microstructure. In this paper, the influence of prior natural aging on the subsequent artificial aging response of aluminium alloy A356 with respective globular and dendritic microstructures has been described. It was concluded that the differences in microstructures (globular or dendritic) do not have a noteworthy effect on the heat treatment response. It is also shown that composition plays a major role in determining hardness regardless of the casting technique used.

In conclusion, it may be stated that all the articles in the present issue present original research efforts on advanced field of materials processing, especially on laser materials processing and rheocasting and would motivate the readers to consider research problem in this directions. Finally, we wish the issue to be a successful, popular, and useful one to the engineers, scientists, and researchers in the field of materials science and manufacturing technology.

*Jyotsna Dutta Majumdar  
Igor Smurov  
Shoujin Sun  
Indranil Manna*

## Research Article

# Synthesis and Characterization of High-Entropy Alloy $Al_xFeCoNiCuCr$ by Laser Cladding

Xiaoyang Ye,<sup>1</sup> Mingxing Ma,<sup>1</sup> Wenjin Liu,<sup>1</sup> Lin Li,<sup>1,2</sup> Minlin Zhong,<sup>1</sup>  
Yuanxun Liu,<sup>1</sup> and Qiwen Wu<sup>1</sup>

<sup>1</sup>Key Laboratory for Advanced Materials Processing Technology Ministry of Education, Department of Mechanical Engineering, Tsinghua University, Beijing 100084, China

<sup>2</sup>Laser Processing Research Centre, School of Mechanical, Aerospace and Civil Engineering, The University of Manchester, Manchester M13 9PL, UK

Correspondence should be addressed to Mingxing Ma, [mmx.thudme@gmail.com](mailto:mmx.thudme@gmail.com)

Received 31 August 2010; Accepted 22 December 2010

Academic Editor: J. Dutta Majumdar

Copyright © 2011 Xiaoyang Ye et al. This is an open access article distributed under the Creative Commons Attribution License, which permits unrestricted use, distribution, and reproduction in any medium, provided the original work is properly cited.

High-entropy alloys have been recently found to have novel microstructures and unique properties. In this study, a novel  $Al_xFeCoNiCuCr$  high-entropy alloy was prepared by laser cladding. The microstructure, chemical composition, and constituent phases of the synthesized alloy were characterized by SEM, EDS, XRD, and TEM, respectively. High-temperature hardness was also evaluated. Experimental results demonstrate that the  $Al_xFeCoNiCuCr$  clad layer is composed of only BCC and FCC phases. The clad layers exhibit higher hardness at higher Al atomic content. The  $AlFeCoNiCuCr$  clad layer exhibits increased hardness at temperature between 400–700°C.

## 1. Introduction

The component of an alloy system is usually based on one principle element and some additional elements for a superior performance. It makes use of the edge component region in the phase diagrams. The traditional view holds that although it is helpful to add a small amount of alloying elements for better performance, a large quantity of the additional alloying elements should be avoided. In some of the common traditional alloys such as aluminum alloy and nickel or titanium alloys, the main elements usually take up more than 50% atomic content.

The widely used ferroalloys suffer a fall of hardness when they are tempered at 350–550°C, which limits the possible applications in high-temperature environments [1]. The high-temperature precipitate strengthened nickel-base super alloys, which are widely applied in the aviation industry, also suffer from the same problem, although to a lesser degree. The multiphase bulk metallic glasses crystallize at 400–600°C, which also limits the application in high temperature [2]. Poor performance in high temperature restricts the application of traditional alloys.

As discussed above, the traditional way of designing an alloy restricts the development of alloy systems for high-temperature and extreme-loading applications. The introduction of the high-entropy alloys (HEA) concept by Yeh et al. [3] broke up the traditional rule that the main elements take up more than 50% atomic content. HEA means that alloys are composed of multielements and each takes up a relatively high but less than 35% of atomic content. The properties of this innovative alloy are decided by the combined action of multielements. Previous research demonstrates that the high-entropy alloy tends to form simple crystallization phase disorderly, even nanophase or amorphous phase. At the same time, by controlling the composition, it is possible to achieve high-hardness and high-abrasion performance at high temperatures [4].

Vacuum arc remelting [5–9] for bulk cast ingot is the primary method to synthesize HEAs. Surface coating is also possible. Varalakshmi et al. [10] synthesized the  $AlFeTiCrZnCu$  by mechanical alloying. However, these methods can hardly be directly applied for the surface modification. By ball milling followed by cladding on the surface, the alloy powder can be used for surface modification indirectly.

The bulk-processing route can be costly and is limited to the production of relatively small components. However, in many situations, only the contact surface properties are important in determining performance of the component in practical applications. Therefore, the use of a coating has several attractive advantages.

In this paper, a novel method to fabricate the HEA coatings by laser cladding is reported. Due to rapid heating and cooling in the laser cladding process, the cooling rate of laser cladding can reach  $10^3$ – $10^6$  K/s. More importantly, laser cladding has the capability of achieving a controllable dilution ratio, metallurgical bonding between the coating and the substrate, small thermal deformation, and nonequilibrium reaction. Considering HEA's tendency to form simple structures and nanocrystallines, fabricating HEA by laser cladding is of great significance and potential for extensive use. Until now, this new method has not been reported elsewhere. The objective of the investigation is to ascertain the feasibility of fabricating HEA by laser cladding and achieve alloy coatings with good combination properties, with an emphasis on high-temperature hardness.

## 2. Experimental Procedures

Al, Co, Cr, Ni, Cu, and Fe powders of high purity are prepared and well mixed as the raw material. Before the above powder material is preplaced on an AISI 1045 steel substrate, the mixed powders are added with ethanol and mixed uniformly. The thickness of the precoated powder layers was restricted to approximately 1.4 mm. When the thickness is as large as the 1.6 mm, the number and length of the cracks will increase sharply. However, when the thickness is as small as 1.0 mm, it is difficult to obtain the approximate dilution rate by controlling the laser parameters. With a PRC-3000 CO<sub>2</sub> laser equipment, in the argon environment, the HEA was synthesized on the surface of AISI 1045 steel. The performance of the cladding coatings are controlled by the laser power and scanning speed, and the spot diameter is fixed to 3 mm. Several different values of laser power were used for laser cladding: 1200 W to 2000 W. The scanning speed is among 2 mm/s–12 mm/s.

It has been reported that Al has a significant influence on the structure and properties [11]. In order to evaluate the influence of Al content in Al<sub>X</sub>FeCoNiCuCr coatings by laser cladding, the X factor was set as another variable quantity and the experiments were divided into 5 groups: X = 1, 1.3, 1.5, 1.8, and 2.0. All the elements except Al are equiatomic. After the laser cladding, the specimens were sectioned perpendicular to the scanning track with a wire-EDM machine. The specimens were analyzed by a D8 Advance X-ray Diffraction analysis system (XRD). The chemical composition of the cladding was determined by an Oxford INCA X-sight 7573 Energy Dispersive X-ray (EDX) microanalysis system equipped with JSM-6460LV Scanning Electron Microscope (SEM). The crystal structure of the cladding layers were analyzed by JEOL-JEM-2010 transmission electron microscope (TEM). The microhardness was measured with an HX-200 Vickers Hardness Tester and

the high-temperature microhardness was measured at 200–800°C with an AKASHI AVK-A High-Temperature Micro Hardness Tester.

## 3. Results and Discussion

*3.1. Synthesis of High-Entropy Alloys.* By optimizing the laser parameters, porosity-free alloy coatings were synthesized by laser cladding. The optimal ranges of laser powers and scanning speeds for better dilution rate are among 1400–1800 W and 8–12 mm/s, respectively. Figure 1 shows the macroscopic appearance of coatings. Cracks were avoided when the X values are under 1.5. The coating shows no visible defects in macroscopic views. With the further addition of Al element and the X factor reaching 1.8, some cracks in small number were observed on the coatings. When X reaches 2.0, the number of cracks increases sharply. The sharply elongated cracks run through the cladding layers. The existence of cracks would lead to adverse impacts to the performance of the cladding layers.

*3.2. The Microstructure and Compositional Characteristics of Al<sub>X</sub>FeCoNiCuCr.* The SEM pictures in Figure 2 show the typical central area of the Al<sub>X</sub>FeCoNiCuCr structures. The typical structures are composed of both dendritic (DR) and interdendritic (ID) areas. Table 1 shows the atomic composition of both DR and ID.

From Table 1, it can be seen that the actual composition percentage of Fe element is much larger than the nominal one. The possible reason is that some of the Fe element of AISI 1045 steel base dilutes the clad, which results in the deviation from the nominal percentage. Experimental results show that the deviation of Fe elements grew bigger with higher laser power and lower scanning speed. For instance, at 1800 W and 4 mm/s, the atomic percentage of Fe can reach as high as 50%.

The deviation from nominal composition of Al element, indicates that there is a possibility of vaporization of Al during laser cladding. Another possible reason is the selective corrosion of aqua regia. If the corrosion resistance of the Al-enriched phase is poorer than others, this phase would be selectively corroded into interdendritic structure. This situation could also result in the deviation of Al composition.

It was reported that the Cu element could be enriched in the interdendritic structure [10, 11]. The atomic percentage of Cu element would be up to more than 50%. However, laser cladding synthesized Al<sub>X</sub>FeCoNiCuCr alloys appear little dendrite segregation between the ID and DR structures. Although the dendrite segregation does occur between the ID and DR, it is not as severe as in casting alloys. The high cooling rate character of laser cladding may explain this phenomenon. In normal situation, with a lower cooling rate, the segregation is more significant. When the cooling rate rises to a certain level, the interdendritic segregation diminishes. This is when the cooling speed reaches a threshold level, then the diffusion process is inhibited in both the solid and liquid phases. Under this condition, the alloy comes into a situation of diffusionless crystallization, similar

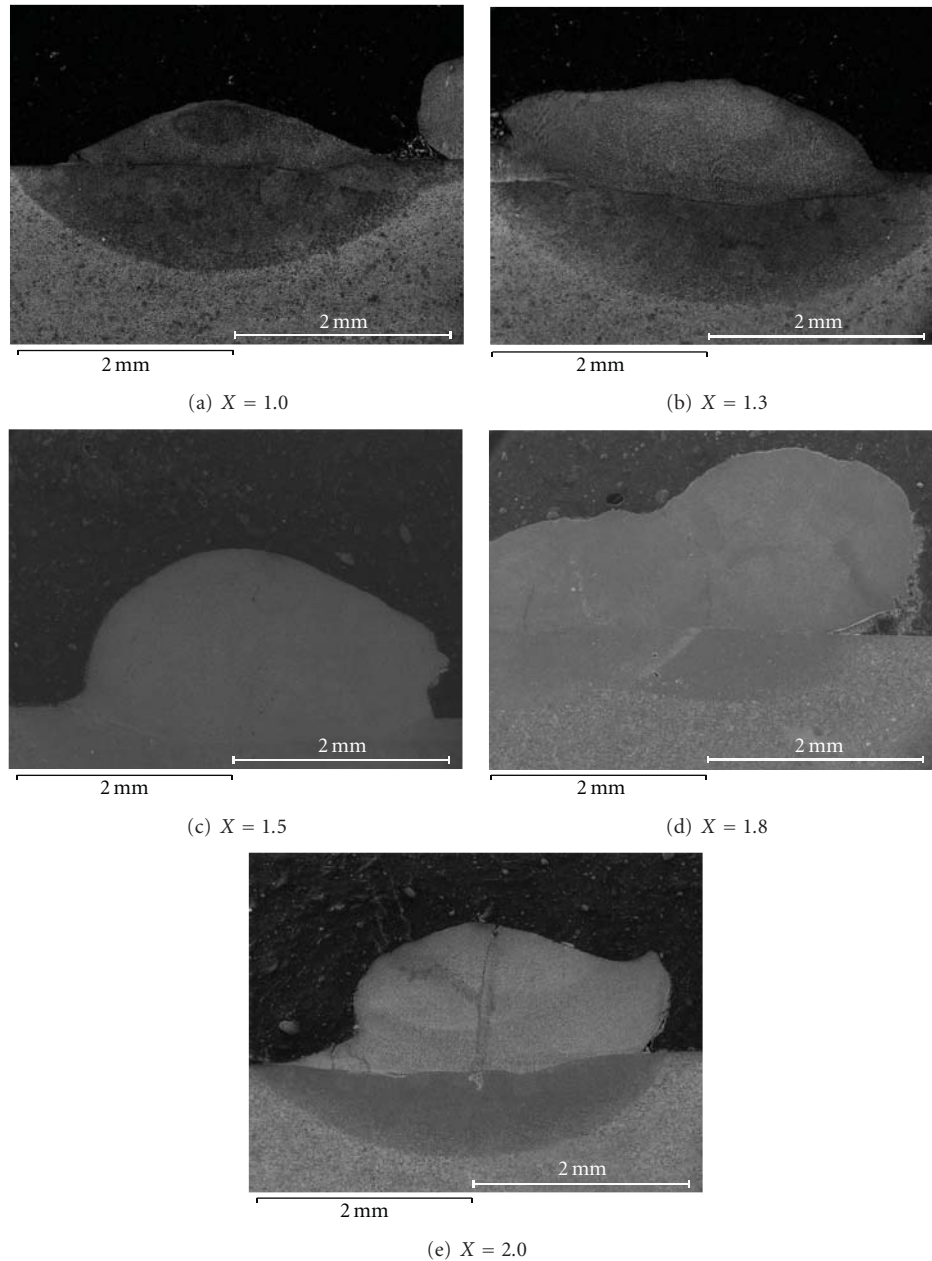


FIGURE 1: Macroscopic SEM figures of Al<sub>x</sub>FeCoNiCuCr High-entropy alloys under different X values at (a) X = 1, (b) X = 1.3, (c) X = 1.5, (d) X = 1.8, and (e) X = 2.0.

to the solidification process of a pure metal. Hence, the interdendritic segregation in the HEA synthesized by laser cladding should be smaller than that synthesized by casting. Interdendritic segregation usually causes adverse impacts on the alloy's performance, especially on the plasticity and toughness. From the above results, it is expected that alloys fabricated by laser cladding should have better performance than casting ones.

**3.3. The Phase Characteristics and the Influence of the Al Contents.** The work shows that the atomic content of the Al element has a great influence on the phase composition

of HEA Al<sub>x</sub>FeCoNiCuCr. Experimental samples with an X factor at 1.0, 1.3, 1.5, 1.8, and 2.0 were characterized using XRD and TEM to understand the phase transitions.

**3.3.1. X-Ray Diffraction Analysis.** Figure 3 shows the X-ray Diffraction patterns of Al<sub>x</sub>FeCoNiCuCr under different X values. The diffraction peaks show that the complex intermetallic compounds are merged into simple phases. Al<sub>x</sub>FeCoNiCuCr synthesized by vacuum arc remelting and mechanical alloying are both composed of simple phases [11, 12].

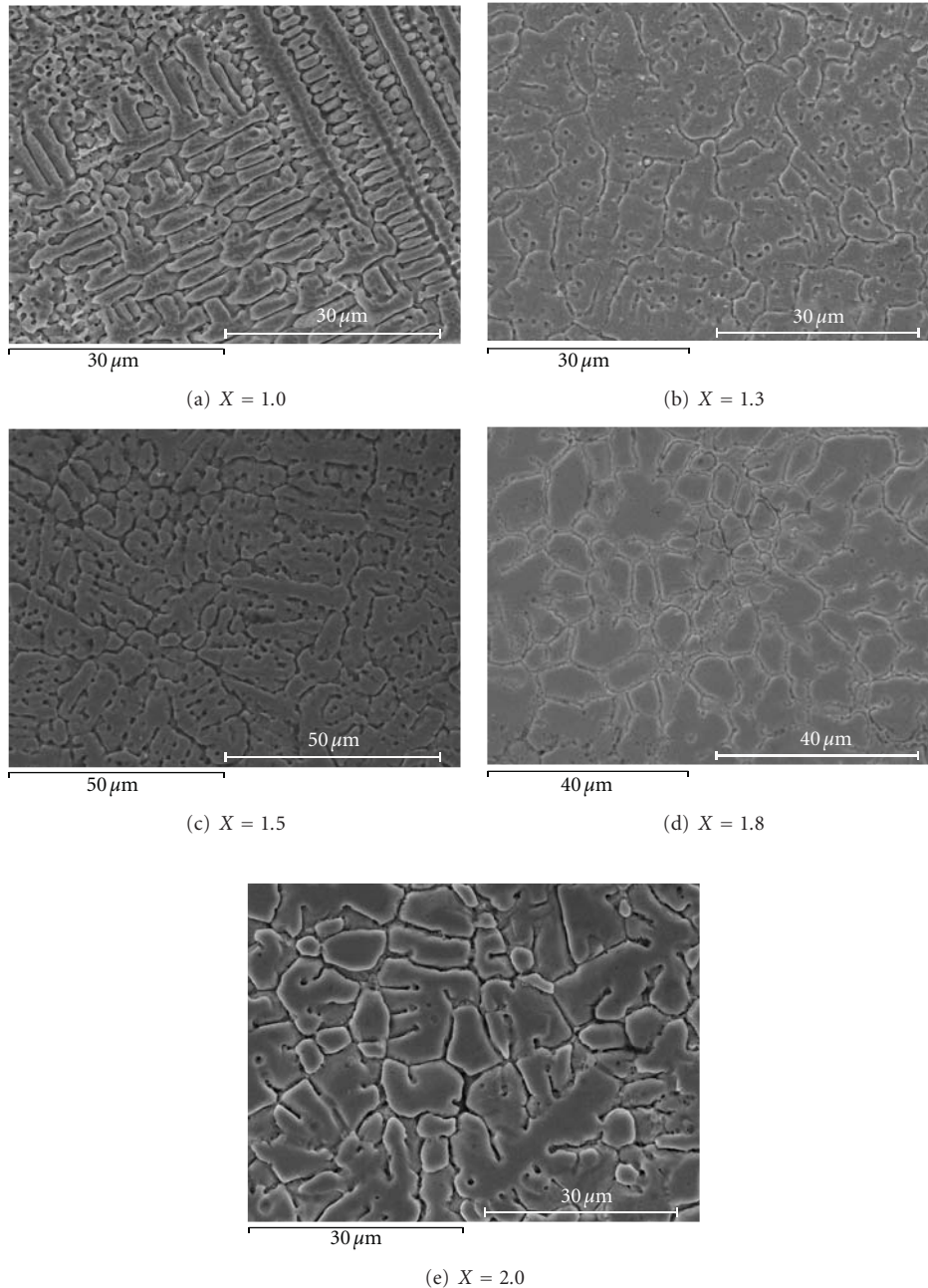


FIGURE 2: Typical microstructure of  $Al_xFeCoNiCuCr$  clad layer, etching in aqua regia for a few minutes: (a)  $X = 1.0$ , (b)  $X = 1.3$ , (c)  $X = 1.5$ , (d)  $X = 1.8$ , and (e)  $X = 2.0$ .

The analysis shows that  $Al_xFeCoNiCuCr$  synthesized by laser cladding shares the same phase composition with the alloys fabricated by traditional methods. According to Figure 4, the addition of Al content does not change the number of phases. However, the relative intensity of the FCC diffraction peaks decrease and the BCC peaks increase. It can be inferred that there exists the transition from FCC phase to the BCC phase, accompanied with the addition of Al element. As Al obtains relatively bigger atomic radius, the addition of Al aggravates the lattice distortion. This phenomenon was also observed in previous research [12].

**3.3.2. The Transmission Electron Microscope Analysis of  $AlFeCoNiCuCr$ .** The nanocrystalline nature of the HEA  $AlFeCoNiCuCr$  has been confirmed from the TEM bright field image and the corresponding selected area diffraction (SAD) pattern shown in Figure 5.

We can learn that the alloy is composed of two distinct phases: Phase One appears as white spots and Phase Two as a black base. In (a), the microstructure investigation shows the granular Phase One is dispersed in the base of Phase Two. The result also proves the nonentity of the complex intermetallic compounds in the HEA prepared by laser

TABLE 1: The atomic composition and distribution in different X values.

Alloy	Zone	at%					
		Al	Cr	Fe	Co	Ni	Cu
$Al_{1.0}FeCoNiCuCr$	Nominal	16.66	16.66	16.66	16.66	16.66	16.66
	Actual	5.95	11.34	40.16	11.83	12.82	17.94
	DR	5.64	12.42	42.36	12.94	11.70	14.94
	ID	6.91	11.61	44.18	14.18	10.58	12.53
$Al_{1.3}FeCoNiCuCr$	Nominal	20.63	15.87	15.87	15.87	15.87	15.87
	Actual	14.84	16.28	23.93	15.68	15.71	13.46
	DR	15.29	17.47	25.63	17.71	14.20	9.71
	ID	16.46	16.97	21.67	14.22	16.16	14.53
$Al_{1.5}FeCoNiCuCr$	Nominal	23.08	15.38	15.38	15.38	15.38	15.38
	Actual	14.30	17.84	23.61	15.75	15.12	13.38
	DR	14.78	20.69	27.70	16.56	11.34	8.93
	ID	10.99	15.85	25.96	15.40	15.79	16.01
$Al_{1.8}FeCoNiCuCr$	Nominal	26.47	14.71	14.71	14.71	14.71	14.71
	Actual	20.99	14.92	16.36	16.28	14.65	16.80
	DR	19.10	15.66	22.73	17.89	14.53	10.10
	ID	20.41	14.73	18.57	13.81	16.66	15.82
$Al_{2.0}FeCoNiCuCr$	Nominal	28.57	14.29	14.29	14.29	14.29	14.29
	Actual	17.06	13.68	21.52	16.28	15.12	16.34
	DR	17.89	12.68	27.62	13.57	14.92	13.32
	ID	5.63	13.58	25.88	15.51	20.19	19.21

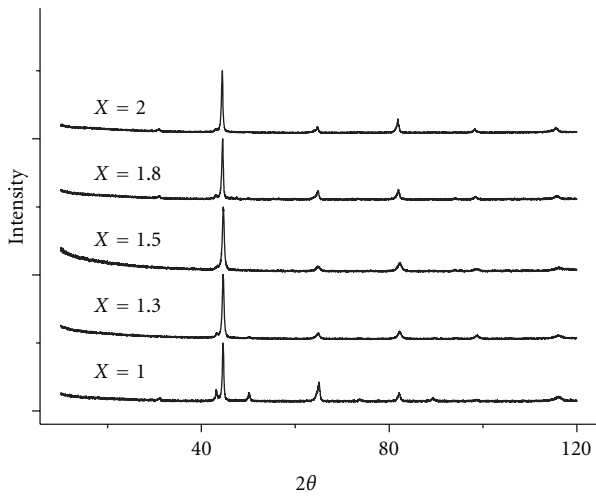


FIGURE 3: The X-ray Diffraction patterns.

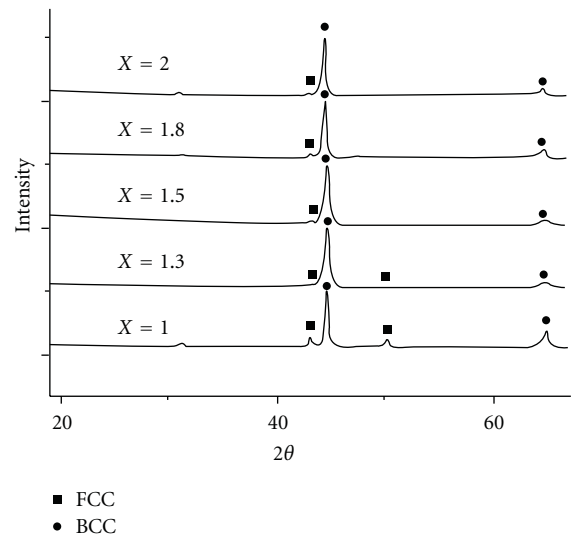


FIGURE 4: The detailed main diffraction peak of XRD.

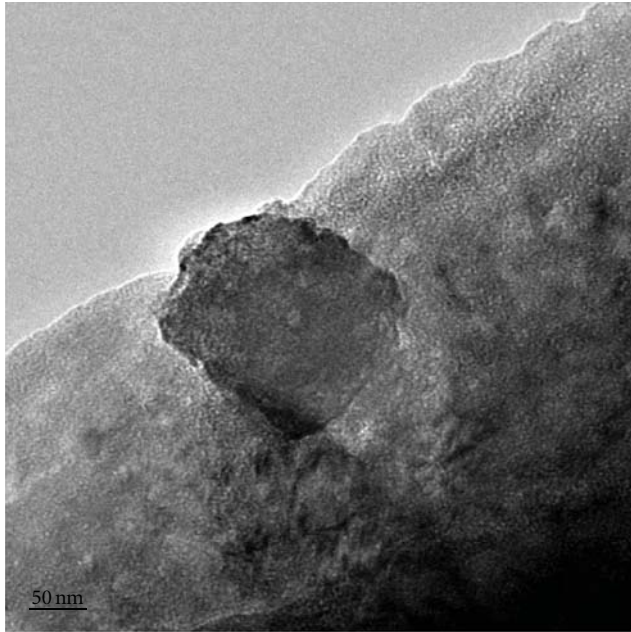
cladding. The Phase One is nanostructure, and the average diameter was between several nanometers to about 100 nm.

3.4. The Cladding Layer Microhardness Distribution of  $Al_XFeCoNiCuCr$ . For the cladding layers, the microhardness is a key performance index. It is also reported that the content of Al elements has a great influence on the hardness [12]. The microhardness distribution for different X values and the average hardness are shown, respectively, in Figure 6 and Table 2.

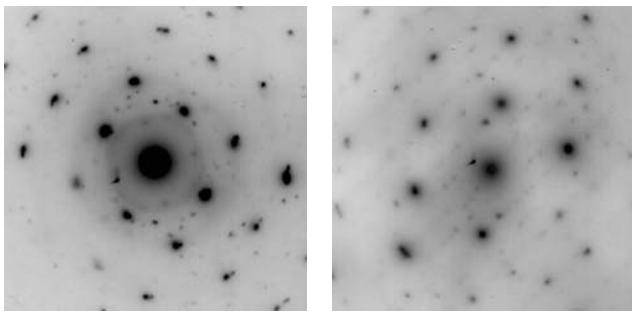
TABLE 2: The microhardness in different X values ( $HV_{0.2}$ ).

Al composition	X = 1.0	X = 1.3	X = 1.5	X = 1.8	X = 2.0
Average $HV_{0.2}$	390	540	640	660	687
Average HRC	40	52	58	58	60

The microhardness values for different X factors differ considerably. With the increase of X, the average microhardness across a section of the cladding layers (0–10 mm



(a)



(b)

(c)

FIGURE 5: The TEM image and SAD patterns. (a) Bright field image; (b) SAD pattern of [001] zone axis; (c) SAD pattern of BCC [012] zone axis.

in length) presents an increasing trend with the increases in the  $X$  factor. When the  $X$  value increases from 1 to 2, the average microhardness increases from 390 to 687  $HV_{0.2}$ . The content of Al significantly influences the microhardness. This result is in agreement with the reported research [11]. This phenomenon can be explained in the transition of lattice structure. As discussed above, the addition of Al promotes the transition from FCC to BCC structure. With the further addition, the BCC become the elementary phase, which results in a significant change of the microstructure. As the BCC structure is considered to obtain higher hardness than FCC [12], the microhardness would expect a sharp increase after this transition. In another aspect, for the bigger atomic ratio of Al, the atoms serve as a function of solution strengthening and aggravate the lattice distortion. Compared with the casting alloys, HEA synthesized by laser cladding obtains higher microhardness as a result of more rapid cooling which leads to finer microstructures.

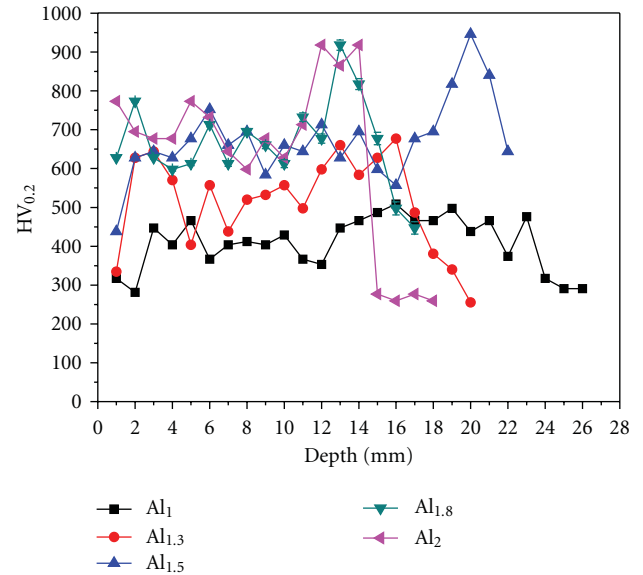


FIGURE 6: The microhardness distribution in different  $X$  values ( $X = 1, 1.3, 1.5, 1.8,$  and  $2.0$ ).

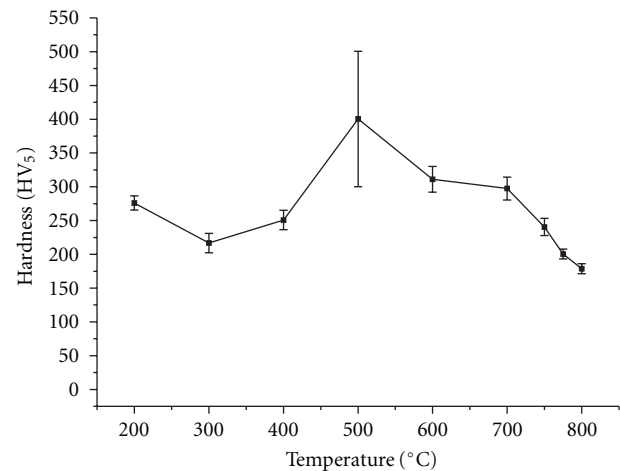


FIGURE 7: The high-temperature microhardness distribution.

From Table 2, it can be inferred that the increase of microhardness is sharp when the  $X$  increases from 1.0 to 1.5. With further addition of Al, the increasing rate of microhardness slows down because the initial addition of Al greatly change the phase structure and this effect diminishes gradually during further addition.

However, the addition of Al also results in the increasing of cracks. It is possible to seek a balanced  $X$  values in which lie the higher average microhardness and less defects. This optimal  $X$  lies between 1.5 and 1.8.

**3.5. High-Temperature Microhardness.** Previous research focuses on the microhardness change after tempering in different temperatures instead of the hardness in high-temperature situations. If HEA could remain a high hardness in high temperature, the possible applications could be

greatly increased. In this paper, we choose AlFeCoNiCuCr for the high-temperature hardness test. Figure 7 shows the microhardness of AlFeCoNiCuCr at different temperatures. Firstly, when the alloy was heated, there was an obvious fall of hardness. Most alloys would suffer from a fall of hardness when heated.

However, more importantly, as the temperature further increases to between 400°C and 500°C, the hardness has a sharp increase. Higher hardness than that at room temperature is shown for temperatures between 400°C and 700°C. This phenomenon shows that the AlFeCoNiCuCr alloy shares the same property as high-speed steel which also has an increasing hardness trend in certain temperature ranges. High-speed steel contains elements such as W, Mo, Cr, Co, and V, which can result in the carbide precipitation when tempering. Precipitation harden effect serve as harden mechanism. When it comes to HEA this phenomenon can be explained as the multialloying elements form intermetallic compounds of high thermostability and microhardness, which results in higher high temperature hardness at temperatures between 400–700°C. This property undoubtedly enhances the possible application in high-temperature situations. However, the hardness falls sharply at 600–800°C and finally reaches HV<sub>5,0</sub>150. This is far from the average hardness in room temperature. Both HEA and high-speed tool steel suffer from a hardness fall above about 600°C.

#### 4. Conclusion

High-entropy alloys Al<sub>X</sub>FeCoNiCuCr has been successfully in situ synthesized by laser cladding, and they are proved to obtain nanostructure. The following characteristics of the alloy have been found.

- (1) Optimal laser parameters of synthesizing Al<sub>X</sub>FeCoNiCuCr for suitable dilution ratio are 1400–1800 W and 8–12 mm/s.
- (2) The HEAs prepared by laser cladding have shown homogeneity in composition and have a crystallite size of about 10 nm.
- (3) Nanostructure with BCC and FCC crystal structure have been observed in all the compositions. The addition of Al element promotes the transition of FCC to BCC structure.
- (4) The composition of Al element is a key factor influencing the microhardness and forming of HEA. The alloy combines the relatively balanced forming and microhardness at the composition region where  $X = 1.5$  to  $X = 1.8$ .
- (5) The nanocrystalline high entropy alloy is stable even at 400–700°C and has a higher microhardness than that at room temperature. The hardness presents a sharp increase between 400°C and 500°C. However, reduced hardness at temperatures above 700°C was also observed.

#### Acknowledgments

The authors would like to thank Liang Lv for technical assistance in TEM experiments and Yu Gu and Changsheng Dong for processing the figures. X. Ye would like to acknowledge the financial support by Professor Wenjin Liu and Dr. Mingxing Ma.

#### References

- [1] C. W. Yao, J. Huang, P. L. Zhang, YI. X. Wu, and B. S. Xu, “Tempering softening of overlapping zones during multi-track laser quenching for carbon steel and alloy steel,” *Transactions of Materials and Heat Treatment*, vol. 30, no. 5, pp. 131–135, 2009.
- [2] K. B. Kim, P. J. Warren, and B. Cantor, “Structural relaxation and glass transition behavior of novel (Ti<sub>33</sub>Zr<sub>33</sub>Hf<sub>33</sub>)<sub>50</sub>(Ni<sub>50</sub>Cu<sub>50</sub>)<sub>40</sub>Al<sub>10</sub> alloy developed by equiatomic substitution,” *Journal of Non-Crystalline Solids*, vol. 353, no. 32–40, pp. 3338–3341, 2007.
- [3] J. W. Yeh, S. K. Chen, SU. J. Lin et al., “Nanostructured high-entropy alloys with multiple principal elements: novel alloy design concepts and outcomes,” *Advanced Engineering Materials*, vol. 6, no. 5, pp. 299–303, 2004.
- [4] A. Inoue, “Bulk amorphous alloys with soft and hard magnetic properties,” *Materials Science and Engineering A*, vol. 226–228, pp. 357–363, 1997.
- [5] F. J. Wang and Y. Zhang, “Effect of Co addition on crystal structure and mechanical properties of Ti<sub>0.5</sub>CrFeNiAlCo high entropy alloy,” *Materials Science and Engineering A*, vol. 496, no. 1–2, pp. 214–216, 2008.
- [6] Y. Zhang, Y. J. Zhou, J. P. Lin, G. L. Chen, and P. K. Liaw, “Solid-solution phase formation rules for multi-component alloys,” *Advanced Engineering Materials*, vol. 10, no. 6, pp. 534–538, 2008.
- [7] C. J. Tong, M. R. Chen, S. K. Chen et al., “Mechanical performance of the Al<sub>X</sub>CoCrCuFeNi high-entropy alloy system with multiprincipal elements,” *Metallurgical and Materials Transactions A*, vol. 36, no. 5, pp. 1263–1271, 2005.
- [8] C. J. Tong, Y. L. Chen, S. K. Chen et al., “Microstructure characterization of Al<sub>X</sub>CoCrCuFeNi high-entropy alloy system with multiprincipal elements,” *Metallurgical and Materials Transactions A*, vol. 36, no. 4, pp. 881–893, 2005.
- [9] B. S. Li, Y. P. Wang, M. X. Ren, C. Yang, and H. Z. Fu, “Effects of Mn, Ti and V on the microstructure and properties of AlCrFeCoNiCu high entropy alloy,” *Materials Science and Engineering A*, vol. 498, no. 1–2, pp. 482–486, 2008.
- [10] S. Varalakshmi, M. Kamaraj, and B. S. Murty, “Synthesis and characterization of nanocrystalline AlFeTiCrZnCu high entropy solid solution by mechanical alloying,” *Journal of Alloys and Compounds*, vol. 460, no. 1–2, pp. 253–257, 2008.
- [11] L. Yuan and C. Min, “Microstructure and solidification mode of AlTiFeNiCuCr<sub>X</sub> high-entropy alloy with multi-principal elements,” *Special Casting & Nonferrous Alloys*, no. S1, 2008.
- [12] Y. Liu, M. Chen, Y. Li, and X. Chen, “Microstructure and mechanical performance of Al<sub>X</sub>CoCrCuFeNi high-entropy alloys,” *Rare Metal Materials and Engineering*, vol. 38, no. 9, pp. 1602–1607, 2009.

## Research Article

# Metallurgical Aspects of Laser Surface Processing of PM Cr-V Ledeburitic Steel

**Peter Jurči, Jiří Cejp, and Jan Brajer**

*Faculty of Mechanical Engineering, Czech Technical University in Prague, Karlovo nám. 13, 121 35 Prague 2, Czech Republic*

Correspondence should be addressed to Peter Jurči, p.jurci@seznam.cz

Received 13 July 2010; Revised 23 November 2010; Accepted 6 December 2010

Academic Editor: J. Dutta Majumdar

Copyright © 2011 Peter Jurči et al. This is an open access article distributed under the Creative Commons Attribution License, which permits unrestricted use, distribution, and reproduction in any medium, provided the original work is properly cited.

The Vanadis 6 ledeburitic-type steel was laser surface remelted. Microstructural changes and hardness in laser affected material were investigated using light microscopy, SEM, and EDS-microanalysis. It was found that the laser surface melting and subsequent rapid solidifying led to softening of the material, due to presence of retained austenite. The melting of the material begins with the transformation of  $M_7C_3$ -carbide into a liquid and finishes via the dissolution of primary solid solution grains. The solidification proceeded in a reverse manner while the eutectics became often so-called degenerated form.

## 1. Introduction

Over the last three decades, the laser surface processing of metals became an important industrial technique used in variety of applications. High power densities delivered to the workpieces can produce fully austenitized or entirely melted and resolidified regions while the process of the treatment can be completed in few seconds [1].

Many laboratory examinations indicated that the laser surface melting can be a very promising technique in a variety of industrial applications. However, technical application of the laser surface melting is currently limited due to several causes. The first one is the economical aspect—mostly high initial costs for the laser equipment. The second problem is connected with the nature of common metallic materials used for the workpieces manufacturing. Since the material undergoes rapid heating and cooling during the laser thermal cycle, coarse structural constituents such as thick pearlitic lamellae or carbides and clusters can make serious obstacles in the results of treatment. Other important difficulty is connected with the applications, when multiple traces are needed to process larger surface areas. In these cases, annealing effects can take place in adjacent laser traces.

The laser surface melting of ledeburitic steels (Cr-, Cr-V-cold work tool steels, high speed steels) has been considered as a promising technique many years ago. It was

believed that the surface remelting can form a “refined as-cast microstructure” in thin near-surface region while the microstructure of the core material remains unaffected. Refined “as-cast microstructure”, as assumed, would more effectively withstand the degradation processes connected with the use of tools, like abrasive and adhesive wear, since it contains very hard carbides creating continuous networks. The core material, on the other hand, consists of the matrix with uniformly distributed fine carbide particles, which ensures an appropriate toughness of the steel.

Metallurgical aspects of laser surface melting of various ledeburitic steels were investigated by many authors. It has been found that for laser remelted M2-type high speed steel, refined dendritic or cellular morphology of primary phase is typical [1, 2]. In addition, our pioneer work [3] confirmed that the solidification of the material finishes by eutectic transformation. Based on the fact that the molten microvolume of the material undergoes the rapid solidification effect, eutectics often freeze irregularly, in a so-called “degenerated” manner. As reported elsewhere, the eutectics can also contain metastable and intermediate phases instead of stable carbides for given systems [4].

Typical cooling rates in laser surface melting were estimated to range between  $10^3$  and  $10^6$  Ks<sup>-1</sup>. Such a high cooling rate induces considerable alterations in the mechanism of crystallization. For most types of high speed steels, for



FIGURE 1: Specimen irradiated by laser.



FIGURE 2: Light micrograph showing the substrate material.

instance, the primary crystallization proceeds by peritectic reaction. As reported by Nizhnikowskaya [5], the peritectic reaction in high speed steels proceeds completely only when the cooling does not exceed  $10^3 \text{ K s}^{-1}$ . At higher cooling rates, the  $\delta$ -ferrite is conserved in the microstructure of solidified metal. This makes a considerable softening of the material, not only after remelting but also after tempering to the maximum of secondary hardness [6, 7]. Therefore, the high speed steels cannot be considered as suitable materials for the laser surface melting. Other negative aspects were published by Colaço and Vilar [8, 9]. They found out that the laser melted and rapidly resolidified material can contain a high portion of the retained austenite.

One can expect that the laser remelted materials would have generally increased hardness compared to conventionally quenched and tempered steel. The reason is that owing to the rapid solidification, extended solid solutions can be formed that can have a positive effect upon the hardness. For the ledeburitic steels, however, the situation seems to be more complex and a general statement on the behaviour of laser remelted and rapidly solidified materials does not exist. At least, above-mentioned changes in the mechanism of primary crystallization of high speed steels can influence the hardness negatively. Also the presence of the retained austenite has an undesirable effect upon the hardness. But, as found out by Colaço and Vilar [9], and independently also by the main author of this paper [10], the softening of the material due to the retained austenite can be completely eliminated by subsequent tempering if the alloy has an appropriate chemical composition.

The laser surface remelting of Cr-V ledeburitic steels, and its consequence upon the structure and properties was not investigated seriously yet. The goal of the paper is to provide

the first attempt on the evaluation of surface remelting upon an example of PM cold work tool steel Vanadis 6.

## 2. Experimental

The experimental material was the PM ledeburitic steel Vanadis 6 with nominally (in wt%) 2.1% C, 1.0% Si, 0.4% Mn, 6.8% Cr, 1.5% Mo, 5.4% V, and Fe as balance. As-received material after soft anneal had a hardness of 284 HV10. Plate-like specimens with 70 mm in length, 18 mm in width, and 8 mm in thickness were mechanically milled and fine ground to a final surface roughness  $R_a = 0.2 - 0.3 \mu\text{m}$ .

The specimens were then subjected to standard heat treatment. The heat procedure included the vacuum austenitizing up to final temperature of  $1050^\circ\text{C}$ , nitrogen gas quenching at 5 bars pressure and double tempering, each cycle at  $550^\circ\text{C}$  for 1 hour. After each tempering cycle, the material was air-cooled down to an ambient temperature. Resulting hardness of heat treated specimens was 700 HV 10.

Laser processing has been performed using the GSI LUMONICS 701H Nd:YAG-laser equipment, with the wavelength of the irradiation of 1064 nm, operating in a continuous regime. The standard output power of the laser was 450 W. The laser beam was focused to 50 mm over the specimen surface. The relative beam speed on the specimen's surface was 80 mm/min. Specimens were laser processed in a longitudinal direction, Figure 1.

Irradiated material was prepared for the microstructural analysis. Cross-sectional samples were ground, polished, and etched by 3% Nital reagent. Light and scanning electron microscopy (SEM) have been used for the investigations. The standard accelerating voltage of SEM was 15 kV for the microstructural investigations. For better understanding of the nature of structural constituents, also the energy-dispersive spectroscopy (EDS) analysis and mapping have been done. But, the acceleration voltage of SEM was strictly reduced to 1 kV, to avoid too deep penetration of electron beam, and to enable more accurate analysis.

Quantification of the retained austenite volume fraction has been done using the NIS-elements software. Standard light microscope magnification was 800x. The measurements were made in various places of cross-sectional samples, in the direction from the surface towards the core material. Five measurements were done on each place. From obtained results, the mean value and the standard deviations were calculated.

Hardness measurements have been made throughout the laser influenced material using a Vickers hardness tester, at a load of 0.3 kg (HV 0.3). The hardness maps of cross-sections of laser traces were then constructed, enabling us to compare the microstructure to the hardness in any of the typical laser influenced regions.

## 3. Results and Discussion

Light micrograph, Figure 2, shows the microstructure of the substrate steel after quenching and tempering to a hardness of 700 HV. The material consists of the martensitic matrix

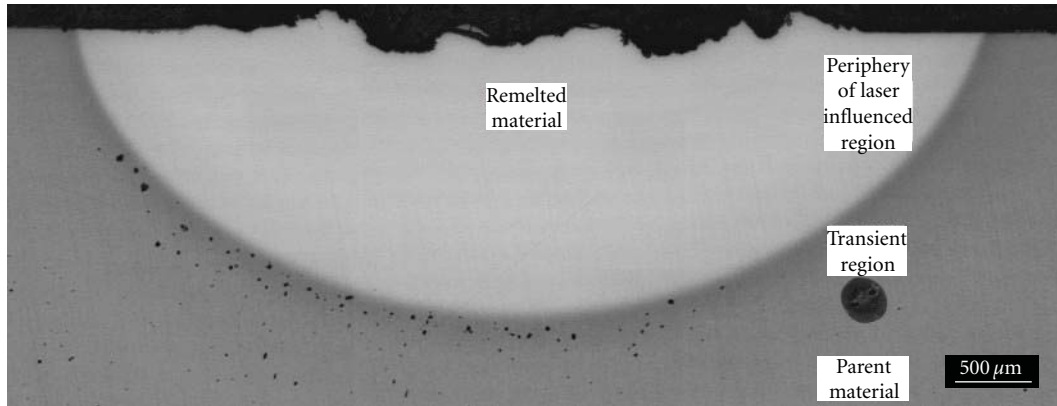


FIGURE 3: Cross-sectional light micrograph showing the overview of laser spot.

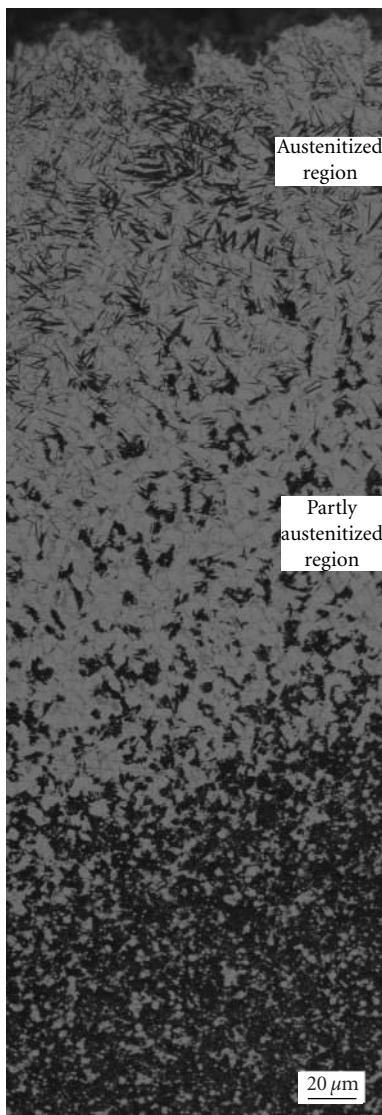


FIGURE 4: Cross-sectional light micrograph showing the periphery of laser influenced spot.

and fine (size of several microns) globular carbide particles. Previous experimental investigations revealed that the carbides are of two types—vanadium rich MC-phase and chromium-rich  $M_7C_3$ -phase [11].

The total influenced depth and width by laser were measured to be 1.7 and 5 mm, respectively, Figure 3. It is clearly shown that the surface quality of remelted material is poor because the processing led to increased surface roughness in the centre of the spot. Similar facts were reported by Ramous [12]. He stated that problems with the surface quality, connected with the needs of additional costs for surface finishing, are one of the limiting factors of industrial use of the laser surface melting technique. For further investigations, therefore, much more careful control of the laser parameters is necessary to obtain a good smooth surface. Other inhomogeneities (pores, cracks) were neither found in the laser spot nor in the vicinity of that.

Figure 4 shows the cross-sectional micrograph of the periphery of laser irradiated region. There are no symptoms of the remelting of the material. Close to the surface, there is a region that underwent rapid austenitizing up to a very high temperature and subsequent rapid cooling down, due to strong thermal flux into the core material. The microstructure consists of small portion of martensite, high portion of retained austenite and undissolved carbides. In between, there is the material, which also underwent the austenitizing during the laser irradiation. But, the processing time was not long enough for the complete transformation of the structure into the austenite. Therefore, the “islands” of nonaustenitized material can be found. The number and size of these formations increase as the distance from the surface increases. Parent material was not affected by laser beam and the structure consisted of tempered martensite and carbides, as developed by previous furnace treatment.

The central region of laser spot contained remelted zone close the surface, Figure 5. This zone can be divided into two characteristic regions. The first one, having a thickness of only several tens of microns, forms very tiny layer on the surface. The structure contained primary austenite cells and

TABLE 1: Results of retained austenite volume fraction measurements.

Depth below the surface (mm)	0.1	0.2	0.3	0.4	0.5	0.6	0.7
Central region	$82 \pm 2$	$81 \pm 4$	$67 \pm 7$	$63 \pm 4$	$39 \pm 5$	$16 \pm 3$	$17 \pm 3$
Periphery	$61 \pm 8$	$63 \pm 6$	$57 \pm 9$	$49 \pm 4$	$30 \pm 4$	$18 \pm 3$	$15 \pm 3$

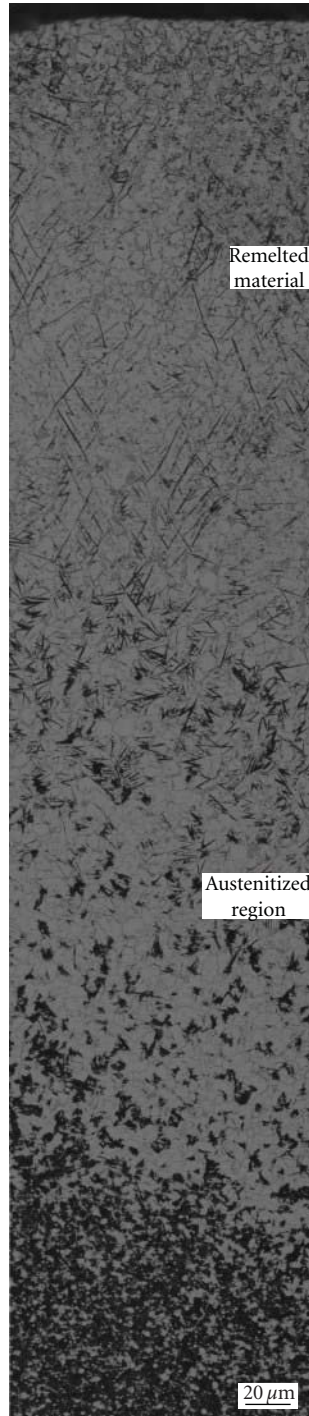


FIGURE 5: Cross-sectional light micrograph showing the central region of laser-influenced spot.

continuous eutectic network along them. The second typical region was larger. It underwent only partial melting. As a result, some of structural constituents were not influenced significantly by the laser processing. The microstructure of this region contained small amount of martensite and high portion of retained austenite. In the intergranular spacings, there is laser melted material, in a form of continuous network. Below the remelted zone, there is the austenitized and quenched region, having the microstructure similar to that described in one of above-mentioned paragraph.

Results of quantitative structural analysis are summarized in Table 1. The volume fraction of retained austenite exceeded clearly 60% in laser remelted and partially remelted material. But, also in the material austenitized to a very high temperature, see also upper part of Figure 4, the volume fraction of retained austenite over 50% has been identified. Towards the core material, however, the amount of retained austenite decreased to a “normal value”, ranging between 15–20%, which is typical for standardly furnace processed material Vanadis 6.

SEM micrograph, Figure 6, made from laser melted and rapidly solidified material shows that the microstructure is formed by the matrix and two morphological types of carbides. The matrix is mostly austenitic, but the presence of some portion of martensitic needles is also evident. EDS-map in Figure 7(a) shows that the first carbide type is a chromium rich phase. Based on our previous results [11, 13, 14] it can be assumed that chromium rich phase is the  $M_7C_3$ -carbide. These particles underwent evidently partial melting and during the freezing, they formed eutectics, Figures 6 and 7(a), respectively. The second type of carbides is the MC-phase, Figures 6 and 7(b), respectively. However, it contains also a small portion of chromium; see Figure 7(a). This finding is well consistent with other observations [15, 16], where up to 10 wt% Cr was found in MC-carbides. Globular shape of these particles, as formed by the manufacturing of the material indicates that they did not undergo melting during the laser processing of the material and remain almost completely unaffected.

For better clarification of the behaviour of laser irradiated material, previous experimental investigations upon the quaternary Fe-C-Cr-V alloys have to be taken into consideration. These experiments revealed that Cr-V ledeburitic steels solidify via complex mechanism where at least two eutectic transformations take place [13, 14]. The first transformation proceeds at higher temperature. As a result, needle-like mixture based on the MC-phase is formed. In the laser affected region, Figure 6, this mixture was not appeared. It seems that the temperature in dominant part of the laser spot was not high enough to enable complete melting of the

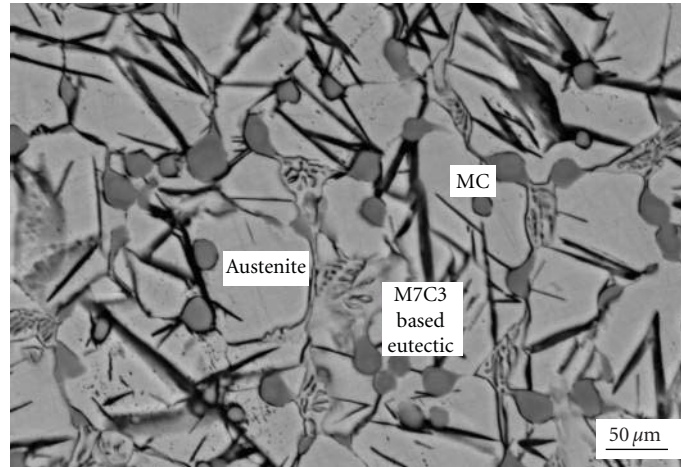
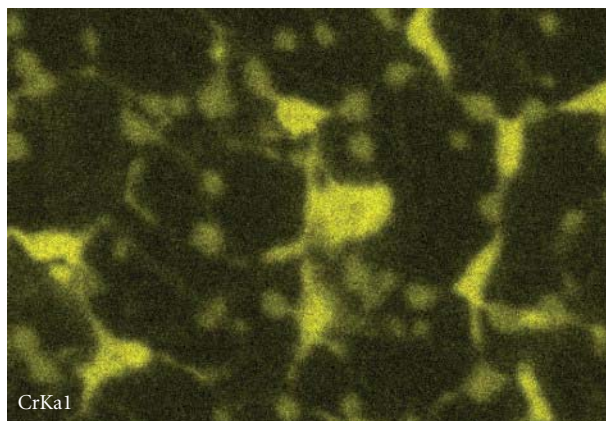
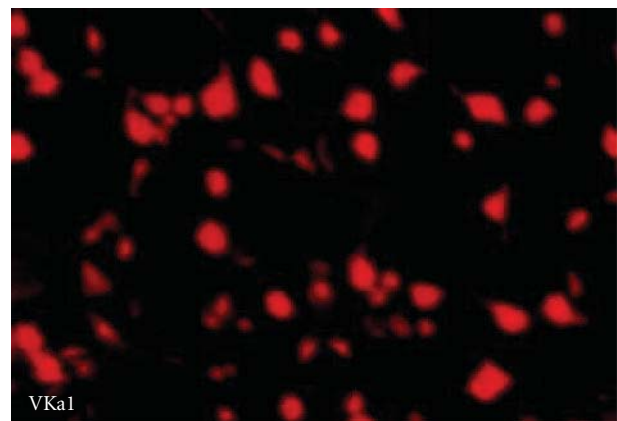


FIGURE 6: SEM micrograph showing the microstructure of remelted material.



(a)



(b)

FIGURE 7: EDS maps of chromium and vanadium distribution from the material shown in Figure 6.

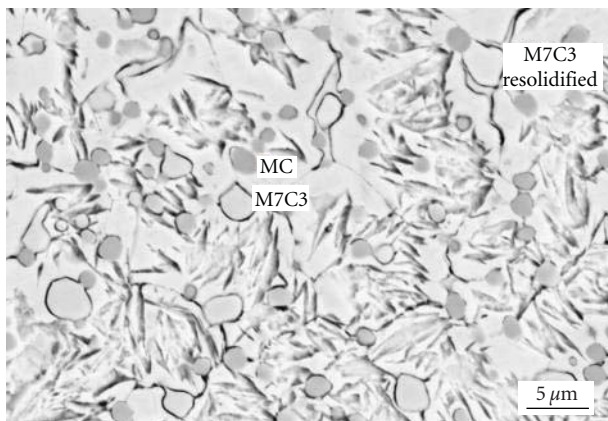


FIGURE 8: SEM micrograph showing the microstructure of interface region between remelted and solid state hardened zone.

material. The MC-carbides remain practically unaffected and retained globular shape, resulting from the manufacturing route of the steel.

During the solidification of Cr-V ledeburitic steels, the second eutectic mixture based on the  $M_7C_3$ -carbide is formed at lower temperature [13, 14]. It appears in a blade-like form in pure Fe-C-Cr system or if the vanadium content is sufficiently low in the alloy. At higher vanadium content, however, the morphology of this phase changes to skeleton. This is also the case of laser melted and resolidified Vanadis 6 steel, as clearly visible on the SEM micrograph, Figure 6.

Close to the melting boundary it is evident how the  $M_7C_3$ -carbides began to melt, Figures 8 and 9(a). If the temperature was close to the solidus of the material, then this phase transformed into a liquid in a very limited extent, and the second part remained almost unaffected. After the laser processing, the  $M_7C_3$ -phase solidified rapidly and formed semicontinuous formations along the grain boundaries. Since the temperature was not high enough for melting of other phases (solid solution, MC-phases), they remain almost unaffected. The formations along the primary grains can thus be considered as so-called “degenerate eutectic structure”, containing only one phase- $M_7C_3$ , Figures 8 and 9.

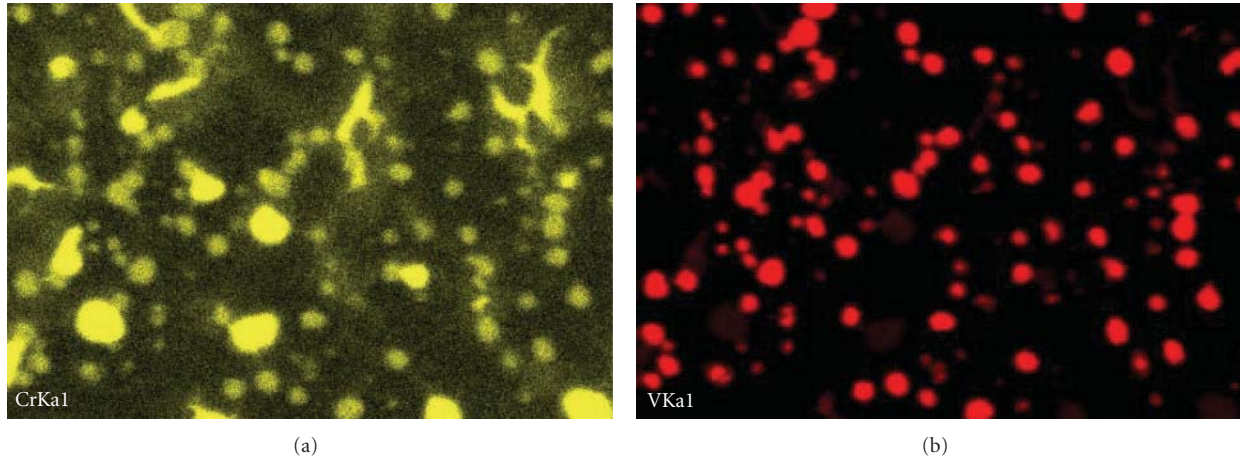


FIGURE 9: EDS maps of chromium and vanadium distribution from the material shown in Figure 8.

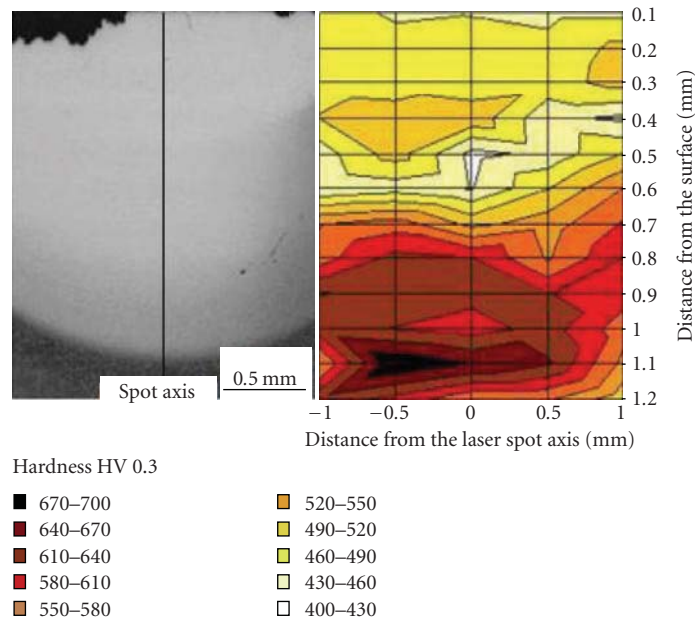


FIGURE 10: Hardness distribution throughout the laser influenced material.

The hardness of laser remelted and partially remelted material ranged between 490 and 580 HV 0.3, Figure 10. Region with such values of hardness reaches down to approximately 0.5 mm from the surface. Around, there is a slightly softer material, having hardness between 400 and 460 HV 0.3. The periphery of laser-influenced region, which was completely austenitized but not overheated, had the highest hardness. It exceeded 600 HV 0.3, but in some cases it was higher than 700 HV 0.3. The hardness of the transient region, located in close vicinity of the laser spot, exhibited considerably lower hardness compared to fully austenitized material of the periphery of the laser spot. The hardness values ranged around 450 HV 0.3.

The behaviour of the laser-influenced material with respect to the hardness can be explained as follows: the remelted material contains primary grains of the austenite,

small portion of the martensite, MC-carbides (that mostly did not undergo melting), and  $M_7C_3$ -carbides (less or more transferred into a liquid phase during processing). It is naturally to expect that this structure has reduced hardness compared to no laser influenced material because two processes were probably happening during the laser processing. The first one is the extension of solid solutions, due to the rapid solidification effect (hardness increase). The second phenomenon is connected with extremely high saturation of as-solidified austenite with carbon and alloying elements and results in high portion of retained austenite in resolidified material of laser spot; see also Table 1. The final hardness of remelted material is then a result of the competition between these two processes whereas it is evident that the softening, caused by extremely high retained austenite volume fraction, becomes dominant. It should also

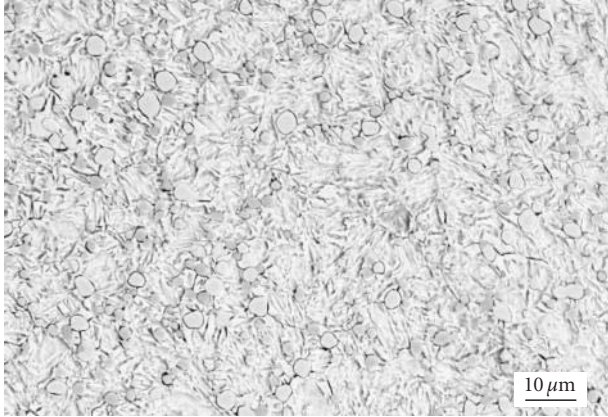


FIGURE 11: SEM micrograph showing the microstructure of solid state hardened zone.

be noticed that the cooling rates in laser processing cannot exceed  $10^5 \text{ K s}^{-1}$  for common metallic materials. Therefore, the microstructural effects are reduced only to the grain refinement and slight extension of solid solutions, which is insufficient to compensate the softening effect of highly retained austenite content.

One possible way how to increase the hardness of laser remelted material is a subsequent tempering. The tempering of Cr-V ledeburitic steels at the temperature around  $500^\circ\text{C}$  generally induces a hardness increase, commonly known as secondary hardening effect. It is connected with the precipitation of fine carbides from the martensite and the retained austenite, respectively, and with the transformation of retained austenite to the martensite during the cooling down from the tempering temperature. As pointed out elsewhere [8], the maximum secondary hardness peak of laser melted and rapidly solidified metals is shifted to higher tempering temperature. As the principal explanation, higher energy needed for the destabilization of retained austenite compared to furnace processed materials, was suggested. In addition, it should be mentioned that there is no presence of phases (for instance  $\delta$ -ferrite) in laser remelted Vanadis 6 steel, which could influence the secondary hardenability of the material in a negative way. The challenge for future experiments is then to perform the investigations of tempering behaviour of the laser remelted Vanadis 6 steel.

Additional softening of the material below the remelted area is also natural to be expected. This region contains also the retained austenite as the dominant constituent. But its supersaturation can be expected to be even much lower than that of remelted region.

The maximum hardness was found in the solid state hardened area. There is the structure with the fine needle-like martensite, small portion of retained austenite, and undissolved carbides, Figure 11. Such a structural type corresponds well to that developed but conventional furnace austenitizing and quenching, of course in a refined manner. High hardness of solid state hardened material is then logical.

In the vicinity of the laser spot, the hardness decreased again, as a result of so-called overtempering of the material. It can be believed that in narrow region around the laser

spot, the temperature exceeded the tempering temperature of the material ( $550^\circ\text{C}$ ) but did not reach to the austenitizing temperature. It is known that Cr-V ledeburitic steels have the maximum secondary hardness peak at the tempering temperatures from the range  $500\text{--}550^\circ\text{C}$ . Beyond this peak, the hardness drops down rapidly [17]. Measured values in this region, being around 450 HV 0.3, correspond very well to these considerations.

#### 4. Conclusions

Laser surface hardening with remelting has been carried out on the Vanadis 6 ledeburitic steel. The main findings can be summarized as follows.

Laser affected spot consists of four typical regions. In the centre, there are thin completely remelted and much larger partially remelted regions. Around, solid state hardened region and thin overtempered zones are located.

The microstructure of remelted region is formed with primary austenite cells and continuous eutectic network along them. Partially melted region contains undissolved MC-carbides, austenitic grains with certain portion of the martensite, and less or more continuous “degenerate eutectic” network based on the  $\text{M}_7\text{C}_3$ -carbides.

Solidification mechanism of laser completely melted material corresponds well to previous observations of the author, concerning the Fe-C-Cr-V quaternary alloys. If the material was not completely melted, then the solidification was restricted only to the formation of either standard  $\text{M}_7\text{C}_3$ -carbide/austenite eutectic or, if the temperature was even lower, to the so-called “degenerate” eutectic based on the same carbide.

Laser remelted material is significantly softer than that hardened in a solid state. Principal explanation can be given by the presence of dominant portion of retained austenite in the microstructure.

Low hardness in laser remelted region could be improved by subsequent tempering. Since the primary grains do not contain any phases that could restrict the capability of the material to be strengthened via precipitation, the investigation of the tempering behaviour of the laser melted Vanadis 6 steel is a challenge for the future investigations.

#### References

- [1] P. R. Strutt, H. Nowotny, M. Tuli, and B. H. Kear, “Laser surface melting of high speed tool steels,” *Materials Science and Engineering*, vol. 36, no. 2, pp. 217–222, 1978.
- [2] P. Molian and H. Rajasekhara, “Laser melt injection of BN powders on tool steels I: microhardness and structure,” *Wear*, vol. 114, no. 1, pp. 19–27, 1987.
- [3] P. Jurčí, P. Stolař, and I. Dlouhý, “Laser heat treatment of 6-5-2 high speed steels of different production way,” in *Proceedings of the 10th Congress of the IFHTE*, T. Bell and R. J. Mittemeijer, Eds., vol. 25, Brighton, UK, 1996.
- [4] H. Jones, “Modelling of growth and microstructure selection in rapid solidification: a progress report,” *Materials Science and Engineering A*, vol. 133, pp. 33–39, 1991.
- [5] P. F. Nizhnikovskaya, E. P. Kalinushkin, L. M. Snagovskij, and G. F. Demchenko, “Structural formation of high-speed

- steels during crystallization, *Metallovedenie i Termicheskaya Obrabotka Metallov*,” *Metal Science and Heat Treatment*, vol. 24, no. 11, pp. 777–784, 1982.
- [6] P. Jurčí, O. Honzík, and P. Stolař, “Investigation of laser affected zones on the 19830-grade high speed steel,” *Metal Materials*, vol. 33, p. 165, 1995.
- [7] P. Jurčí, “Surface remelting of ledeburitic steels by laser,” *Metal Letters*, vol. 53, p. 12, 1998.
- [8] R. Colaço and R. Vilar, “Effect of laser surface melting on the tempering behaviour of DIN X42Cr13 stainless tool steel,” *Scripta Materialia*, vol. 38, no. 1, pp. 107–113, 1997.
- [9] R. Colaço and R. Vilar, “Stabilisation of retained austenite in laser surface melted tool steels,” *Materials Science and Engineering A*, vol. 385, no. 1-2, pp. 123–127, 2004.
- [10] P. Jurčí and P. Grgáč, “Structural analysis of laser surface remelted CH3F12-alloy,” in *Proceedings of the International Conference of Technology*, P. Kostka, Ed., Bratislava, Slovakia, September 1993.
- [11] P. Jurčí, F. Hnilica, J. Suchánek, and P. Stolař, “Microstructural features of Cr-V ledeburitic steel saturated with nitrogen,” *Materials and Technology*, vol. 38, p. 13, 2004.
- [12] E. Ramous, “Rapid surface melting,” *Materials Science and Engineering A*, vol. 178, no. 1-2, pp. 185–188, 1994.
- [13] P. Jurčí, *Preparation and investigation of properties of rapidly solidified powders and compacts of the Fe-C-Cr-V - system*, Ph.D. thesis, MtF STU, Trnava, Slovakia, 1996.
- [14] P. Jurčí, D. Vojtěch, and P. Stolař, “Influence of solidification conditions on microstructure and phase composition of a Fe-4C-12Cr-13V alloy,” *Zeitschrift fuer Metallkunde*, vol. 88, no. 9, pp. 733–738, 1997.
- [15] R. A. Versaci, “Stability of carbides in M2 high speed steel,” *Journal of Materials Science Letters*, vol. 7, no. 3, pp. 273–275, 1988.
- [16] K. Stiller, L. E. Svensson, P. R. Howell, W. Rong, H. O. Andrén, and G. L. Dunlop, “High resolution microanalytical study of precipitation in a powder metallurgical high speed steel,” *Acta Metallurgica*, vol. 32, no. 9, pp. 1457–1467, 1984.
- [17] P. Jurčí, J. Sobotová, J. Cejp, P. Salabová, and O. Prikner, “Effect of sub-zero treatment on mechanical properties of the vanadis 6 PM ledeburitic tool steel,” in *Proceedings of the 19th International Metallurgical and Materials Conference (METAL '10)*, S. R. O. Tanger, Ed., Rožnov pod Radhoštěm, Czech Republic, May 2010.

## Research Article

# Influence of Welding Parameters on Weld Formation and Microstructure of Dual-Laser Beams Welded T-Joint of Aluminum Alloy

Min Li,<sup>1</sup> Zhuguo Li,<sup>1</sup> Yong Zhao,<sup>1</sup> Hao Li,<sup>2</sup> Yuhua Wang,<sup>2</sup> and Jian Huang<sup>1</sup>

<sup>1</sup> Shanghai Key Laboratory of Materials Laser Processing and Modification, Shanghai Jiao Tong University, Shanghai 200240, China

<sup>2</sup> Shanghai Aircraft Manufacturing Co., Ltd. Shanghai 200436, China

Correspondence should be addressed to Jian Huang, [jhuang@sjtu.edu.cn](mailto:jhuang@sjtu.edu.cn)

Received 15 March 2011; Revised 24 May 2011; Accepted 26 May 2011

Academic Editor: J. Dutta Majumdar

Copyright © 2011 Min Li et al. This is an open access article distributed under the Creative Commons Attribution License, which permits unrestricted use, distribution, and reproduction in any medium, provided the original work is properly cited.

This paper focused on the welding 1.8 mm thick 6061 aluminum alloy plates in T-joint form using dual lasers that introduced by a Nd: YAG laser and a CO<sub>2</sub> laser with 4043 aluminum filler wire. The effects of welding parameters on the T-joint weld appearance, microstructure and the joint mechanical properties were studied systematically. The influence of welding parameters included the distance between two laser beams, welding speed, laser power and the laser beam offset toward the stringer. The weld appearance, microstructure, hardness of the joint were evaluated by optical microscope and micro-hardness test. A monotonic quasi-static tensile test was conducted by a self-made clamping device to obtain the tensile property of welded joints. At the optimized parameters, the welded T-joint showed good weld appearance without macro defects; the micro hardness of welds ranged from 75 to 85 HV<sub>0.3</sub>, and the tensile strength was about 254 MPa with the fracture at the heat affected zone on the stringer side.

## 1. Introduction

From the viewpoint of demand for weight loss in aerospace industry, joint, of fuselage panels connected by traditional mechanical fastening will be replaced by laser beam welding [1]. Laser beam welding provides outstanding characteristics of high energy density, high welding speed, high flexibility of the moving system, low distortions, narrow heat affected zone, and high depth-to-width ratio [2–4]. However, T-joint of fuselage panels welded at one side by full penetration will cause distortions because of the asymmetric force. Distortions not only increase the difficulty of frock clamping, but also add the probability of crack [5–7]. In past decades, mitigation methods have been developed to reduce welding distortion using different approaches, such as low-stress no-distortion welding with additional cooling [8], predeformation [9], thermal tensioning [10], optimized welding sequences [11], or change clamping support distance [12]. Those methods are capable of reducing the distortion of T-joint, however, dual-beam laser welding synchronously at two sides can minimize the formation of weld-induced

self-stresses in the weld seams because of the symmetrical stress distribution. In essential, dual beam laser weld T-joint is a more efficient way to weld T-joint configuration. Up to now, the influence of welding parameters on weld formation and microstructure of T-joint welded by dual laser beams was seldom reported, especially for thin aluminum alloy plates. So this paper focuses on the welding of 1.8 mm thin aluminum alloy plate T-joints synchronously at two sides. The main goal is to evaluate the effects of welding parameters on the microstructures and joint mechanical properties systematically. Welding parameters include the distance between two laser beams, welding speed, laser power, and the laser beam offset toward the stringer (BOF).

## 2. Materials and Method

Test plates used in this study were the age-hardened (T6) 6061 aluminum alloy with the thickness of 1.8 mm. The weld seam between the stringers and the fuselage skin were simultaneously welded from both sides of the stringer by means of a dual-beam system. The dual-beam system is composed

TABLE 1: Nominal chemical composition of materials used (wt.%).

	Si	Fe	Cu	Mn	Mg	Cr	Zn	Ti	Al
6061	0.4–0.8	0.7	0.15–0.4	0.15	0.8–1.2	0.10	0.25	0.15	Balance
4043	4.5–6.0	<0.8	0.30	0.05	0.05	—	0.10	<0.02	Balance

of a 15 kW continuous wave (cw) CO<sub>2</sub> laser TLF15000 of TRUMPF and a 3 kW cw Nd:YAG laser LS-YC of IHI with spot sizes of 0.86 mm and 0.9 mm, respectively. YAG laser beam is in multimode, CO<sub>2</sub> laser beam is of low-order mode. The dual beam lasers were fixed together with the self-designed fixture system to ensure synchronism. During the laser processing, pure helium gas was used as the shielding gas, which was coaxial ejected with the laser beams. The flow rates are 15 and 28 L/min at the sides of Nd:YAG laser and CO<sub>2</sub> laser, respectively. According to results of the pre-experiment and the simulate calculation, the applied filler wires are Tehan-4043 aluminum alloy with diameters of 1.0 mm and 1.2 mm. The chemical compositions of the substrate material and the filler wire are listed in Table 1 and the experiment setup for the T-joint welding is described in Figure 1. The Nd:YAG laser beam formed an angle of  $\beta$  (45°) with the skin and  $\theta$  (25°) for the CO<sub>2</sub> laser, filler wire were held at the angle of 11° to the stringer at the side of Nd:YAG but perpendicular to the stringer at the CO<sub>2</sub> side. The symbols  $h$  and  $d$  represent the position of laser focused on the stringer and the distance between two laser beams, respectively. Before welding, plate surface was cleaned by abrasive paper and then washed by a sodium hydroxide solution followed by nitric acid to remove and minimize the oxide film.

Macrographs and microstructure observation were performed using optical micrographs. Micro-Vickers hardness was tested on the cross-section of the welded T-joints using a load of 300 g for 15 s. The T-joint tensile tests were carried out on Zwick Z020 E-stretching machine at a strain rate of 0.5 mm/min by a home-made device for clamping specimens. According to the routine operating general recognized in aeronautic industry, the specimen geometry for T-joint tensile test and the schematic description of the self-made clamping device were shown in Figures 2 and 3, respectively.

### 3. Experimental Results and Discussions

**3.1. Appearance of the Weld.** In our pre-experiments, deep penetration cannot be produced by 3 kW Nd:YAG due to the low power density. However, by preheating of tested plate, the weld depth can be increased significantly. For example, the sample preheating at 300°C showed an depth of the weld bead twice as deep as the sample without preheating, 1.00 mm versus 0.53 mm at the same welding condition (laser power = 2.8 Kw, welding speed = 1 m/min). Taking this fact into account, the Nd:YAG laser beam was placed behind CO<sub>2</sub> laser beam to facilitate preheating and its output was kept at 2.8 kW. The feed rate of the filler wire and the BOF were maintained at 1.4 m/min and 0.5 mm because of its minimal affection. To simplify the discussion, the wire

TABLE 2: Influence of the distance between two laser beams on welding process (welding parameters: P<sub>CO<sub>2</sub></sub> = 7.8 KW,  $v$  = 4 m/min).

The distance between two laser beams	Welding process
0~1.0 mm	Unstable
1.0~1.5 mm	Stable
1.5~3.0 mm	Unstable

feeding speed at the side of CO<sub>2</sub> laser was also kept at a constant value of 4.2 m/min.

It is well know that the distance between two laser beams plays an important role on the welding result. Therefore, different distances have been tested from 0 to 3 mm in order to investigate the effect of this parameter on the stability of the welding. As Table 2 shows, when the distance between two laser beams is relatively small (0~1.0 mm), the absorption of Nd:YAG laser power increased and the welding seam got deeper and wider. However, smaller distance caused higher instability of welding process; this problem existed due to less preheating of the plate at the position of Nd:YAG laser focus and therefore incomplete melting of filler wire, which then resulted in blocking of wire feed and breaking off the welding process. If the distance is too big (1.5~3.0 mm), the plate also could not be preheated enough to acquire deep penetration. The distance between two laser beams which ranged from 1.0 to 1.5 mm was suitable to get stable welding processing and proper weld formation. Based on that, in the following experiment the distance between two laser beams was set as 1.5 mm.

T-joints were successfully welded with welding speed of 2 to 6 m/min and the CO<sub>2</sub> laser power of 7.8 kW. The typical macrographs of weld cross-sections were shown in Figure 4. It can be seen that weld seam at the side of CO<sub>2</sub> laser (left side in each photo) was wider than that of Nd:YAG because of the relatively higher energy input of CO<sub>2</sub> laser. Meanwhile, with the increased welding speed, the welding seam changed from full, wide penetration to partial, small penetration. The undercut is seen in Figures 4(a) and 4(d), but the reason is different. In the lower welding speed, the undercut is formed because of the evaporation of melted metal. While welding in the higher speed, undercut also formed for the fast cooling speed and inadequate filler wire. According to the pre-experiment, porosity is not the main problem in the whole welding processing. In general, the porosity is reduced with the increasing welding speed, because the flow of the melted metal improved and the gas can escape more easily. However, when the welding speed is too high, gas can not escape from the pool in the limited time and the amount of porosity increased. Weld beam with full penetration is useful

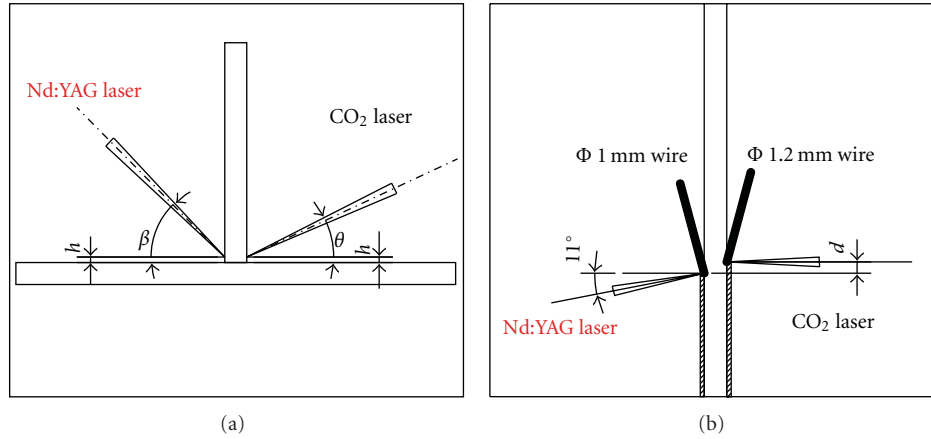


FIGURE 1: Schematic diagram of the experiment set-up used for the T-joint experiment.

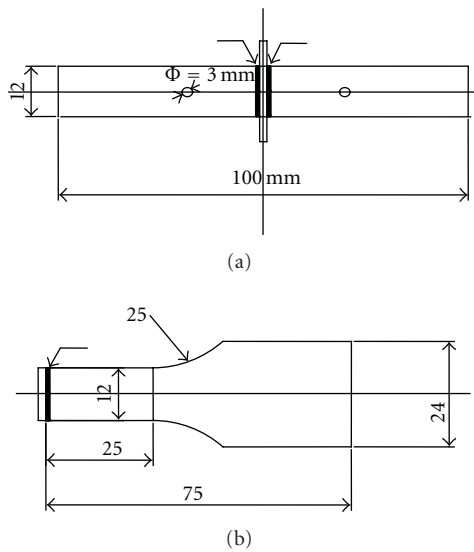


FIGURE 2: Specimen geometry for T-pull test.

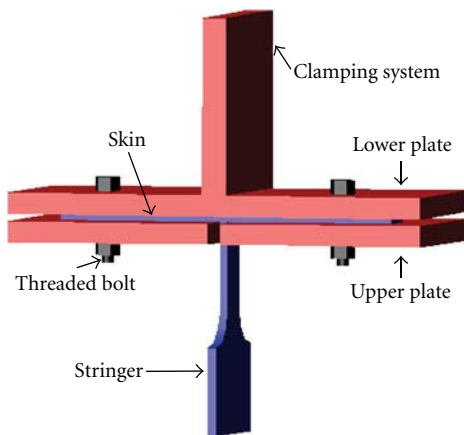


FIGURE 3: Self-made lamping system adopted to perform T-pull test.

to reduce the porosity. Welding speed range of 3 m/min to 4 m/min was suitable to form a sound weld seam.

The weld cross sections at different CO<sub>2</sub> laser power at the same welding speed of 4 m/min are shown in Figure 5. It can be found that with the increased laser power, the weld seam at CO<sub>2</sub> laser side became larger, but little change at the side of Nd:YAG laser was observed. When the CO<sub>2</sub> laser power is relatively low, the weld seam at both sides was similar, but incomplete penetration was formed as shown in Figures 5(a) and 5(b) with the red arrow pointed out. The unpenetrated fusion hindered the escape of gas with a result of higher porosity. With the increase of laser power, weld seam area at CO<sub>2</sub> laser side became much larger than Nd:YAG. When the laser power increased to 8.0 kW, undercut took place at CO<sub>2</sub> laser side, as show in Figure 5(e). As shown in Figures 5(c) and 5(d), with the laser power of 7.5 kW and 7.8 kW, sound weld seams without macrodefects were formed.

When laser spot focuses on joint of the stringer and the skin (BOF = 0 mm), any tiny change may cause large fluctuation of the weld pool, which will lead to an unstable welding process. However, the offset of laser beam toward the stringer can stabilize the welding process. Table 3 presented the widths of upper and inner fillet weld leg fabricated using BOF of 0, 0.5, and 1.0 mm at the CO<sub>2</sub> laser side, respectively. It can be seen that the widths of upper and inner weld leg were not symmetry and the ratio of upper and inner weld leg width was 1.35 when the BOF was 1.0 mm. Besides, there was undercut in the stringer (see in Figure 5(e)). When BOF was 0.5 mm, upper and inner weld legs of weld beam were symmetrical without any obvious defect.

**3.2. Microstructures.** The optical micrograph, as shown in Figure 6(a), reveals the whole view of the T-joint. While high-magnification images of spot A, B, C, and D in Figure 6(a) were shown as Figures 6(b), 6(c), 6(d), and 6(e), respectively. At the center of welding seams, very fine cellular-dendrite structures are found. The grain size at the side of Nd:YAG welding seam is a little smaller than that at CO<sub>2</sub>

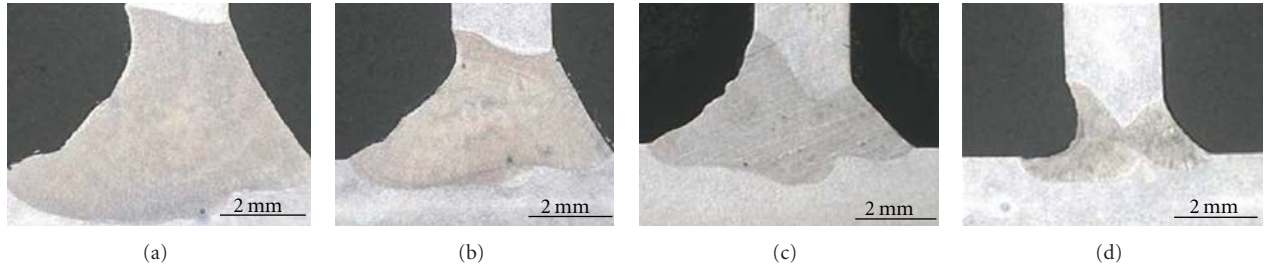


FIGURE 4: Macrographs of the weld seams obtained at different welding speed (fixed welding parameter:  $P_{CO_2} = 7.8\text{ kW}$ ). (a) 2 m/min, (b) 3 m/min (c) 4 m/min, (d) and 6 m/min.

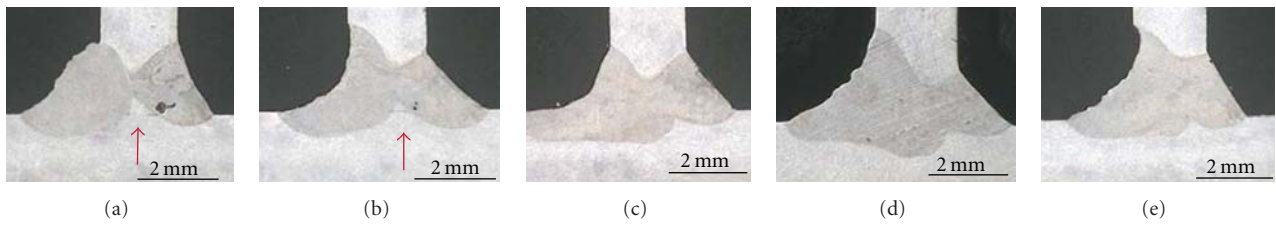


FIGURE 5: Macrographs of the weld seams obtained using different laser power of  $CO_2$  laser (fixed welding parameter:  $v = 4\text{ m/min}$ ). (a) 6.8 KW, (b) 7.2 KW, (c) 7.5 KW, (d) 7.8 KW, and (e) 8.0 KW.

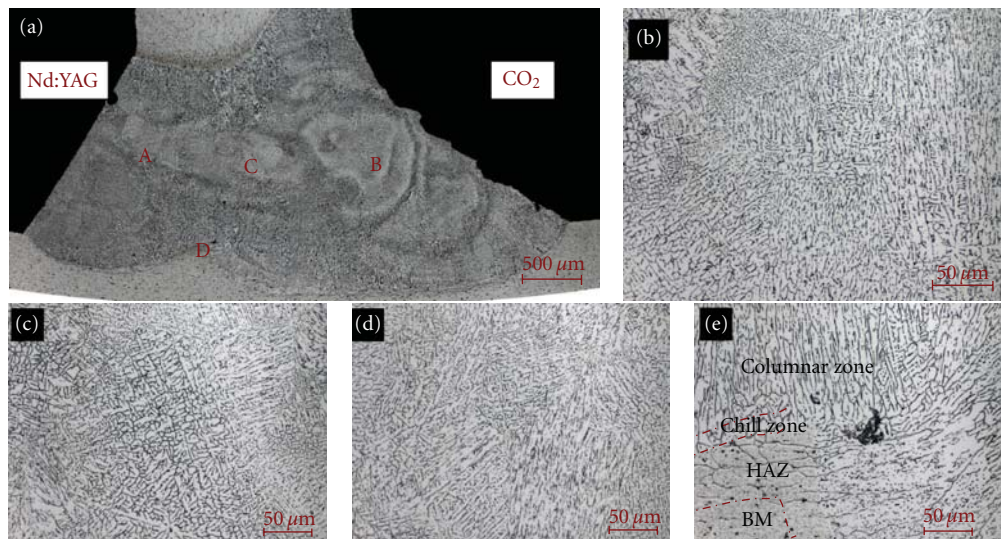


FIGURE 6: OM micrographs of T-joint (welding parameter:  $P_{CO_2} = 7.8\text{ KW}$ ,  $v = 4\text{ m/min}$ ). (a) Macrographs of the weld seam; (b) high magnification of spot A; (c) high magnification of spot B, (d) high magnification of spot C, and (e) High magnification of spot D.

TABLE 3: Influence of BOF on the width of upper/down fillet weld leg and welding process (welding parameters:  $P_{CO_2} = 7.8\text{ KW}$ ,  $v = 4\text{ m/min}$ ).

BOF (mm)	Upper fillet weld leg width (mm)	Down fillet weld leg width (mm)	Ration of upper/down weld leg width	Welding process
0	1.55	2.29	0.67	Unstable
0.5	2.28	2.25	1.01	Stable
1.0	2.03	1.50	1.35	Stable

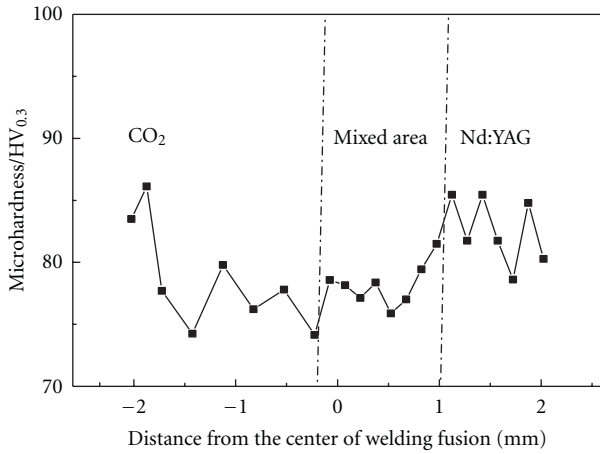


FIGURE 7: Microhardness of the welding seam (welding parameter:  $P_{CO_2} = 7.8 \text{ KW}$ ,  $v = 4 \text{ m/min}$ ).

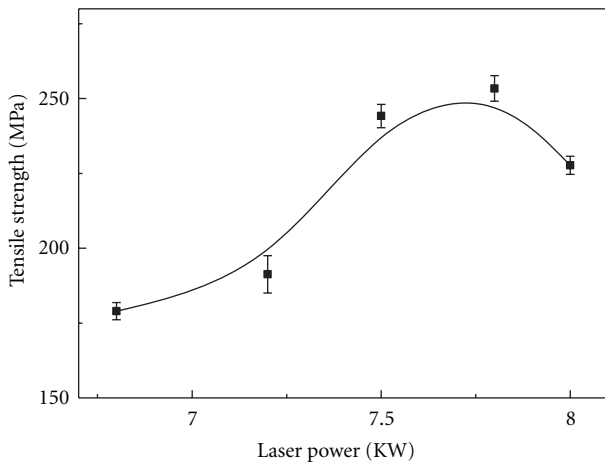


FIGURE 8: Relationship between tensile strength and laser power at the welding speed of 4 m/min.

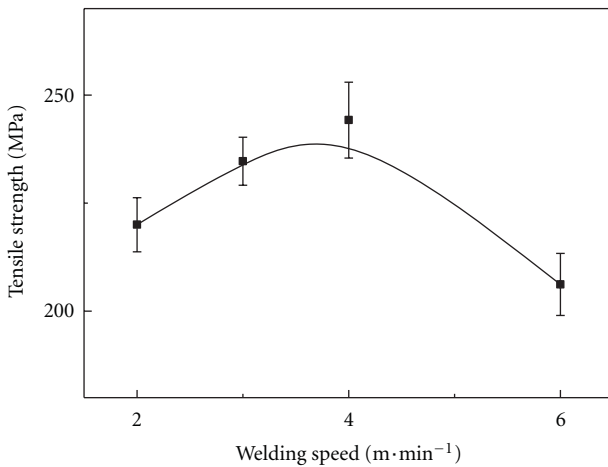


FIGURE 9: Relationship between tensile strength and welding speed at the laser power of 7.8 kW.

laser side due to less laser energy input. The root area of the mixed welding seam as shown in Figure 6(e) contains several distinct microstructure zones from the fusion zone to the base material. They are (1) columnar zone, parallel dendrites preferentially grew along the heat flow direction; (2) chill zone, small equiaxed grain formed; (3) heat affected zone (HAZ), the grain grow coarse to the equiaxed grain; (4) base material region (BM). The detail is drawn by the dotted line.

Varieties of microstructures were due to the different cooling rate and heat transfer direction. The morphology of the solidification structures developed in the fusion zone was controlled by the parameter  $G/R$  ( $G$  is the thermal gradient in the liquid and  $R$  is the solidification growth ratio) and the undercooling level. At the center of fusion zone,  $G/R$  reached a minimum value. While close to the fusion line, it gained its maximum in the columnar zone, with the microstructure changed from the cellular-dendrite at the center of fusion zone to parallel dendrites. Near the fusion line, the melted metal has high undercooling level, forming fine equiaxed grain (show in Chill zone). The grain in the HAZ have been affected by the thermal circle and grown coarse.

**3.3. Microhardness.** Figure 7 shows the microhardness profile across the weld bead of the T-joint with the  $CO_2$  laser power of 7.5 kW. At the side of Nd:YAG fusion zone, hardness is slight higher than other area, because of low heat input resulting in smaller grain size. At the side of the  $CO_2$  fusion zone, the micro-hardness is the lowest, for heat input is higher and the grain grows coarse. However, near the surface of the weld bead at the side of  $CO_2$  laser, the micro-hardness increased sharply because of the fast cooling speed and small grain obtained. In the mixed area, the value of micro-hardness is between those of Nd:YAG laser and  $CO_2$  laser. The result of micro-hardness coincides well with the grain size as Section 3.2 described.

**3.4. Tensile Strength.** Figures 8 and 9 show the tensile strength plot against laser power and welding speed, respectively. When the laser power was relatively low, the T-joint exhibited lower tensile strength because of nonfusion. The peak tensile strength located at about 7.5 kW to 7.8 kW, which corresponded to the complete penetration without any obvious defect. If the laser power is kept increased, the tensile strength decreased because of the grown grain size and undercut. The plot of tensile strength against welding speed is similar to Figure 8 for the same reason as discussed above. With the welding speed increased, tensile strength got maximum value at 4 m/min and then decreased, and the peak tensile strength was 254 MPa with the fracture at the heat affected zone (HAZ) on the stringer side.

## 4. Conclusions

- (1) The parameters such as distance between two laser beams ( $d$ ), welding speed ( $v$ ), laser power ( $P$ ), and the laser beam offset toward the stringer (BOF) was systematically investigated. The results showed that

- these parameters have great effect on the stability and macrostructure of the welding.
- (2) The undercut would be occurred under relatively high and low welding speed as well as higher laser power. Complete penetration is helpful to reduce the porosity.
  - (3) With the optimized parameters ( $d = 1.0\sim 1.5$  mm,  $v = 3\sim 4$  m/min,  $P_{CO_2} = 7.5 \sim 7.8$  kW, BOF = 0.5), T-joint with good weld appearance, no obvious porosity, and undercut was observed.
  - (4) Micrograph observation showed the joint had different distinct zone with different microstructure from the center of fusion zone to the BM. At the center of fusion zone, cellular dendrites are present. While close to the fusion line, microstructure changes to parallel dendrites for preferentially elongating along the heat flow direction. In chill zone, fine equiaxed grain formed due to high undercooling level. In the HAZ, grain grew coarse for the thermal circle.
  - (5) Micro-hardness at the Nd:YAG zone is higher than other area due to smaller grain size. The tensile strength was about 254 MPa with the fracture at the heat affected zone (HAZ) on the stringer side.
- [9] K. Masubuchi, *Analysis of Welded Structures*, Pergamon Press, New York, NY, USA, 1980.
  - [10] M. V. Deo and P. Michaleris, "Mitigation of welding induced buckling distortion using transient thermal tensioning," *Science and Technology of Welding and Joining*, vol. 8, no. 1, pp. 49–54, 2003.
  - [11] W. Machold, W. Staron, P. Bayraktar, F. Riekehr, S. Kocak, and M. Schreyer, "Influence of the welding sequence on residual stresses in laser welded t-joints of an airframe aluminum alloy," *Stress Evaluation in Materials using Neutrons and Synchrotron Radiation*, vol. 571-72, pp. 375–380, 2008.
  - [12] T. Schenk, M. Doig, G. Esser, and I. M. Richardson, "Influence of clamping support distance on distortion of welded T joints," *Science and Technology of Welding and Joining*, vol. 15, no. 7, pp. 575–582, 2010.

## References

- [1] M. Zain-ul-abdein, D. Nélias, J. F. Jullien, and D. Deloison, "Experimental investigation and finite element simulation of laser beam welding induced residual stresses and distortions in thin sheets of AA 6056-T4," *Materials Science and Engineering A*, vol. 527, no. 12, pp. 3025–3039, 2010.
- [2] C. Williams, "CO<sub>2</sub> laser processing—an overview," *Aircraft Engineering and Aerospace Technology*, vol. 69, no. 1, pp. 43–52, 1997.
- [3] X. Cao, W. Wallace, C. Poon, and J. P. Immarrigeon, "Research and progress in laser welding of wrought aluminum alloys. I. Laser welding processes," *Materials and Manufacturing Processes*, vol. 18, no. 1, pp. 1–22, 2003.
- [4] E. Schubert, M. Klassen, I. Zerner, C. Walz, and G. Sepold, "Light-weight structures produced by laser beam joining for future applications in automobile and aerospace industry," *Journal of Materials Processing Technology*, vol. 115, no. 1, pp. 2–8, 2001.
- [5] M. Zain-ul-Abdein, D. Nelias, J. F. Jullien, and D. Deloison, "Prediction of laser beam welding-induced distortions and residual stresses by numerical simulation for aeronautic application," *Journal of Materials Processing Technology*, vol. 209, no. 6, pp. 2907–2917, 2009.
- [6] S. Daneshpour, M. Koçak, F. S. Bayraktar, and S. Riekehr, "Damage tolerance analyses of laser welded "skin-clip" joints for aerospace applications," *Welding in the World*, vol. 53, no. 3-4, pp. R90–R98, 2009.
- [7] F. S. Bayraktar, P. Staron, M. Koçak, and A. Schreyer, "Analysis of residual stress in laser welded aerospace aluminium T-joints by neutron diffraction and finite element modelling," *Materials Science Forum*, vol. 571-572, pp. 355–360, 2008.
- [8] E. M. Van der Aa, *Local cooling during welding: prediction and control of residual stresses and buckling distortion*, Ph.D. thesis, Delft University of Technology, Delft, The Netherlands, 2006.

## Research Article

# Direct Laser Cladding of Cobalt on Ti-6Al-4V with a Compositionally Graded Interface

**Jyotsna Dutta Majumdar**

*Department of Metallurgical and Materials Engineering, Indian Institute of Technology, Kharagpur 721302, India*

Correspondence should be addressed to Jyotsna Dutta Majumdar, jyotsna@metal.iitkgp.ernet.in

Received 1 March 2011; Accepted 21 May 2011

Academic Editor: Smurov Igor

Copyright © 2011 Jyotsna Dutta Majumdar. This is an open access article distributed under the Creative Commons Attribution License, which permits unrestricted use, distribution, and reproduction in any medium, provided the original work is properly cited.

Direct laser cladding of cobalt on Ti-6Al-4V with and without a graded interface has been attempted using a continuous wave CO<sub>2</sub> laser. Graded interface is developed by depositing a thin copper layer on Ti-6Al-4V substrate prior to multiple laser cladding of cobalt on it. Presence of copper interlayer was found to suppress the formation of brittle intermetallics of Ti and Co. The effect of process parameters on the microstructures, compositions, and phases of the interface was studied in details. Finally, the mechanical and electrochemical properties of the interface processed under optimum process parameters are reported.

## 1. Introduction

The conventionally replaced hip consists of three parts; a ball which rotates in a hollow socket, and it is fixed into the femur (thigh bone) by a stem [1]. Co-Cr-Mo is the most appropriate alloy for the ball because of its very high elastic modulus and its wear and corrosion resistance [1]. On the other hand, Ti-6Al-4V alloy is the most acceptable stem material. The ball and stem may be held together with a taper. Though the use of multimaterials seems economical to prepare component for hip replacement, loosening of metals from the interface because of fretting and corrosion attack is a severe problem. It has been observed that maximum performance and service life of the bio implants may be achieved when the component is made of a single material. Direct laser cladding is a technique where fabrication of solid components is achieved by laser-assisted melting of the materials in the form of particles/wire, deposition of molten layer on a substrate in a layer by layer fashion and thereby, building of the full component using computer-aided design (CAD) [2]. Notable advantages of the technique over conventional fabrication techniques include faster processing speed, no requirement of tooling, ability to fabricate complex shapes, and retention of metastable microstructure/composition [3]. Arcella and Froes [4] reported on the laser forming of tita-

nium. Srivastava et al. [5] reported on the direct laser fabrication of Ti<sub>48</sub>Al<sub>2</sub>Mn<sub>2</sub>Nb alloy and established the role of process parameters on the microstructure. Effect of process parameters on the quality of the DLD layers have been studied by Syed & Li [6] and Majumdar et al. [7]. In the present study, attempts have been made to fabricate a Co layer on the surface of Ti-6Al-4V substrate by direct laser cladding technique with an objective to develop the ball on a stem made of Ti-6Al-4V for hip and femoral prostheses. Attempt has been made to suppress the formation of intermetallics between Co and Ti by application of a thin Cu layer on Ti substrate by electrodeposition technique. A copper interlayer has been used to suppress the interdiffusion of titanium and cobalt and hence, suppressing the formation of a brittle intermetallics [8]. Following fabrication, a detailed investigation of the microstructure, composition, and phase of the fabricated layer has been undertaken. Finally, the wear and corrosion properties of the fabricated part have been studied in details.

## 2. Experimental

In the present study, commercially pure Ti-6Al-4V (of dimensions 15 mm × 15 mm × 5 mm) was chosen as substrate. A thin layer (30 μm thickness) of copper was deposited

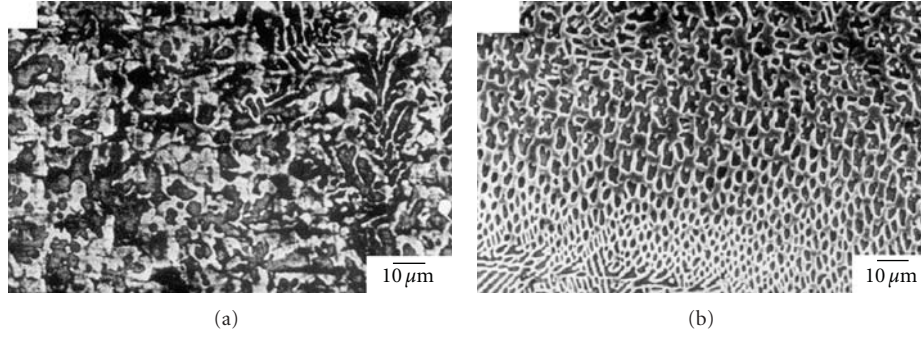


FIGURE 1: Scanning electron micrographs of the alloyed zone formed at the interface of direct laser clad Co on Ti, (a) without Cu and (b) with Cu coating at a thickness of  $30\ \mu\text{m}$ .

TABLE 1: Summary of Young's Modulus of as-received Ti-6Al-4V and direct laser clad Co on Ti-6Al-4V without any interlayer and with a  $30\ \mu\text{m}$  copper interlayer.

Sample history	Young's modulus (GPa)
Ti-6Al-4V	114
Interface of cobalt clad on titanium without copper interlayer	130–150
Interface of cobalt clad on titanium with a $30\ \mu\text{m}$ copper interlayer	140–240

on diamond polished Ti-6Al-4V substrate by electrodeposition. Co layer was developed on the electrodeposited (Ti-6Al-4V substrate using multiple laser cladding technique by pre-deposition of elemental Co powder (of size ranging from  $20\ \mu\text{m}$  and to a thickness of  $500\ \mu\text{m}$ ) by spraying with the desired elemental powder dispersed in alcohol with organic binder and subsequently, laser melting it with a continuous wave  $\text{CO}_2$  laser with an applied power of 1-2 kW and scan speed of 500–1250 mm/min using Ar as shrouding environment. Following the development of clad layer, the microstructures of the clad layer and interface (both on top-surface and cross-sectional plane) were studied by scanning electron microscope (SEM). Compositional distribution was monitored by energy-dispersed X-ray spectroscopy (EDS). Phases present and its distribution were determined by X-ray diffractometer (XRD) using Co- $K\alpha$  radiation. Wear resistance property of the formed layer was studied using a ball-on-plate friction and wear monitor unit (model no.: TR-208-M1) comprising a diamond pyramid indenter rotating on the specimen with a predetermined speed of 15 rpm) and normal load of 1 kg. Kinetics of wear as a function of time under different load was monitored by converting the vertical displacement of the indenter into cumulative wear loss using Winducom 2003 software. The Young's modulus distribution at the interface was carefully analyzed using nanoindentation technique (by application of a triangular pyramid (Berkovich) diamond indenter). TestWorks 4 software for nanoindentation system is used to calculate hardness and Young's modulus from load-displacement graph using the Oliver and Pharr method [9].

Finally, the corrosion behavior of the cross-section of equal segments of clad-alloyed-substrate combinations were carried out in Hank's solution ((g/l): 0.185  $\text{CaCl}_2$ , 0.4 KCl, 0.06  $\text{KH}_2\text{PO}_4$ , 0.1  $\text{MgCl}_2$ ,  $6\text{H}_2\text{O}$ , 0.1  $\text{MgSO}_4 \cdot 7\text{H}_2\text{O}$ , 8 NaCl, 0.35  $\text{NaHCO}_3$ , 0.48  $\text{Na}_2\text{HPO}_4$ , and 1.00 D-glucose) by potentiodynamic cyclic polarization test at a scan rate of 2 mV/s from  $-500$  to  $+5000$  mV(SCE) using standard calomel as reference electrode and platinum as counter electrode [10].

### 3. Results and Discussions

Microstructures play a crucial role in determining the properties and behavior of the components in practical service. In the present study, a detailed investigation of the effect of laser parameters and coating thickness on the morphology of the microstructure was undertaken to optimize the process parameters. Figures 1(a) and 1(b) show the scanning electron micrographs of the alloyed zone formed in direct laser clad Co on Ti, (a) without Cu coating and (b) with Cu coating at a coating thickness of  $30\ \mu\text{m}$ . From Figure 1 it is relevant that the microstructures of the alloyed zone mainly consist of intermetallic phases distributed uniformly all throughout the matrix. The morphology of the microstructures is a mixture of dendrites and cellular. A comparison between Figure 1(a) with Figure 1(b) shows that presence of Cu at the interface, significantly refines the microstructures (As evident from interdendritic arm spacing). The refinement of microstructure due to the application of copper coating is possibly because of a rapid cooling rate associated with a large thermal conductivity of coated copper at the interface. In this regard, it is relevant to mention that the area fraction and nature of precipitates were found to vary with the thickness of Cu coating. However, it was observed that application of a very thick Cu interlayer leads to formation of fine micro cracks in the alloyed zone due to presence of a very large area fraction of intermetallics. A careful analysis of the microstructures and residual stress distribution at the interface shows an optimum coating thickness to be of  $30\ \mu\text{m}$ .

A detailed elemental distribution with depth showed that distribution of Co in the alloyed region is maximum (20 wt%) at the clad layer-alloyed zone interface and

TABLE 2: Corrosion behavior of the dissimilar interface in a 3.56 wt.% NaCl solution.

Sample history	$E_{pp1}$ mV (SCE)	Corrosion rate (mm/year)
Ti-6Al-4V	1300	$1.07 \times 10^{-3}$
Interface of cobalt clad on titanium without copper interlayer	437	$2.43 \times 10^{-3}$
Interface of cobalt clad on titanium with a 30 $\mu$ m copper interlayer	700	$1.26 \times 10^{-3}$

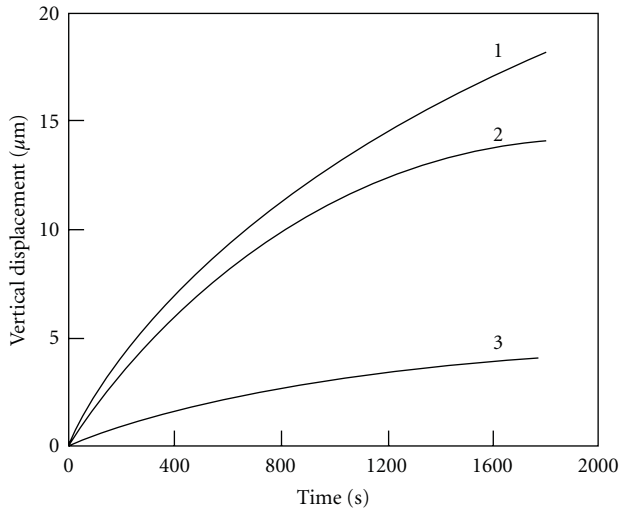


FIGURE 2: Wear profiles of (1) Ti substrate and Co clad Ti lased with laser power density,  $P$  of  $0.212 \text{ kW/mm}^2$  and scan speed,  $v$  of  $14.3 \text{ mm/s}$  for (2) without Cu interlayer and with Cu interlayer with thickness of (3)  $30 \mu\text{m}$  at  $1 \text{ kg}$  load.

decreases gradually with depth reaching a minimum level to 5 wt% at the alloyed zone-substrate interface. Addition of Cu interlayer leads to its melting, intermixing with Ti and Co and changing the composition/microstructures of alloyed zone significantly. A detailed elemental analysis showed that a 10 wt% of Cu was uniformly distributed all throughout the alloyed zone. X-ray diffraction profiles of the interface reveal the presence of intermetallics of Co and Ti ( $\text{Ti}_2\text{Co}$ ). This intermetallic is very brittle and is detrimental to the toughness property of the interface. On the contrary, application of Cu interlayer on Ti prior to laser cladding with Co causes formation of a number of intermetallics between Cu and Ti (mainly  $\text{CuTi}_3$ ,  $\text{Cu}_3\text{Ti}$  and suppresses the formation of  $\text{Ti}_2\text{Co}$  completely, though there was a presence of  $\text{TiCo}_2$  phase at the interface).

Figure 2 shows the wear profiles of (1) Ti substrate and at the interface of Co clad Ti lased with laser power density of  $0.212 \text{ kW/mm}^2$  and scan speed of  $14.3 \text{ mm/s}$  for (2) without Cu interlayer and with Cu interlayer with thickness of (3)  $30 \mu\text{m}$ , respectively. Wear test was carried out with standard Diamond indenter with  $1 \text{ kg}$  load. A relatively lower wear resistance of the interface where, Co was clad on Ti-6Al-4V without any interlayer is attributed to the presence of  $\text{Ti}_2\text{Co}$  which is brittle and hence, leads to spalling effect during abrasive wear against diamond indenter. From plot 3 the effect of Cu interlayer on wear resistance is clearly noted. The excellent wear resistance of  $\text{CuTi}_3$ ,  $\text{Cu}_3\text{Ti}$  protects the formed layer against the dry sliding wear. In addition, the rapidly

solidified homogeneous fine microstructure imparts the coatings good combination of strength and toughness, which also contributes to the excellent resistance of the coating to spallation and delamination during dry sliding wear process. Table 1 summarizes the average Young's modulus of as-received and the interface of the direct laser clad cobalt on titanium without and interlayer and with  $30 \mu\text{m}$  thick copper interlayer. From Table 1 it may be noted that Young's modulus of the interface without the interlayer is increased to 130–150 GPa as compared to as-received Ti-6Al-4V (114 GPa). On the other hand, application of Cu interlayer increases Young's modulus further to a level of 140–240 GPa. Improved Young's modulus due to the application of copper interlayer is attributed to the presence of several Ti-Cu intermetallics (like  $\text{CuTi}_3$ ,  $\text{Cu}_3\text{Ti}$ , etc.).

The corrosion behaviour of the interface was studied using potentiodynamic polarization test. Table 2 represents the results of the potentiodynamic polarization test conducted in Hank's solution for Ti substrate and the interface of laser clad Co on Ti without copper deposition and with copper deposition lased with laser power density of  $0.212 \text{ kW/mm}^2$  and scan speed of  $14.3 \text{ mm/s}$ . The polarization test was conducted in forward cycle to determine the critical potential for pit formation ( $E_{pp1}$ ) values. From Table 1 it is clear that  $E_{pp1}$  value for laser clad Co on Ti with Cu interlayer (700 mV) shows improvement compared to laser clad Co on Ti without Cu interface (437 mV). However, the formation of intermetallics like  $\text{CuTi}_3$ ,  $\text{Cu}_3\text{Ti}$  results in low  $E_{pp1}$  value compared to as-received Ti substrate (1300 mV). The improvement in the pitting corrosion property due to the addition of copper interlayer is attributed to formation of a lower area fraction of precipitates in the later. On the other hand, corrosion rate of interface of cobalt clad titanium without copper interlayer is slightly deteriorated as compared to as-received Ti-6Al-4V. On the other hand, at the interface of cobalt clad on titanium with a  $30 \mu\text{m}$  copper interlayer the corrosion rate is almost similar to Ti-6Al-4V substrate.

#### 4. Conclusions

Direct laser cladding of cobalt on Ti-6Al-4V with and without a copper interlayer was attempted using a continuous wave  $\text{CO}_2$  laser. Graded interface is developed by depositing a thin copper layer on Ti-6Al-4V substrate prior to multiple laser cladding of cobalt on it. Presence of copper interlayer was found to increase both the wear resistance and Young's modulus significantly due to the presence of intermetallics between Ti and Cu ( $\text{CuTi}_3$ ,  $\text{Cu}_3\text{Ti}$ , etc.) which are less brittle as compared to the intermetallics between Ti and Co ( $\text{Ti}_2\text{Co}$ ). Corrosion resistance of the interface in Hank's

solution was marginally deteriorated due to the presence of multiphase in the structure. The degree of deterioration is less where a copper interlayer was applied prior to the direct laser cladding of cobalt on it. The pitting potential was significantly reduced at the interface of direct laser clad cobalt on titanium without any copper interlayer, though marginally reduced in the case where Cu interlayer was applied, which is attributed to a lower area fraction of intermetallic in the structure.

## Acknowledgments

Partial financial support from Department of Science and Technology (DST, New Delhi), Council of Scientific and Industrial Research (CSIR, New Delhi), Board of Research in Nuclear Science (BRNS, Bombay), and Naval Research Board (NRB, New Delhi) are gratefully acknowledged. Technical discussions with Professor I. Manna and Professor A. K. Nath are also gratefully acknowledged.

## References

- [1] Bhat S. V., Ed., *Biomaterials*, Narosa Publishing House, N. Delhi, India, 2002.
- [2] W. M. Steen, *Laser Material Processing*, Springer, New York, NY, USA, 1991.
- [3] J. Dutta Majumdar and I. Manna, "Laser processing of materials," *Sadhana*, vol. 28, no. 3-4, pp. 495-562, 2003.
- [4] F. G. Arcella and F. H. Froes, "Producing titanium aerospace components from powder using laser forming," *Journal of Metals*, vol. 52, no. 5, pp. 28-30, 2000.
- [5] D. Srivastava, I. T. H. Chang, and M. H. Loretto, "The effect of process parameters and heat treatment on the microstructure of direct laser fabricated TiAl alloy samples," *Intermetallics*, vol. 9, no. 12, pp. 1003-1013, 2001.
- [6] W. U. H. Syed and L. Li, "Effects of wire feeding direction and location in multiple layer diode laser direct metal deposition," *Applied Surface Science*, vol. 248, no. 1-4, pp. 518-524, 2005.
- [7] J. D. Majumdar, A. Pinkerton, Z. Liu, I. Manna, and L. Li, "Microstructure characterisation and process optimization of laser assisted rapid fabrication of 316L stainless steel," *Applied Surface Science*, vol. 247, no. 1-4, pp. 320-327, 2005.
- [8] T. B. Massalski, *Binary Alloy Phase Diagrams*, ASM International, Materials Park, Ohio, USA, 1990.
- [9] W. C. Oliver and G. M. Pharr, "Improved technique for determining hardness and elastic modulus using load and displacement sensing indentation experiments," *Journal of Materials Research*, vol. 7, no. 6, pp. 1564-1580, 1992.
- [10] M. G. Fontana, *Corrosion Engineering*, McGraw-Hill, New York, NY, USA, 1987.

## Research Article

# Precise Hole Drilling in PMMA Using 1064 nm Diode Laser CNC Machine

Jinan A. Abdulnabi,<sup>1</sup> Thaier A. Tawfiq,<sup>1</sup> Anwaar A. Al-Dergazly,<sup>2</sup> Ziad A. Taha,<sup>1</sup> and Khalil I. Hajim<sup>1</sup>

<sup>1</sup>Institute of Laser for Postgraduate Studies, University of Baghdad, P.O. Box 47314, Jadriha, Baghdad, Iraq

<sup>2</sup>Laser and Optoelectronics Engineering Department, Al-Nahrain university, Jadriha, Baghdad, Iraq

Correspondence should be addressed to Ziad A. Taha, zddiesel@yahoo.com

Received 30 December 2010; Accepted 21 February 2011

Academic Editor: J. Dutta Majumdar

Copyright © 2011 Jinan A. Abdulnabi et al. This is an open access article distributed under the Creative Commons Attribution License, which permits unrestricted use, distribution, and reproduction in any medium, provided the original work is properly cited.

This paper represents the outcome of efforts that intended to achieve laser hole drilling execution in polymethylmethacrylate (PMMA) of 2.5 mm thickness using 1064 nm diode laser of 5 W output power. Different laser beam powers, exposure time, and positions of the laser spot were taken into consideration with respect to the workpiece. The workpieces were tested in the existence of low-pressure assist gas (20–60 mmHg of air). The experimental results were supported by the predicted results of the analytical model.

## 1. Introduction

The conduction of heat in a three-dimensional solid is given by the solution of the following equation:

$$\rho C_p \frac{\partial T}{\partial t} = \frac{\partial}{\partial x} \left( K \frac{\partial T}{\partial x} \right) + \frac{\partial}{\partial y} \left( K \frac{\partial T}{\partial y} \right) + \frac{\partial}{\partial z} \left( K \frac{\partial T}{\partial z} \right) + A(x, y, z, t), \quad (1)$$

where, the thermal conductivity  $K$  ( $\text{Wcm}^{-1} \text{K}^{-1}$ ), the density  $\rho$  ( $\text{gcm}^{-3}$ ), and the specific heat  $C_p$  ( $\text{Jkg}^{-1} \text{K}^{-1}$ ) are dependent on the temperature and position. The rate of the applied heat to the solid is  $A(x, y, z, t)$  per unit time per unit volume, and  $t$  is the time [1].

Using the cylindrical coordinates  $r$  and  $z$  (Figure 1), the temperature distribution is [1, 2]

$$T(r, z, t) = \frac{P\varepsilon}{2\pi aK} \int_0^\infty J_0(mr)J_1(ma) \times \left\{ \exp(-mz) \operatorname{erfc} \left[ \frac{z}{2(kt)^{1/2}} - m(-kt)^{1/2} \right] - \exp(mz) \operatorname{erfc} \left[ \frac{z}{2(kt)^{1/2}} + m(kt)^{1/2} \right] \right\} \frac{dm}{m} + T_0,$$

where,  $r$  is the radial coordinate (hole radius),  $z$  is the axial coordinate (thermal penetration depth),  $J_0$  and  $J_1$  are Bessel functions of the first kind,  $P$  is the constant power during a laser pulse,  $a$  is the radius of the laser spot at the surface,  $K$  is the thermal conductivity of the material,  $k$  is the thermal diffusivity,  $\varepsilon$  is the fraction of incident radiation absorbed,  $m$  is an integer that represents the limit of integration,  $t$  is the exposure time, and  $T_0$  is the initial temperature.

The numerical solution of (2) for determining the temperature distribution as a function of time at any point

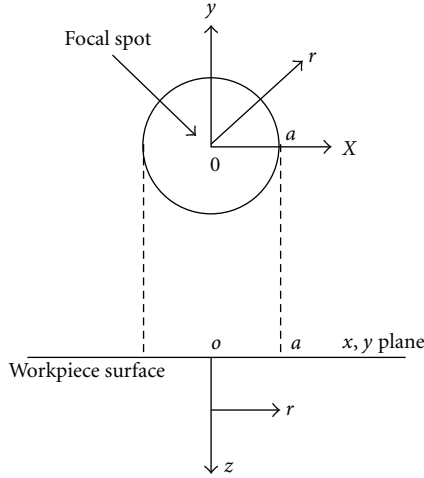


FIGURE 1: Coordinate system [1].

inside the material along the Z-axis for  $r = 0$  is given by [1, 2]

$$T(0, z, t) = \frac{2P\varepsilon(kt)^{1/2}}{\pi a^2 K} \left\{ i \operatorname{erfc} \left[ \frac{z}{2(kt)^{1/2}} \right] - i \operatorname{erfc} \left[ \frac{(z^2 + a^2)^{1/2}}{2(kt)^{1/2}} \right] \right\} + T_0. \quad (3)$$

The dimensionless variables for temperature and time, respectively are defined as [1, 2]

$$\theta = \frac{TaK\pi}{P\varepsilon}, \quad (4)$$

$$\Gamma = \frac{2(kt)^{1/2}}{a}. \quad (5)$$

Hence, (3) becomes

$$\theta(0, z, \tau) = \Gamma \left[ i \operatorname{erfc} \frac{z}{a\Gamma} - i \operatorname{erfc} \frac{(z^2 + a^2)^{1/2}}{a\Gamma} \right] + T_0. \quad (6)$$

For steady-state condition at any depth below or at the center of the focal spot,  $t \rightarrow \infty$  in (6) [1, 2]

$$T(0, 0, t) = \frac{2P\varepsilon(kt)^{1/2}}{\pi a^2 K} \left\{ \frac{1}{\pi^{1/2}} - i \operatorname{erfc} \left[ \frac{a}{2(Kt)^{1/2}} \right] \right\} + T_0 \quad (7)$$

$$\theta(0, z, \infty) = \frac{1}{a} \left[ (z^2 + a^2)^{1/2} - z \right]. \quad (8)$$

This implies that the maximum surface temperature attainable is given by [1]

$$T(0, 0, \infty) = \frac{P\varepsilon}{\pi a K}. \quad (9)$$

Figure 2 illustrates a plot diagram for (6) as the variation of the dimensionless temperature  $\theta$  with  $\tau = \Gamma^2 = 4kt/a^2$  and

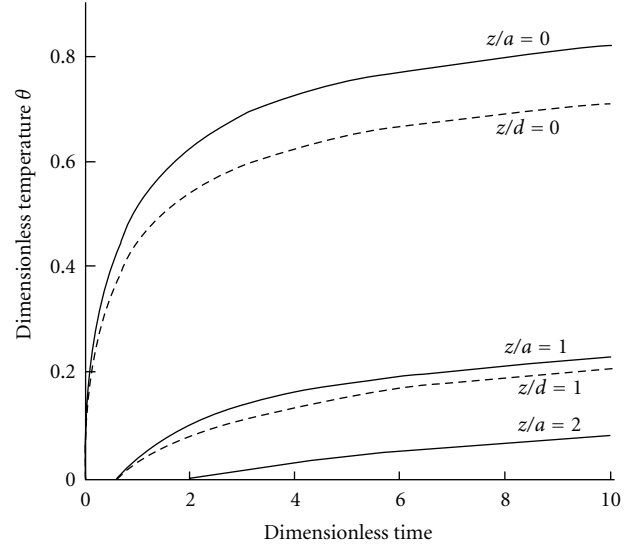


FIGURE 2: Dimensionless temperature  $\theta$  versus dimensionless time for various depths when heating with continuous disk (—) and Gaussian (--) sources [1].

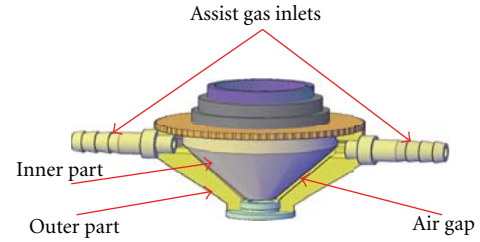


FIGURE 3: The designed nozzle.

depth below the focal spot. The temperature rises rapidly at first and approaches 75% of its steady-state value within  $\tau = 4$  or  $t = a^2/k$ , then the change in temperature with time proceeds at a progressively decreasing rate. The time  $t = a^2/K$  can, therefore, be considered as the thermal time constant [1].

## 2. Experimental Work

A special nozzle for the laser head was designed and constructed for achieving the optimum performance as shown in Figure 3.

In the absence of the assist gas nozzle, the output power of the laser head was 2.75 W as examined by a power meter type (Gentec TPM 300 CE) as an average value of the output power. In this work, the nozzle was designed in a way that acts as a normal assist gas nozzle and as an assist gas nozzle with variable orifice diameters (with a changeable nozzle tips of 0.4, 0.6, 0.8, 1, 1.2, 1.5, and 3.0 mm in diameters), as shown in Figure 4, that were used as an apertures (placed at the waist of the collimating lens [3, 4]) to allow choosing various values of the laser beam output power and suppress the higher-order modes.



FIGURE 4: The assist gas nozzle and the seven different tips.

TABLE 1: The theoretical values of the aspect and taper ratios at different powers.

Power (W)	Hole Diameter mm		Aspect Ratio $A_r$	Taper Ratio $T_r$
	Inlet	Outlet		
2.45	0.700	0.300	3.571	0.428
1.82	0.650	0.200	3.846	0.308
0.96	0.500	0.200	5.0	0.400

All the workpieces were illuminated by the laser beam for many different time periods in order to reach the vaporization temperature and executing drilling process. The drilling process was examined for different laser spot positions (at the surface, at the mid surface, and at the lower surface), without the use of assist gas, and with the assist gas (the used pressures were 20, 30, 40, 50, and 60 mmHg).

Figure 5 shows the values of the aspect ratio (depth to diameter) and the taper ratio (outlet to inlet diameter) using laser power of 2.45 W, the focal position at the surface of the workpiece, and the assist gas pressure of 20 mmHg for 11 exposures time.

Figures 8, 9, and 10 illustrate the temperature distributions for different working conditions.

### 3. Simulation Results

The maximum temperature in the center of the focus at the surface was measured from (7). This temperature was substitute in (2) for each used output laser power with the rest values mentioned in this equation ( $a, K, k, t, \dots$ , etc.) and plotting the temperature distribution. The value of  $t$  that substituted in (2) was measured as the thermal time constant ( $t = a^2/k$ ) for  $z$  below the focal spot. This  $t$  represents the maximum exposure time needed for the material to reach the vaporization temperature over which the heat diffused inside the material and not along the depth. This value of  $t$  was used for the rest stages of the drilling process. The hole depth was measured using the plot diagram and substituted in (8) for determining  $\theta$ . This  $\theta$  was substituted in (4) for determining the maximum temperature at this depth, which will be considered as the new surface. The newly measured

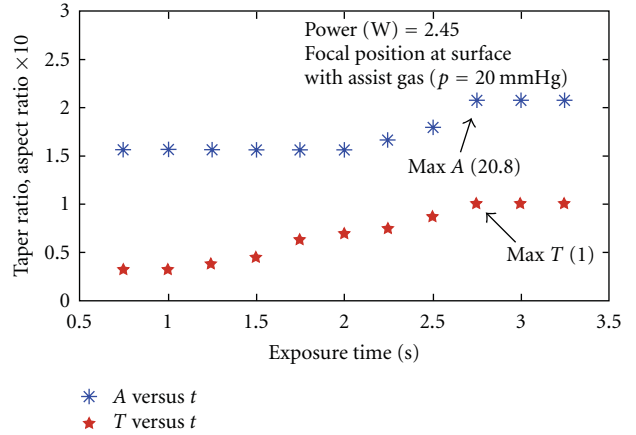


FIGURE 5: Different holes drilled by  $P = 2.45$  W, focal position at the surface, and with 20 mmHg of assist gas.

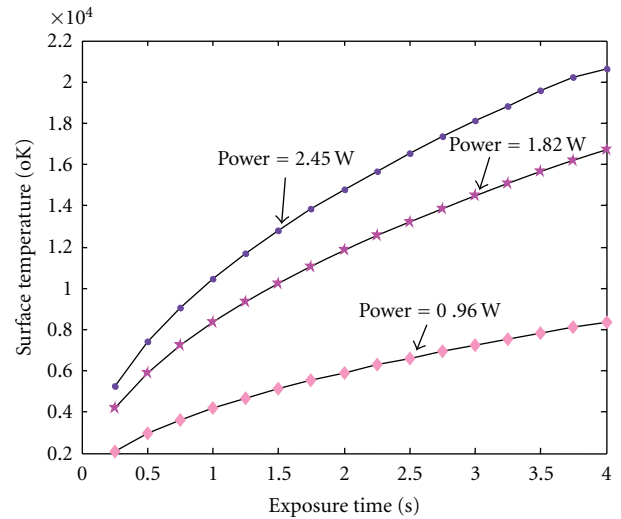


FIGURE 6: The laser beam exposure time versus the surface temperature.

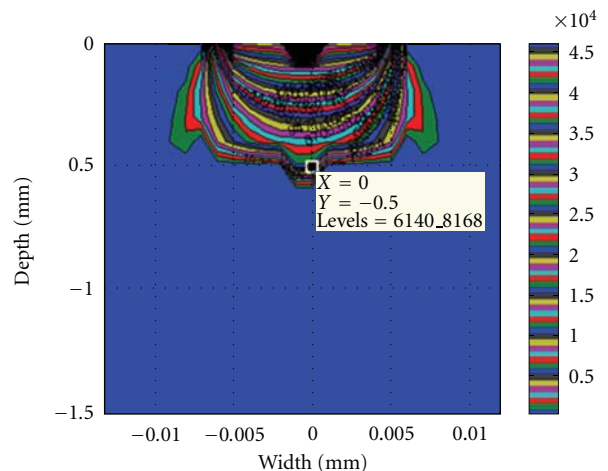


FIGURE 7: The hole depth versus the hole radius.

TABLE 2: The different experimental values of  $A_r$  and  $T_r$  at different working conditions.

Power (W)	Focal position	Taper ratio	Taper exposure time (s)	Aspect ratio	Aspect exposure time (s)	Assist gas pressure (mmHg)
2.45	At surface	1	2.75	20.8	2.75	20
=	=	1	2.5	16.6	2.5	30
=	=	1	2.5	20.8	1.75	40
=	=	0.9	3	22.2	0.75	50
=	=	0.9	0.75	22.7	0.75	60
=	At mid surface	1	1.75	16.6	1.5	20
=	=	0.8	1.75	3.7	1.25	30
=	=	1	1.25	17.8	1.25	40
=	=	0.9	3.5	4	3.5	50
=	=	0.9	3.75	7.8	3.5	60
=	At lower surface	0.43	1.75	4.3	1.75	20
=	=	0.54	3.75	4.5	3.75	30
=	=	0.6	4	4.5	3.75	40
=	=	0.37	1.5	4.5	4	50
=	=	0.4	4	4.4	0.75	60
=	=	1	0.75	31	0.75	70
2.45	At surface	0.48	3.75	3.3	2	Non
=	At mid surface	0.5	3.5	4	2	=
=	At lower surface	0.6	3.75	3.5	2	=
1.82	At surface	0.5	3.75	3.5	2.5	=
0.96	At surface	0.56	3.25	5	2.5	=

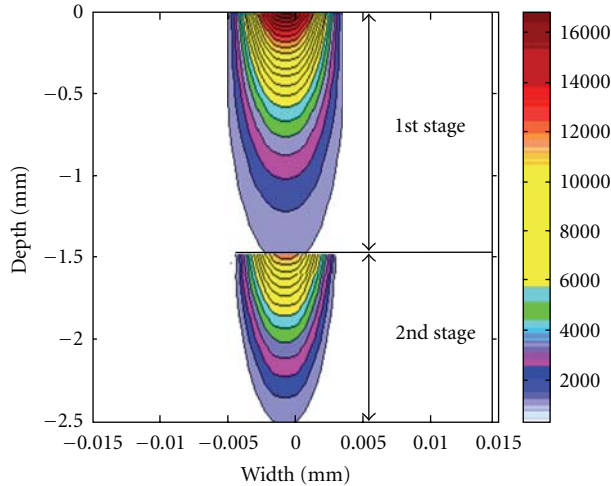


FIGURE 8: The first-stage temperature distribution; exposure time (s) = 2.25, total power (W) = 2.45, and surface temperature =  $1.5364e + 004$ . The second-stage temperature distribution; exposure time (s) = 2.25, total power (W) = 0.3528, and surface temperature =  $2.2124e + 003$ .

temperature was substituted in (9) for measuring the new laser power at this depth. The above-mentioned steps were followed again many times until the hole covered the whole thickness of the workpiece. Knowing that each time the new thickness was added to the depth of the previous stage and then substituted in (2).

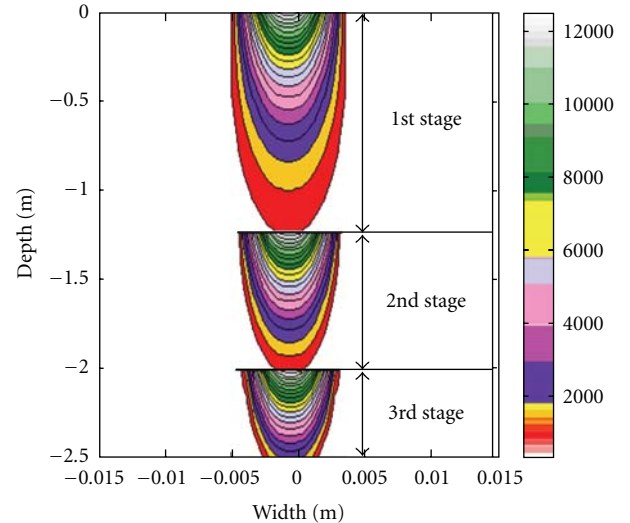


FIGURE 9: The first-stage temperature distribution; exposure time (s) = 2.25, total power (W) = 1.82, and surface temperature =  $1.1413e + 004$ . The second-stage temperature distribution; exposure time (s) = 2.25, total power (W) = 0.2953, and surface temperature =  $1.8518e + 003$ . The third-stage temperature distribution; exposure time (s) = 2.25, Total power (W) = 0.19, and surface temperature =  $1.2559e + 003$ .

#### 4. Results and Discussion

The analytical steps were followed for laser output powers 2.45 W, 1.82 W, and 0.96 W using the nozzle orifices of 3 mm, 1.5 mm, and 1.2 mm, the spot radius measured as

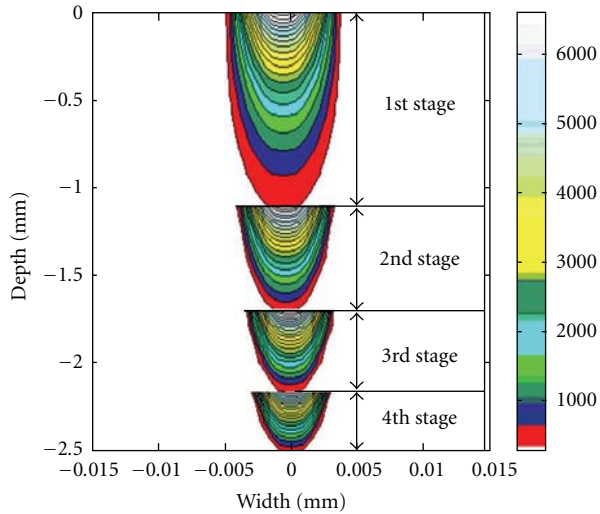


FIGURE 10: The first-stage temperature distribution; exposure time ( $s$ ) = 2.25, total power ( $W$ ) = 0.96, and surface temperature =  $6.0201e + 003$ . The second-stage temperature distribution; exposure time ( $s$ ) = 2.25, total power ( $W$ ) = 0.1782, and surface temperature =  $1.1175e + 003$ . The third-stage temperature distribution; exposure time ( $s$ ) = 2.25, total power ( $W$ ) = 0.19, and surface temperature =  $1.2559e + 003$ . The fourth-stage temperature distribution; exposure time ( $s$ ) = 2.25, total power ( $W$ ) = 0.0989, and surface temperature = 620.196.

0.5 mm, The thermal time constant  $t$  was 2.25 s,  $K$  of the workpiece material (PMMA)  $0.2 \times 10^{-3} \text{ W mm}^{-1} \text{ }^\circ\text{K}^{-1}$ ,  $k$  of the workpiece material is  $0.11 \text{ mm}^2 \text{ s}^{-1}$ , and the reflectivity  $R$  of the workpiece material was assumed as 0.01. Therefore, the emissivity of the surface of the workpiece  $\varepsilon = 1 - R = 0.99$ , and the exposure time versus the surface temperature was plotted for each of the used powers, 2.45 W, 1.82 W, and 0.96 W as shown in Figure 6.

A MATLAB package was used for presenting the case under study. For one stage drilling process, it was found that whatever the increase in the exposure time the hole did not exceed certain depth of the whole thickness of the workpiece and the heat was diffused (dissipated) inside the material and not along the depth (Figure 7).

The aspect ratio (ratio of depth to diameter) and the taper ratio (ratio of outlet to inlet diameter) of the drilled holes by using laser beam powers; 2.45 W, 1.82 W, and 0.96 W as measured from Figures 8, 9, and 10 are listed in Table 1.

These values of  $A_r$  and  $T_r$  clarify that irradiating PMMA workpiece of 2.5 mm thickness by 1064 nm CW diode laser of 1 W output power and exposure time of 2.25 s leads to achieving an acceptable quality of the hole drilling process that matches the most improved values represented by the highest aspect ratio (20–30) and lowest taper ratio ( $\approx 1$ ) [5, 6].

## 5. Conclusion

The experimental results for different working conditions that were illustrated in Table 2 show that without the use of the assist gas the best holes can be achieved by focusing

almost of 1 W laser output power on the surface of the chosen workpiece material for about 2.5 s which matches with the best result of the analytical model as shown in the last row of the table.

Moreover, the use of the low-pressure assist gas of about 60 mmHg with laser output power of 2.45 W and focusing the spot on the surface of the workpiece enhanced the drilling process and reduced the required exposure time. Therefore, this study concluded that for executing laser hole drilling process in black acrylic (PMMA) material of 2.5 mm thickness using CW diode laser of low laser output power around 1 W with the absence of the assist gas, the focal position represents the most affecting parameter for getting best results (highest aspect ratio and lowest taper ratio) while when using higher laser output power of 2.45 W with the existence of the assist gas, the most affecting parameters are the assist gas pressure and focal position.

## References

- [1] W. W. Duley, *CO<sub>2</sub> Laser Effects and Applications*, Academic Press, New York, NY, USA, 1976.
- [2] H. S. Carslaw and J. C. Jaeger, *Conduction of Heat in Solids*, Oxford Press, Oxford, UK, 1969.
- [3] R. Menzel, *Photonics, Linear and Nonlinear Interaction of Light and Matter*, Springer, Berlin, Germany, 2001.
- [4] J. F. Ready, *LIA Handbook of Laser Materials Processing*, Laser Institute of America, Magnolia Publishing, Orlando, Fla, USA, 2001.
- [5] H. El-Hofy, *Advanced Machining Processes, Nontraditional and Hybrid Machining Processes*, Production Engineering Department, Alexandria University, Alexandria, Egypt, 2005.
- [6] W. M. Steen, *Laser Material Processing*, Springer, London, UK, 2nd edition, 1998.

## Review Article

# The Fabrication of Automobile Components by Applying Electromagnetic Stirring in Semisolid Process

H. H. Kim<sup>1</sup> and C. G. Kang<sup>2</sup>

<sup>1</sup> Precision Manufacturing Systems Division, Pusan National University, Pusan 609-735, Republic of Korea

<sup>2</sup> School of Mechanical Engineering, Pusan National University, Pusan 609-735, Republic of Korea

Correspondence should be addressed to C. G. Kang, cgkang@pusan.ac.kr

Received 1 September 2010; Accepted 19 November 2010

Academic Editor: Shoujin Sun

Copyright © 2011 H. H. Kim and C. G. Kang. This is an open access article distributed under the Creative Commons Attribution License, which permits unrestricted use, distribution, and reproduction in any medium, provided the original work is properly cited.

This paper describes a rheo-forming process for the development of automobile components, such as knuckle, by using rheology material with electromagnetic stirring (EMS) system equipment. The effects of several process and metallurgy parameters such as stirring current, stirring time, pouring temperature, forming pressure, tip velocity, fraction of primary phase, and its morphology and distribution, on the final products are reviewed and discussed. A variety of simulation studies are conducted. In addition, the effect of the vacuum-assisted method on the performance of rheo-forged products is introduced. The EMS is an effective process to improve a feed stock in the rheo-forming process with improved mechanical properties.

## 1. Introduction

Recently, the car industry has required lightweight parts to improve gas mileage and mitigate the impact of damaging emissions on the environment, which are thought to contribute to depleting the ozone layer, increasing greenhouse gases, and producing acid rain [1, 2]. Forming processes such as casting and forging, hot forging, and low-pressure casting have allowed lightweight aluminum alloy-based component to be used in passenger cars, but they have not been adapted to mass-production due to a lack of product reliability, increased costs, and excessive initial investment.

The die casting process, that is, the forming process that fills mold cavities with molten metal, has advantages for the mass production of thin parts with complex shapes which have little need for mechanical strength. However, the process is inappropriate for producing parts with high strength requirements because defects such as turbulent flow-induced air entrapment could result as the melt flows into the mold cavities [3]. Moreover, the forging process has several limitations in producing precise parts and productivity because the forming process has multiple steps. Conversely, the mechanical properties of the parts appear to be uniform and stable [4].

Therefore, the electromagnetic stirring forming process, which is capable of producing light automobile parts with high strength, has been required to promote low mechanical properties of parts [5, 6]. Electromagnetic stirring (EMS) is a process that modifies the microstructure of alloy before or during the forming process. These microstructures are created during solidification to spherical primary  $\alpha$ -Al phase particles and distributed into the eutectic phase by strongly stirring the molten metal at the initial stage of solidification.

This paper describes a rheo-forming process for the development of automobile components by using rheology material with EMS system equipment such as knuckle, arm and special designed bracket module. In addition, the effect of the vacuum-assisted method on the performance of rheo-forged products was introduced.

## 2. Fabrication of Arm Component Medium-Pressure Type with EMS

*2.1. Apparatus for Electromagnetic Stirring.* This study obtains the experimental data applicable to the forming process of the resulting products to be produced by electromagnetic stirring in terms of investigation of the relation

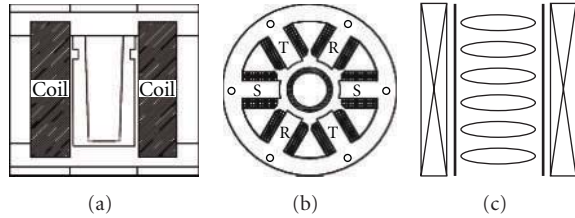


FIGURE 1: The schematic diagram of the apparatus with electromagnetic stirrer: (a) Front view of EMS, (b) top view, (c) stirring direction.

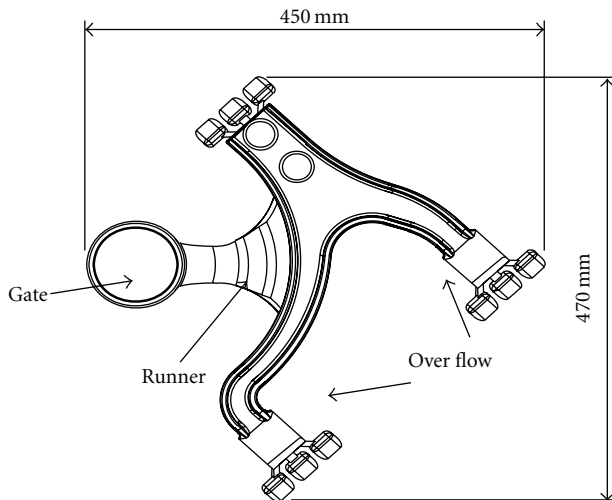


FIGURE 2: Geometry of runner system and arm part.

between the properties of A356 alloys. This includes primary  $\alpha$ -Al phase particle sizes, their distribution state, spherical structures and electromagnetic stirring current and time. An electromagnetic stirrer is classified with a vertical and horizontal stirrer. In this study, a horizontal electromagnetic stirrer was employed to get experimental data, and the schematic electromagnetic stirrer used in this experiment was illustrated in Figure 1(a). The horizontal electromagnetic stirrer used in this study was manufactured so as to contain three phases and three poles, with each phase located circumferentially so that the current flows through the coils, as shown in Figure 1(b). The electromagnetic force appears to arise toward the circumferential direction, as shown in Figure 1(c). To manufacture the electromagnetic stirrer used in this work, the design and manufacture of the core to fix the coil were completed first. The core holds the coil that is wound to the core, which is in turn fabricated to laminate the 0.35-mm-thick steel plate.

**2.2. Mold Design and Simulation.** This study adopted the Ostwald-de Waele rheology model. Taking into consideration these characteristics of electromagnetic stirring, mold design of arm parts was prepared using MAGMASoft (casting analysis code) and was optimized with prediction of casting defects through filling analysis and solidification. Then, the design plan was applied to manufacturing the mold used in this study.

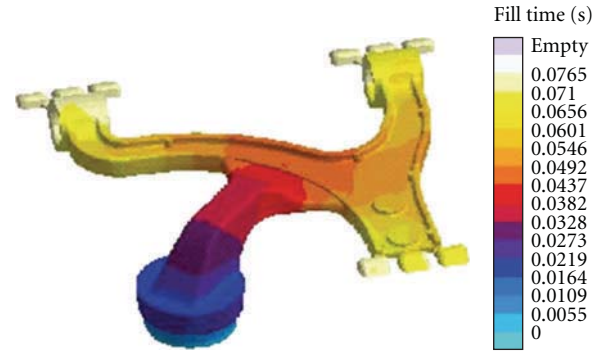


FIGURE 3: Filling time distribution of arm part.



FIGURE 4: Solidification time distribution of arm part.

Figure 2 depicts a runner system including the geometry of a gate and an overflow. Figure 3 shows distribution of filling time of arm products into mold cavity. The filling time, the passing time through the gate, and the time for filling the mold cavity of products are 0.074, 0.0437, and 0.0327 s, respectively. Figure 3 shows the filling time distribution of arm parts. Change in melt flows in the cavity as a function of filling time found that good filling behavior is achieved with completion of overflow. In addition, temperature deviation of melts in the cavity resulted within  $3^{\circ}\text{C}$  due to the short period of filling. In addition, the final filling is completed with the minimum temperature of melt in the cavity of  $609^{\circ}\text{C}$  and solid fraction of 75%. Figure 4 shows the distribution of solidification time of arm products. The final solidification was completed in 66.9 s, and solidification of product parts was also completed in 16.37 s after the final filling. Also, directional solidification from product parts to gate parts took place. Utilizing these results, the forming condition of practical products like pressing time after filling was obtained. Figure 5(a) shows the distribution of hotspots in the arm products. Hotspots were mostly distributed at the gate and the overflow due to directional solidification toward the gate. As illustrated in Figure 5(b), a heating line was facilitated surrounding the arm products for the prevention of the lowering of the temperature and control of solidification and stabilization in the temperature of the mold since shrink pores may take place at locations having formation of hotspots.

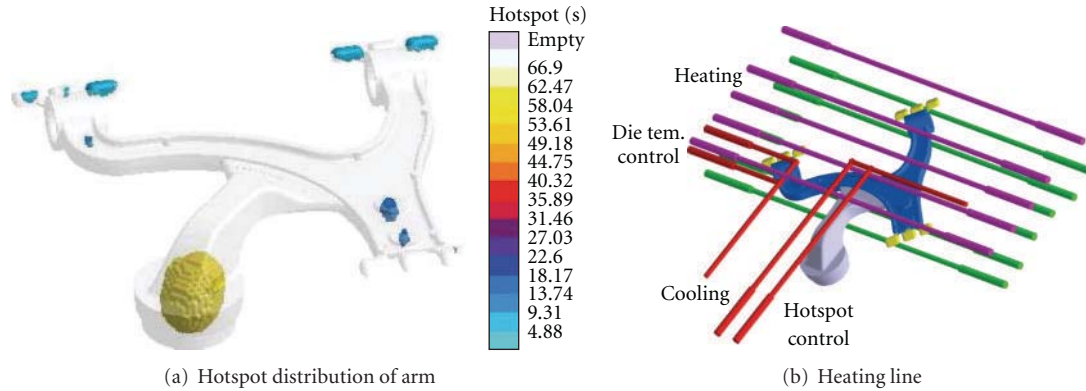


FIGURE 5: Hotspot distribution of arm part and heating line.

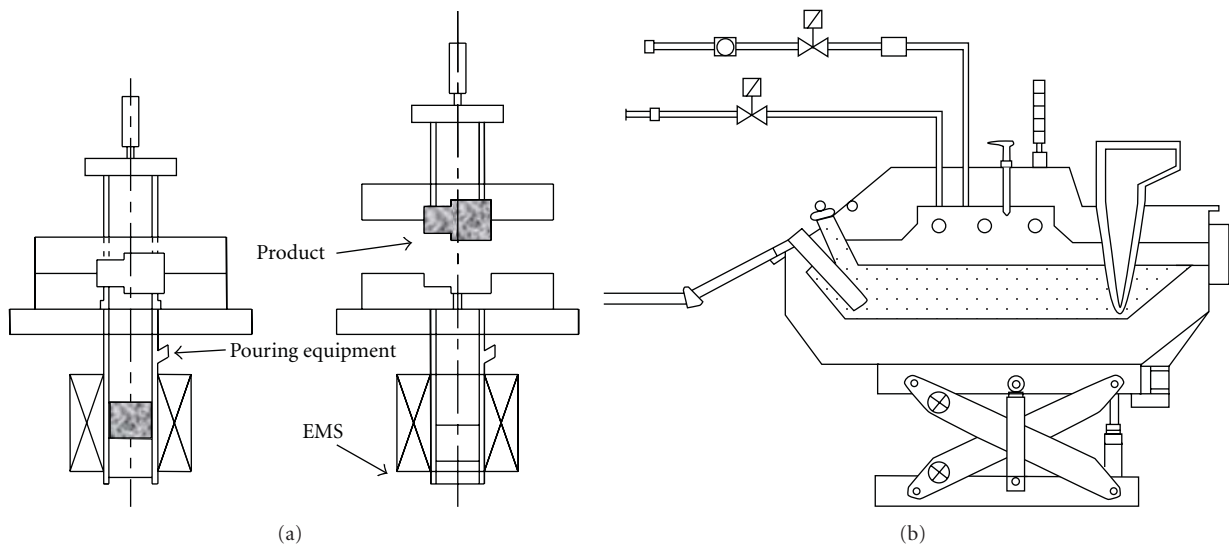


FIGURE 6: Schematic diagram for casting with EMS: (a) medium vertical die casting press; (b) continuous pouring of molten alloy (Al dosing furnace).

2.3. Results of Arm Fabrication by Rheo-Casting. Manufacturing sleeves is important in the forming process utilizing electromagnetic stirrers. Nonmagnetic material 19%Cr–9%Ni STS 304 is currently used as a sleeve. STS 304 was selected as a sleeve material since the characteristics of STS 304 provides nonmagnetic properties at room temperature and good machinability. The inner and outer diameters of the sleeve are 80 and 130 mm, respectively. Figure 6 illustrates a schematic diagram for casting with EMS.

Figure 7 shows photographs of arm products formed by EMS in terms of each forming condition. In the case of pressure of 300 bar ( $300 \text{ bar} \times 14.5 \text{ psi} \times 0.001 \times 5.895 \text{ MPa} = 26 \text{ MPa}$ ) and a speed of 0.2 m/s, insufficient forming of products due to solidification of melt during filling into the cavity took place and surface quality was not acceptable due to a lack of transfer of filling pressure to the cavity. With injection speed at a range of 0.2–0.3 m/s, sufficient products were obtained and good surface quality was achieved. In the case of an increase of injection speed up to 0.3–0.5 m/s, the melt spread into the parting line of the mold due to

high-speed filling and surface quality of products was not achieved. Surface quality of products was found to be better with an increase of injection pressure with an increase of forming pressure to 450 bar to investigate the effect of forming pressure.

Figure 8(b) shows microstructures at each position according to each point as depicted in Figure 8(a). The samples of arm products were formed with EMS at 60 A for 10 s and were sized with 5 mm long and 5 mm wide. As a result of microstructural observation, it was found that the primary  $\alpha$ -Al phase particles were uniformly distributed through entire products and the distributed primary  $\alpha$ -Al phase particles reached fine and globularly.

### 3. Fabrication of Tower Sprocket Component by EMS Rheo-Casting

3.1. Procedure of Rheo-Forming. In this experiment, A356 aluminum alloy was used for making slurry with the same EMS system (Section 2.1).

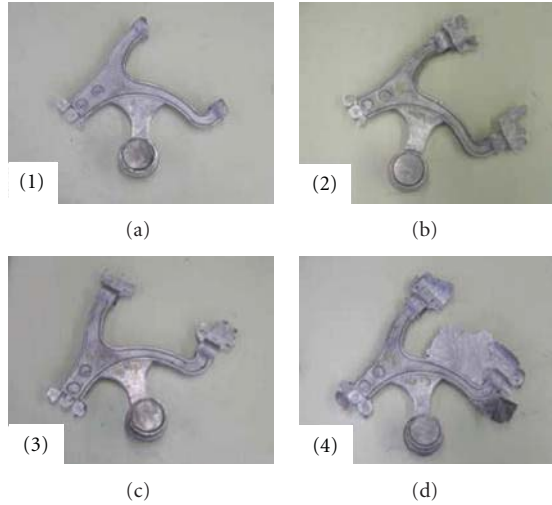


FIGURE 7: Photographs of arm part according to velocity and pressure (at 75% solid fraction): (1) 0.2 m/s and 300 bar; (2) 0.3 m/s and 300 bar; (3) 0.3 m/s and 450 bar; (4) 0.5 m/s and 450 bar.

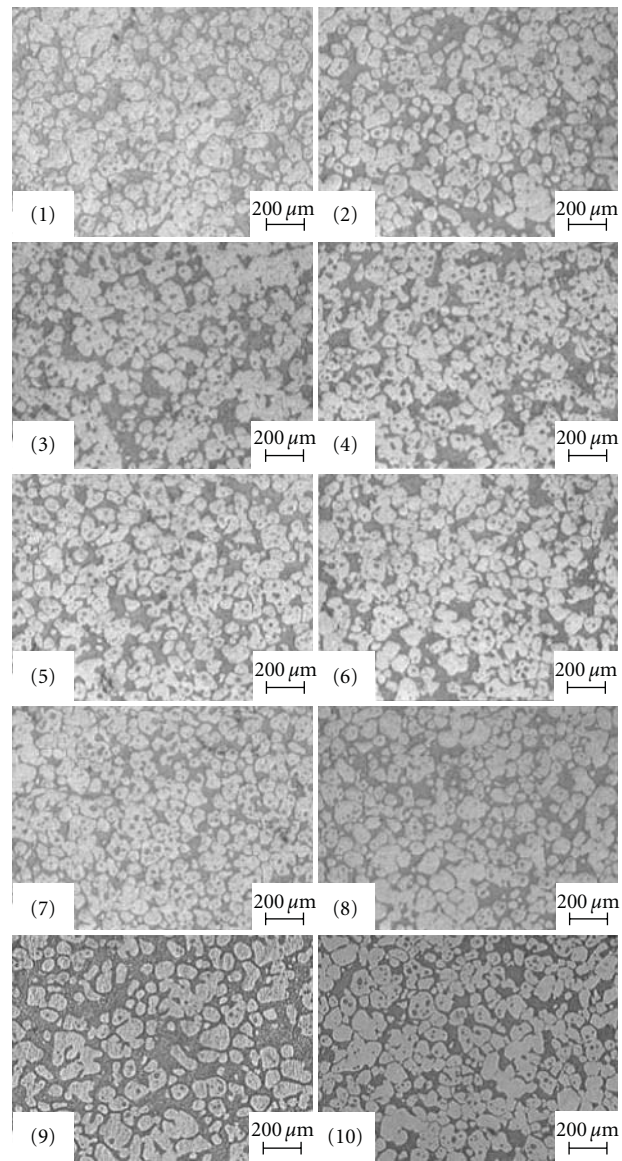
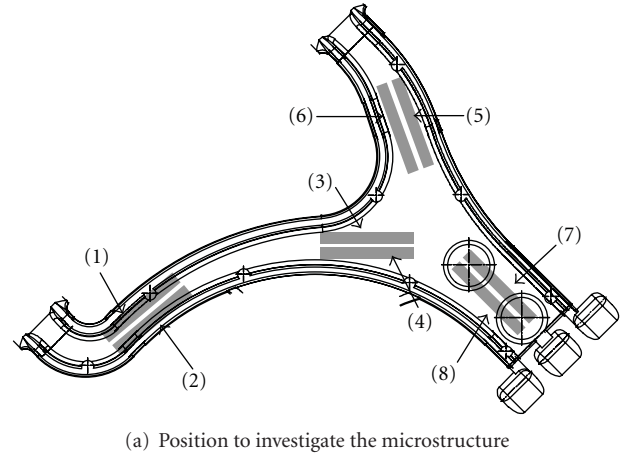
TABLE 1: The conditions of rheo-casting process.

No.	Casting pressure (MPa)	Low velocity ( $V_L$ ) (m/s)	High velocity ( $V_H$ ) (m/s)
1	35	0.1	0.3
2	35	0.1	0.5
3	35	0.1	0.7
4	35	0.1	1.0
5	20	0.1	1.0
6	35	0.1	1.0
7	50	0.1	1.0
8	60	0.1	1.0

Figure 9 shows a location of rheological material and the tip in the sleeve at both low velocity and high velocity. After putting solid fraction-controlled (20% and 50%) rheological material into the cavity and combining shot sleeve and lower mold with concentration, the tip velocity maintains to be low so as to reduce entrapment of air bubbles while the rheological material arrives to gate entrance. The movement of tip is kept to be high velocity so that the segregation of the solid and liquid phase is prevented by quickly forwarding the tip as soon as the material passes the gate entrance. In this study, therefore, the experiment was evaluated with regard to low velocity of  $V_L = 0.1$  m/sec and high velocity of the tip movement ranging from  $V_H = 0.3$  m/sec to 1.0 m/sec, as shown in Table 1.

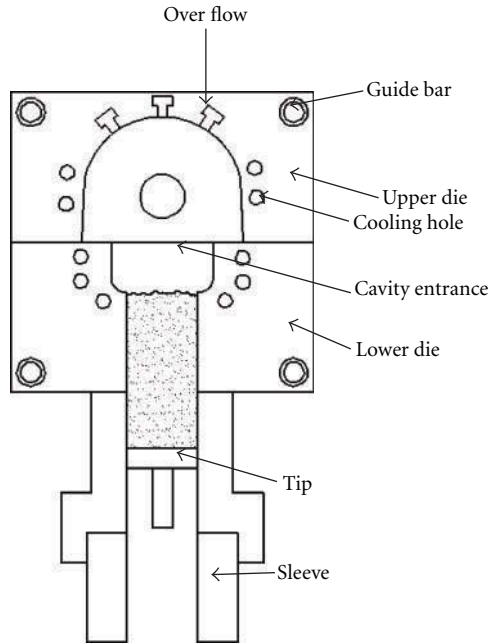
### 3.2. Results of Tower Sprocket Fabrication by Rheo-Casting.

Figures 10(a) to 10(d) show the filling behaviors when the velocities of injection are low velocity of  $V_L = 0.1$  m/sec at solid fraction  $f_s = 0.5$  and high velocity of  $V_H = 0.3$  m/sec to  $V_H = 1.0$  m/sec. No filling parts were observed at the high injection velocity of 0.3, 0.5, and 0.7 m/sec. The filling was only completed at  $V_L = 0.1$  m/sec and  $V_H = 1.0$  m/sec, as

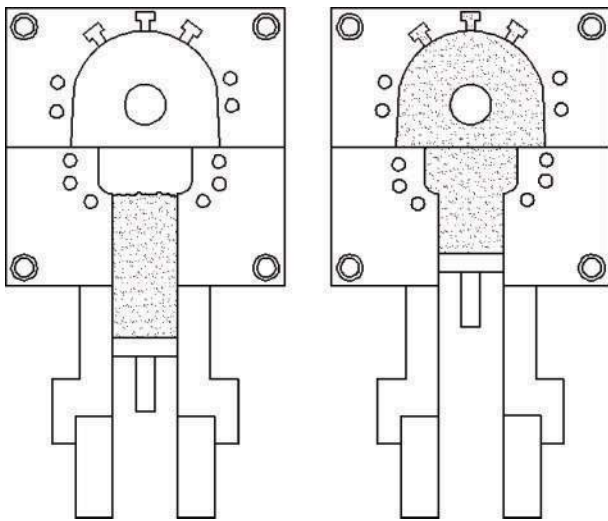


(b) microstructure at each position

FIGURE 8: Microstructures at each position according to each point ( $C = 60$  A,  $t_s = 10$  s and solid fraction of 75%).



(a) Pouring and contact between lower die and shot sleeve



(b) Movement of the tip by low velocity until meniscus of the melt arrives at the die entrance

FIGURE 9: The plunger position for variation of velocity.

shown in Figure 10(d). Thus, the casting parameters for the case of Figure 10(d) were used to obtain the complete cast product. As shown in Table 1, after completing to fill the die cavity, pressure of injection was controlled by maximum pressure of 60 MPa so that microstructure of the part is refined.

Figure 11 shows the external appearance of products formed under the condition,  $V_L = 0.1$  m/sec,  $f_s = 0.2$ , and  $V_H = 1.0$  m/sec, which was optimized to obtain the sound product through the preliminary experiment carried out in this study. The thickness of side part of the product is 6mm and the total weight of the net product is 1.61 kg without gate part which occupies 40% of the product.

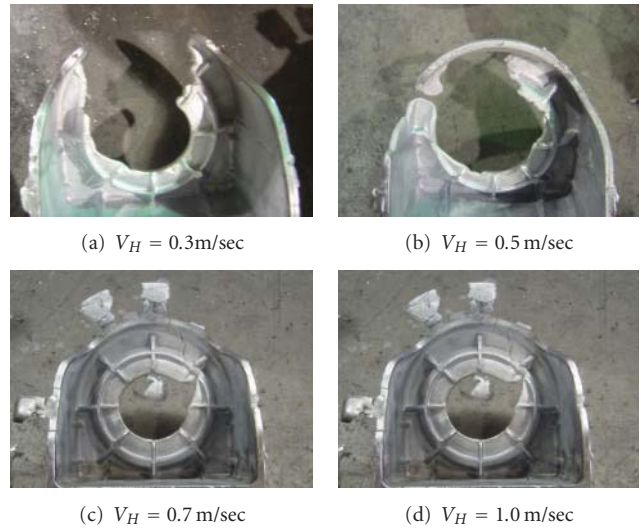


FIGURE 10: Photograph of fabricated part according to injection velocity in high-speed zone ( $V_L = 0.1$  m/sec, Solid fraction: 50%)



FIGURE 11: A photograph of products fabricated by vertical type squeeze machine ( $V_L = 0.1$  m/sec  $V_H = 1.0$  m/sec, Solid fraction: 20%).

In this study, the shape of the cast product was selected to be channel shape structure which has complicate shape and rapidly changing direction of the melt flow. Through conventional rheology die casting process, it is considerably difficult to obtain the cast product which has the uniform solid fraction over the entire product. Therefore, squeeze casting process of rheological material developed in this study is suitable for forming the complex part.

Figure 12 shows photographs showing the fine microstructure of the product which were fabricated at  $V_L = 0.1$  m/sec,  $V_H = 1.0$  m/sec,  $f_s = 0.2$ . Dendrite phases for the product fabricated at solid fraction,  $f_s = 0.2$ , were hardly shown. Because the branch of the dendrite might be crushed by EMS, the globularized phases were shown compared to the product fabricated at  $f_s = 0.0$ . However, globularized microstructure of the product obtained from vertical squeeze casting process was quite different from that of the product directly obtained from EMS. It may be due to the fact that the melt flow in the die cavity did not smoothly occur because the product, that is, die cavity was the complicated thin plate in channel shape. During the EMS, control of the solid fraction is associated with reduction in temperature of the melt arising from convective heat transfer. The effect of EMS, which plays a role on crushing and refinement of dendrites,

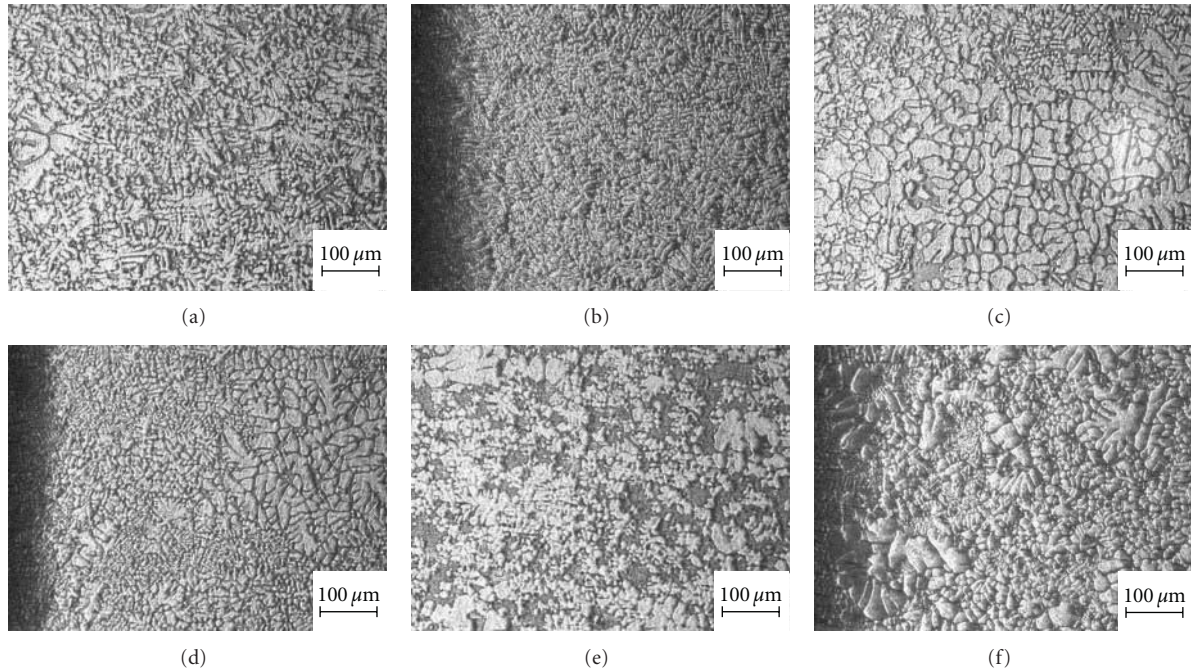


FIGURE 12: Microstructures of fabricated part by rheo-casting:  $V_L = 0.1$  m/sec,  $V_H = 1.0$  m/sec, Solid fraction: 20%.

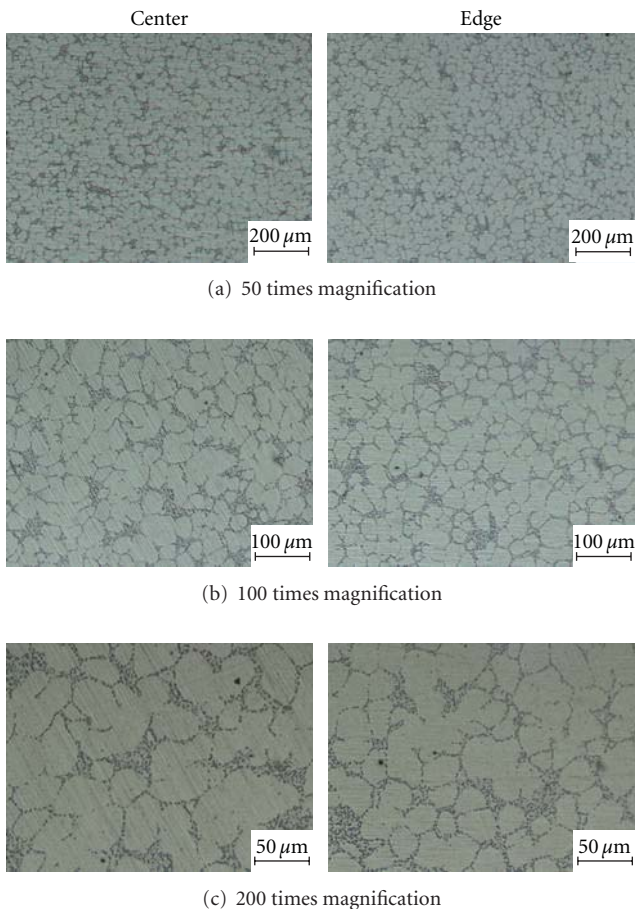


FIGURE 13: Microstructure of rheology material (70% solid fraction).

was considerably weak because EMS was conducted for short time in order to get the melt with the low solid fraction.

#### 4. Fabrication of Module Bracket by EMS Rheo-Casting

**4.1. Fabrication of Slurry by EMS.** In this experiment, A356 aluminum alloy was used for making slurry with the same EMS system (Section 2.1). Figure 13 shows a microstructure of rheological material. Uniformed and globular microstructure was well distributed.

**4.2. Mold Design and Simulation with MAGMASoft.** To produce a module bracket using EMS, an optimal module bracket mold was designed by using a computer program to predict product defects by analyzing filling and solidification as shown Figures 14 and 15. The melt is filled from center to edge.

The possibility happening of shrinkage was high at spot regions. However, shrinkage will be removed due to direct pressure at center position by punch.

**4.3. Inspection of Fabricated Module Bracket.** Figure 16 is a fabricated sample by rheo-casting. Overall, there are no unfilling region and surface crack. To investigate the internal defect and particles distribution, observation of microstructure was conducted by optical microscope as shown in Figure 17. Overall, macroporosities were not founded. However, dendrite structures and liquid segregations were founded at regions 3 and 4. Liquid segregation and dendrite structure cannot be controlled in liquid phase. The primary  $\alpha$  and

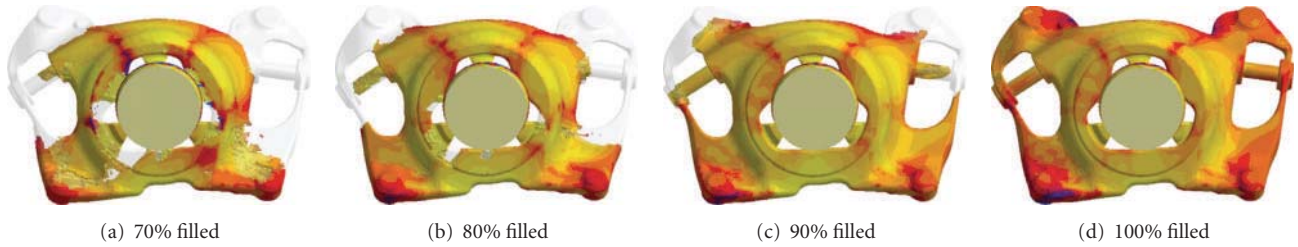


FIGURE 14: Filling behavior of module bracket by rheology forging.



FIGURE 15: Solidification behavior of module bracket by rheology forging.

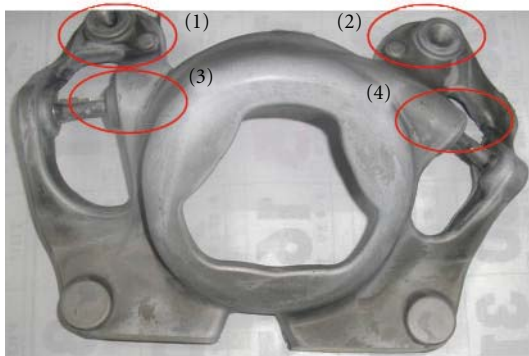


FIGURE 16: Fabricated module bracket and position of microstructure (initial slurry temperature: 600°C, punch velocity: 50 mm/sec and solid fraction: 70%).

eutectic phases were separated by the applied pressure at the mentioned positions. This liquid segregation was caused by nucleation of solid particles at the early solidification stage, which later grew to dendrite and rosette type structure by high liquid fraction. EMS is well affected between liquidus and solidus. Reduction of pouring slurry temperature could be done by the dendrite and liquid segregation. However, generally lower temperature requires more load in metal forming. In addition, unfilling and surface crack can easily take place. Therefore, the finding of optimal pouring temperature is very important.

**5. Fabrication of Knuckle Component by EMS Rheo-Casting**

5.1. *Mold Design and Simulation with MAGMASoft.* To produce a knuckle using EMS, an optimal knuckle mold was

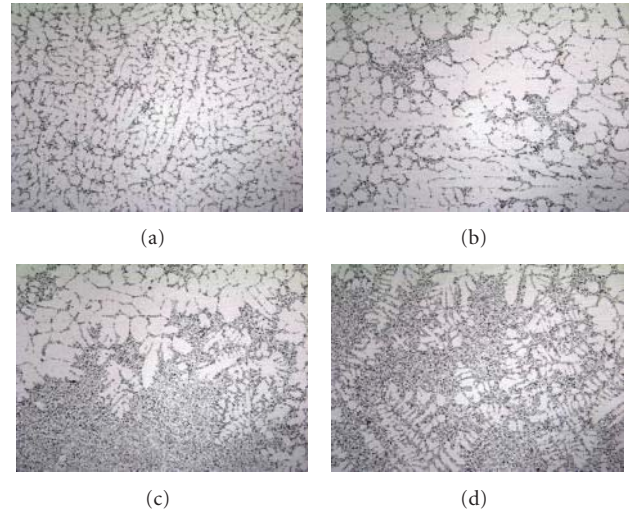


FIGURE 17: Microstructure of each position.

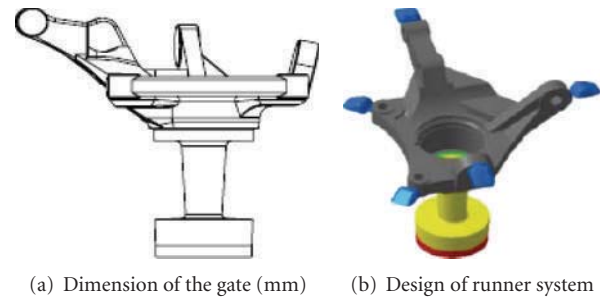


FIGURE 18: Geometry of gate and runner system for knuckle.

designed by using a computer program to predict product defects by analyzing filling and solidification. Figure 18 depicts the casting scheme of the knuckle describing the gate and the runner system. The sleeve and the gate were designed with a diameter of 80 mm and a height of 147.5 mm, respectively. The overflow was designed to eliminate the oxide layer on the surface of the slurry and gaseous impurities occurring during production.

The analyses of filling and solidification were performed using condition 1 (a speed of 0.6 m/s for the gate and of 0.2 m/s for the cavity) and condition 2 (a speed of 0.1 m/s for the gate and of 0.3 m/s for the cavity). Figure 19 shows the behavior of filling in the knuckle by injection speed for each condition. Figure 19(a) shows how the materials

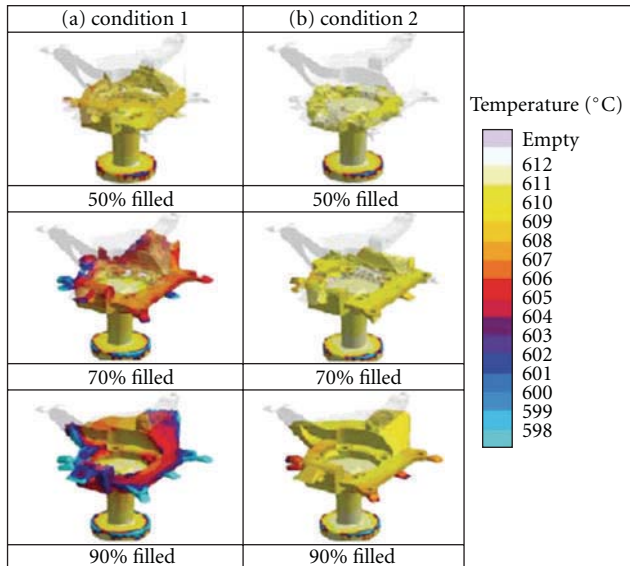


FIGURE 19: The comparison of filling behavior at conditions 1 and 2.

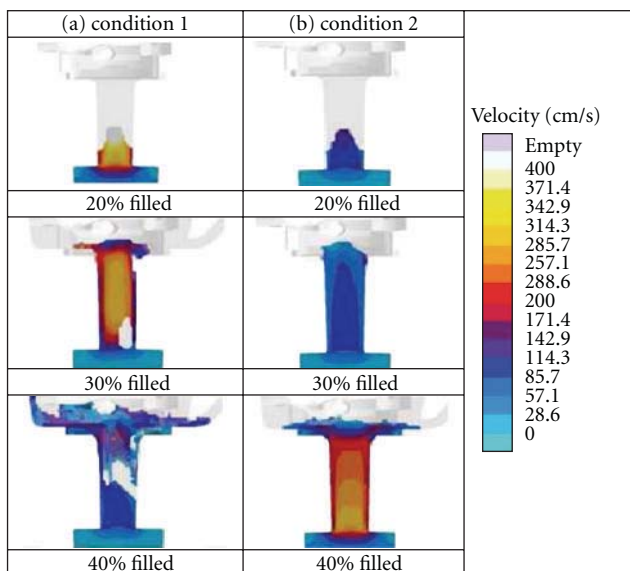


FIGURE 20: Comparison of velocity behavior at the runner.

spattered at the ingate when the cavity was filled to 50 and 60% using condition 1. The temperature in the mold was altered by 20°C under condition 1 because of the increase in filling time. In contrast to condition 1, the cavity was filled flawlessly around the gate and the product using condition 2 as shown in Figure 19(b). The deviation of temperature in the mold was found to be 7°C and the fraction of liquid phase was within 10%. Figure 20 compares the behaviors of the flows at the gate for each condition. When the gate speed was 0.2 m/s, the mold was insufficiently filled after 30% of the filling was poured due to the high speed of the injection when filling the mold up to 30%. It is evident that the turbulence of the flow spatters the material because after 40% of the filling

was poured, the product was insufficiently filled. Thus, these results indicate that porosity occurs due to the presence of gas impurities in the knuckle. In Figure 20(b) it is clear that the gate was fully filled and a laminar flow was well developed.

**5.2. Results of Knuckle Fabrication by Rheo-Casting.** Figure 21 shows a photograph of the knuckle produced without EMS with solid fraction of 40%. When the injection pressure was 450 bar and the injection speed was 0.2 m/s, the products were insufficiently formed due to solidification occurring in the sleeve while filling the cavity. Moreover, the surface quality was degraded because forming pressure did not transfer to surface of the product. Since low-speed casting resulted in an incomplete formation of the part and a poor surface quality, the injection speed was increased from 0.2 m/s to 0.3 m/s. When the injection pressure was 450 bar and the injection speed was 0.3 m/s, the resulting knuckle was sufficiently formed and its surface quality was excellent. When the injection speed was increased from 0.3 m/s to 0.5 m/s and the injection pressure was kept at 450 bar, large volume products were incompletely formed and had degraded surfaces.

To investigate the effect of EMS on the microstructures of products, the product was cast while varying electromagnetic current and time. Figure 22 shows photographs of the microstructure of the knuckle produced using EMS. The microstructure of the knuckle cast under each condition was investigated at the tip of the product, which can be difficult to form. When the stirring current was 60 A and stirring time was 5 s, the dendritic structure was crushed somewhat but not completely. When the current was 60 A and the time was 10 s, the structure was fine. The primary  $\alpha$ -Al phase particle size was 75  $\mu\text{m}$  and the roundness was 1.6. As the stirring time increased to 15 s with a 60 A stirring current, the crushed dendritic structure was recombined and coarsened. The primary  $\alpha$ -Al phase particle size was 79  $\mu\text{m}$  and the roundness was 1.7.

**5.3. Mechanical Properties and Defect Analysis.** Table 2 summarizes the mechanical properties of the knuckle formed with and without EMS by these conditions. To investigate the effect of EMS on the mechanical properties, the forming experiments were performed using stirring currents of 40 A and 60 A with stirring times of 5, 10 and 15 s. The mechanical properties of the products using EMS were considerably enhanced compared with those of the products formed without EMS, but the values themselves were low. As air and oxides flowed into the products when the melts were stirred or were poured into the mold cavity, those impurities may have caused deterioration in the mechanical properties. The microstructures of the knuckles produced using EMS had very fine primary phase particles compared with those of the products formed without using EMS. Globular particles may have influenced the mechanical properties [7].

To investigate the cause of the deterioration of the mechanical properties of the knuckle produced by EMS, the interior of the product was X-rayed (Toshiba Tosray-150 HS), as shown in Figure 23. The final filling part, which

TABLE 2: The mechanical properties of knuckle part with and without stirring according to each condition.

P (Mpa)	V (m/s)	C (A)	T <sub>s</sub> (s)	Heat treatment condition	Elongation (%)	UTS (MPa)
450	0.3	0	0	T5 (8 h at 170°C)	1.9	145
450	0.5	0	0	T5 (8 h at 170°C)	2.1	132
450	0.3	60	5	T5 (8 h at 170°C)	2.2	204
450	0.3	60	10	T5 (8 h at 170°C)	2.4	212
450	0.3	60	15	T5 (8 h at 170°C)	1.5	164
450	0.3	60	5	T6 (3 h at 530°C 8 h at 160°C)	3.5	264
450	0.3	60	10	T6 (3 h at 530°C 8 h at 160°C)	3.6	250
450	0.3	60	15	T6 (3 h at 530°C 8 h at 160°C)	2.9	230
450	0.3	60	15	T6 (3 h at 530°C 8 h at 160°C)	6.7	286

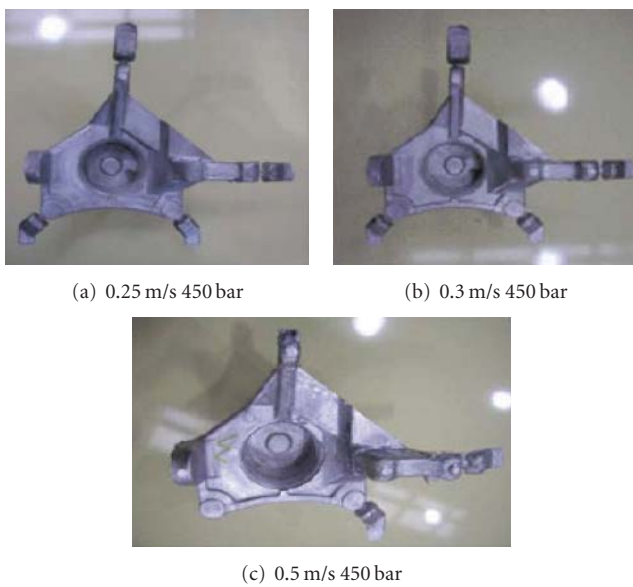


FIGURE 21: Photographs of the knuckle part fabricated by various casting conditions.

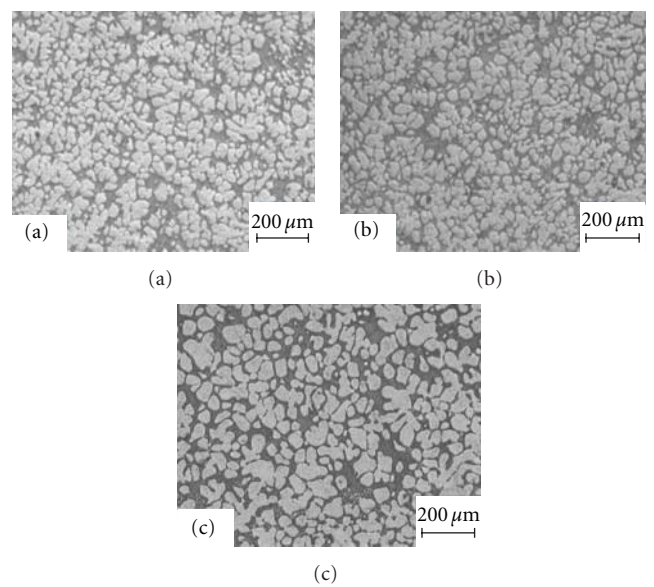


FIGURE 22: Microstructure of knuckle part at stirring current 60 A for (a) 5 s; (b) 10 s; (c) 15 s.

may have had defects, was the focus of the investigation. As can be seen from the photographs shown in Figure 23, numerous porosities were found inside the products that were cast after being stirred with 60 A of current for 15 s. The air flowing into the products and the turbulent flow of the melts caused the porosities to develop. Moreover, air in the mold cavity could not be vented through air vents, thus the air remains in the mold cavity. Figure 24 shows a photograph of the microstructure of the knuckle including porosity and impurities. Observations of the microstructures revealed that porosities existed inside the products. These porosities may diminish mechanical properties and cause surface defects as the pores vent air to the surface of the products during heat treatments. To eliminate these porosities, the stirring current should be increased slowly preventing air from flowing into the products and air in the mold cavity could be completely vented through the five overflows while the melts filled the mold cavity.

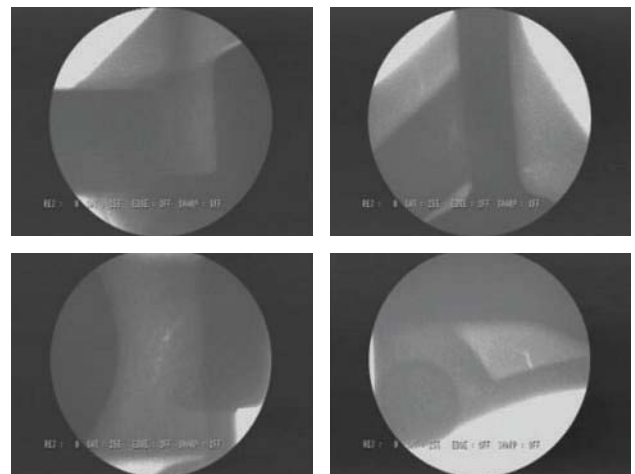


FIGURE 23: The X-ray photograph to observe inside knuckle.

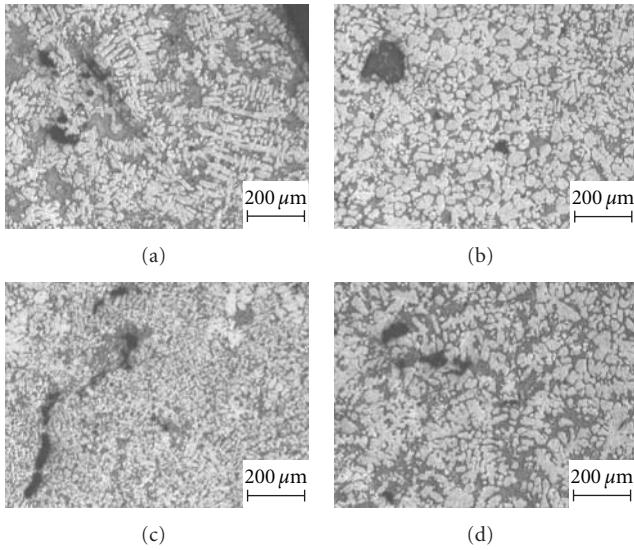


FIGURE 24: The microstructure of knuckle including defects such as porosity and segregation of liquid phase ( $C : 60 \text{ A}; T_s : 20 \text{ s}$ )

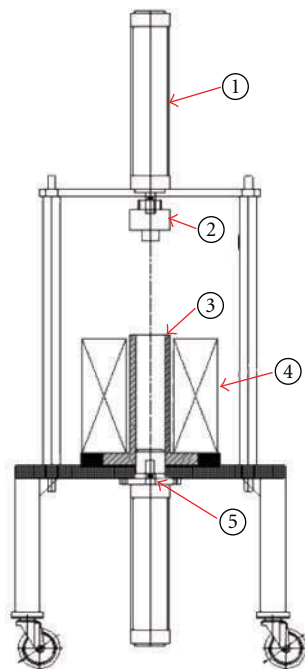


FIGURE 25: Schematic diagram of the vacuum casting system ((1) air cylinder, (2) Injection punch, (3) Sleeve, (4) Case, (5) Moving bottom punch).

## 6. Fabrication of Knuckle Component by EMS Two Type Rheo-Forging with Vacuum Pump

6.1. EMS under Vacuum for Rheological Billet Fabrication. To remove oxidization products and hydrogen gas from the molten metal, nitrogen gas was injected into the melt for 15 min. Oxidization products and impurities were thus cleared away from molten metal surface [8].

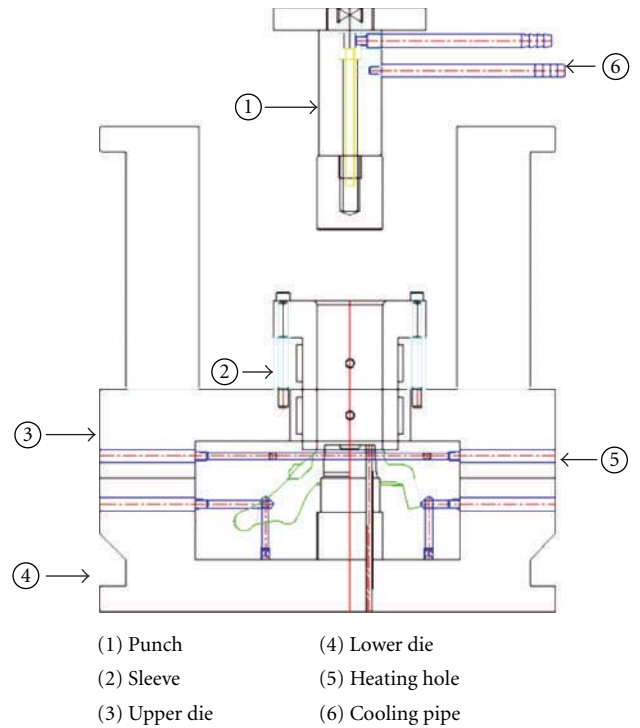


FIGURE 26: Schematic of indirect-type die set for rheo-forging and product.

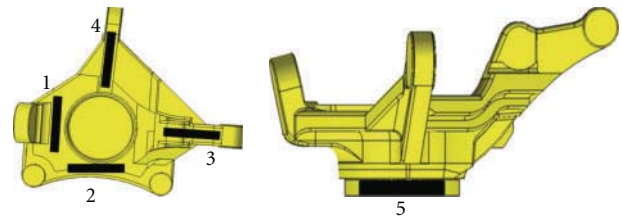


FIGURE 27: Positions of sample to observe in microstructure.

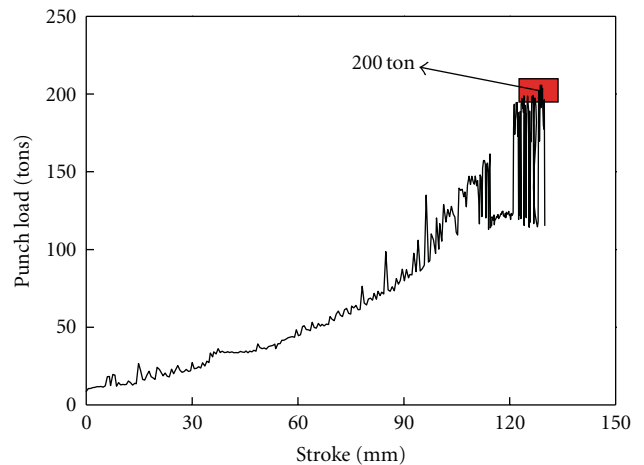


FIGURE 28: Stress of punch according to stroke for A356 at  $588^\circ\text{C}$  ( $S_f = 40\%$ ) in DEFORM-3D.

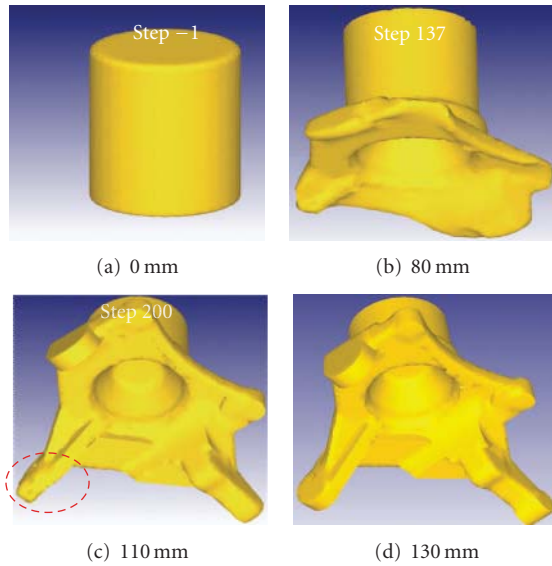


FIGURE 29: Shape change results according to punch stroke in DEFORM 3D.



FIGURE 30: Result of indirect rheo-forging test of rheological materials.

In aluminum alloys, hydrogen gas readily makes holes within the alloy during solidification. In addition, hydrogen gas has the highest solvency within aluminum alloy compared to other constituents of air, such as oxygen and nitrogen. Consequently, gas hole formation and porosity are increased within the alloy as the temperature decreases, degrading its mechanical properties.

Figure 25 shows schematic diagram of the EMS and vacuum pump. The EMS system operated with a three-phase current at 60 A. After the molten metal was poured, the injection punch was moved to the surface of the top

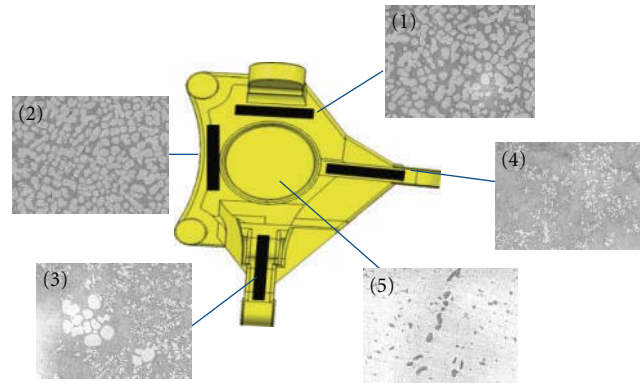


FIGURE 31: Microstructures of knuckle at each position ( $S_f = 40\%$ ,  $588^\circ\text{C}$ ).

sleeve and the EMS was operated under vacuum. This system prevents oxidation of the molten metal and air indraft.

6.2. *Die Design and Simulation with DEFORM 3D.* Knuckles were fabricated by a press machine. To decrease the process cycle time, the direct forging type is required, and Figure 26 shows the schematic of the indirect-type experimental procedure in the rheo-forging knuckle sample.

The temperature was controlled for achieving the solid fraction between 30% and 50%. Solid fraction (pouring temperature) is variable in rheo-forging. Figure 27 shows the positions on the test piece that were subjected to tensile testing. The regions of each position were also studied by microscope. In order to observe the differences of the mechanical properties at different locations on the test piece, microstructure observation was carried out.

Before the experiment was started for the required forging load was calculated by simulation, considering the capacity of the press machine, with a maximum 200 Tons. As shown in Figure 28, the required load was about 200 Tons at  $588^\circ\text{C}$  (40% solid fraction). Figure 29 shows the shape change with respect to the punch stroke. At the near end of punch displacement of about 110 mm, most of cavities were filled, except for marked region as shown Figure 29(c). When the punch displacement reached about 130 mm, all cavities were fully filled.

6.3. *Results of Knuckle Fabrication by Rheo-Forging.* Figure 30 shows the real samples fabricated with respect to various pouring temperatures. All samples were completely filled above the pouring temperature of  $588^\circ\text{C}$ . Real samples showed similar filling behavior as the simulation results in indirect forging.

In semisolid forming, liquid segregation easily occurred at high velocity due to the thixotropic characteristic. High shear rate resulted in decreased viscosity for a given solid fraction. Material having low solid fraction flowed easily compared with already hardened material. As a result, segregation occurred in a wide region. On the contrary, almost primary  $\alpha$  phase is shown Figure 31 at position 5. Position 5 region was directly contacted with the punch.

Material flow was slower than that of the other regions. The contacted region was rapidly cooled. As previously stated, a material hardened by the decreasing temperature flows less easily than materials in liquid state. The remaining liquid material is squeezed. It moves down to the other cavities. For this reason, liquid phase is rare at position 5.

## 7. Summary

The applied EMS fabrications of automobile components were studied by simulation and experiment. The following conclusions were obtained.

- (1) It was found from the microstructural observation that the fine and spheroidized primary  $\alpha$ -Al phase particles were obtained, as a result of products by EMS.
- (2) The analysis of filling products using MAGMAsoft (casting analysis software) or DEFORM 3D (forging analysis software) was conducted, and based on the analysis results, the optimized mold design scheme was constructed, predicting the defects that may take place during forming.
- (3) Porosity is removed by the forging pressure. However, the molten aluminum alloy easily takes up hydrogen gas during solidification under exposure to the atmospheric environment. Defects such as porosity and oxide in the material could be removed by application of a vacuum during EMS.
- (4) In the rheo-forging process, segregations was remarkably occurred at branches of the knuckle. It must be controlled to obtain uniform mechanical properties according to the changing process condition.
- (5) In rheo-forming process, the EMS could be easily applied during fabrication, and it is very effective method to increase the mechanical properties.

## Acknowledgments

This work was financially supported by the Ministry of Knowledge Economy (MKE) and Korea Institute for Advancement in Technology (KIAT) through the Workforce Development Program in Strategy Technology by the National Research Foundation of Korea (NRF) grant funded by the Korea government (MEST) (no. 2009-0081077), and by the National Core Research Center (NCRC). The authors would like to express their deep gratitude to the Ministry of Science & Technology (MOST) for its financial support.

## References

- [1] M. C. Flemings, "Behavior of metal alloys in the semisolid state," *Metallurgical Transactions A*, vol. 22, no. 5, pp. 957–981, 1991.
- [2] C. G. Kang, P. K. Seo, and Y. P. Jeon, "Thixo diecasting process for fabrication of thin-type component with wrought

- aluminum alloys and its formability limitation," *Journal of Materials Processing Technology*, vol. 160, no. 1, pp. 59–69, 2005.
- [3] A. Pola, R. Roberti, E. Bertoli, and D. Furloni, "Design and production of new aluminum thixotropic alloys for the manufacture of structural components by semisolid die casting," *Diffusion and Defect Data Part B*, vol. 116-117, pp. 58–63, 2006.
- [4] D. Liu, H. V. Atkinson, P. Kapranos, W. Jirattiticharoean, and H. Jones, "Microstructural evolution and tensile mechanical properties of thixoformed high performance aluminium alloys," *Materials Science and Engineering A*, vol. 361, no. 1-2, pp. 213–224, 2003.
- [5] K. Sukumaran, B. C. Pai, and M. Chakraborty, "The effect of isothermal mechanical stirring on an Al-Si alloy in the semisolid condition," *Materials Science and Engineering A*, vol. 369, no. 1-2, pp. 275–283, 2004.
- [6] C. G. Kang, P. K. Seo, and Y. I. Son, "The effect of velocity control method on the part characteristic in semi-solid die casting," *The Korean Society of Mechanical Engineers A*, vol. 10, pp. 2034–2043, 2002.
- [7] C. P. Hong and J. M. Kim, "Development of an advanced rheocasting process and its applications," *Diffusion and Defect Data Part B*, vol. 116-117, pp. 44–53, 2006.
- [8] S. Lee and B. J. Ye, "The variation of pore distribution behavior according to melt treatments for Al alloys," *The Korean Foundrymen's Society*, vol. 21, no. 6, pp. 343–349, 1999.

## Research Article

# Industrial Semi-Solid Rheocasting of Aluminum A356 Brake Calipers

**U. A. Curle, J. D. Wilkins, and G. Govender**

*Materials Science and Manufacturing, the Council for Scientific and Industrial Research, Meiring Naudé Road,  
P. O. Box 395, Brummeria Pretoria 0001, South Africa*

Correspondence should be addressed to U. A. Curle, [ucurle@csir.co.za](mailto:ucurle@csir.co.za)

Received 18 October 2010; Accepted 19 November 2010

Academic Editor: Shoujin Sun

Copyright © 2011 U. A. Curle et al. This is an open access article distributed under the Creative Commons Attribution License, which permits unrestricted use, distribution, and reproduction in any medium, provided the original work is properly cited.

Industrial semi-solid casting trials of aluminum A356 brake calipers were performed over five days with the CSIR-RCS and high-pressure die casting process cell. Consecutive visual passed castings were used as the measure of process stability, and common defects between trials were categorized. Short fill results are erratic and caused by unintended underdosing by the furnace or incomplete billet discharge at the delivery point in the shot sleeve. Cold shuts can be significantly reduced by adjusting the shot control profile. Surface finish defects include surface roughness and staining caused by lubricant burn off. Visual passed castings display none of the above-mentioned external defects. X-ray examination and pressure testing of heat-treated castings from the consecutive visual passed castings show improvement over the five days. These initial-stage industrialization efforts pave the way for process commercialization.

## 1. Introduction

Since the concept of semi-solid metal forming was discovered in the early 1970s, the full potential of the process has not yet been realized. The initial hype about the benefits of forming near net shape high-integrity components resulted in a wide array of technological approaches being proposed [1]. Up to the early 2000s, the preferred approach was using the thixocasting method which requires reheating a billet with the desired globular microstructure to the semi-solid state and forming. The high cost of infrastructure and the actual processing of the material have limited the use of the process although this method has a great opportunity to produce high-quality components [2], especially in cost-sensitive markets like the automotive industry.

In order to make semi-solid metal (SSM) forming a viable option, the “slurry on demand” or rheocasting processes offer a more cost-effective method of preparing slurries for SSM forming. It was proposed [2] that the ideal process for SSM forming is a cell with an integrated slurry maker; the slurry maker needs to be efficient and capable of producing the desired microstructure and billet consistency

with accurate process control. During the early 2000s, a myriad of rheocasting systems were developed, UBE (NRC—New Rheocasting), Honda (rheocasting), IDRA (SSR), THT presses, SOD (Slurry on demand), Mercury Marine, and New Rheo-Diecasting (Brunel University) to name a few [3]. Although rheocasting processes do provide a cost advantage over the thixocasting process, they have not been widely adopted by industry because the process is more expensive than conventional casting processes. Also, the consistency, efficiency, and repeatability of the processes need to be demonstrated with a high degree of confidence.

The Council for Scientific and Industrial Research in South Africa has developed and patented a rheocasting system (CSIR-RCS) [4, 5] in the early 2000s. Since then, testing was performed on a small-scale cell with different alloys including Al-7Si-Mg [6] and Al-Cu-Mg-(Ag) [7] casting alloys; heat treatable Al-Cu-Mg, Al-Mg-Si, and Al-Zn-Mg-Cu wrought alloys [8], SiC<sub>p</sub> aluminum metal matrix composites [9] as well as high purity aluminum [10].

An industrial scale semi-solid metal high-pressure die casting cell with the CSIR-RCS unit at the heart was established in 2008/09. Although there was interest from

potential industry partners, the key question continuously asked was: how stable and repeatable is the process? This paper will present the first phase of the work performed to demonstrate the industrial feasibility of the CSIR-RCS through casting and industrial quality testing of aluminum A356 brake calipers in order to answer these questions.

## 2. Experimental

Aluminum A356 brake calipers were produced on five different days, each a single continuous run, with the CSIR-RCS and a high-pressure die casting (HPDC) machine. Figure 1 shows the brake caliper casting in drawing (including the runner and the biscuit) and the actual premachined component. The overall dimensions for the casting in Figure 1(a) is 327 mm high  $\times$  163 mm wide  $\times$  95 mm thick; the biscuit and gate diameters are 78 mm and 35 mm, respectively.

Figure 2 gives the layout of the CSIR-RCS-HPDC cell. The main components that make up the cell are: a 240 kg dosing furnace (WESTOFEN WESTOMAT W25S), an automated robotic arm (FANUC ROBOT M-16iA), a three-coil version of the CSIR-RCS (induction stirring with simultaneous forced air cooling [4]) processing unit, and a 630 ton HPDC machine with full shot control (LK DCC630). The mechanical hardware operation of the cell runs automatically through computer control software (NATIONAL INSTRUMENTS LABVIEW 8.6).

The 240 kg dosing furnace was filled by melting commercial aluminum alloy A356 ingots in charges of approximately 40 kg each with a custom-made induction heating ladle furnace. The metal temperature in the dosing furnace was left to equilibrate after the last charge (with additional Sr) was added. A sample was poured into a cup and chilled for chemical analysis by optical emission spectroscopy (Thermo Quantis OES). The composition of the aluminum alloy A356 melt was found to be 7.14 wt% Si, 0.36 wt% Mg, 0.14 wt% Fe, 0.13 wt% Ti, and 105 ppm Sr with the balance of Al.

Thermodynamic properties of the alloy were then calculated with an aluminum thermodynamic database (ProCast 2009.1) from the specific OES composition. Table 1 summarizes the calculated thermodynamic properties and deduced rheocasting parameters. A pouring temperature of approximately 40°C above the liquidus (the pouring temperature sensitivity has not yet been established) and a semi-solid metal (SSM) processing temperature corresponding to a solid fraction of 26% are used from experience with this specific SSM processing cell system.

The sequence for casting was as follows: liquid metal was poured from the dosing furnace into a stainless steel processing cup (approximately 2 kg) which was then robotically transferred to the CSIR-RCS unit and entered the coil train at the bottom. All three coils in the processing unit was inductive while forced air cooling was only used (manually activated) on the top coil to control the SSM temperature which was measured with a thermocouple in the semi-solid metal contained in the cup.



(a)



(b)

FIGURE 1: Example of the rheocast aluminum brake caliper including the runner and the biscuit in part drawing (a) and the actual premachined component (b).

When this cup at the top of the train thus been processed after reaching the SSM temperature, it was robotically transferred to the shot sleeve of the HPDC machine, and the injection shot was triggered automatically to fill the die. The die temperature was controlled by two oil heaters (REGLOPLAS 300 L), one for each half of die, and was set at 170°C.

The piston followed a set computer-controlled injection velocity profile which was adjusted at the beginning of each day to achieve the best filling result (within the first 4

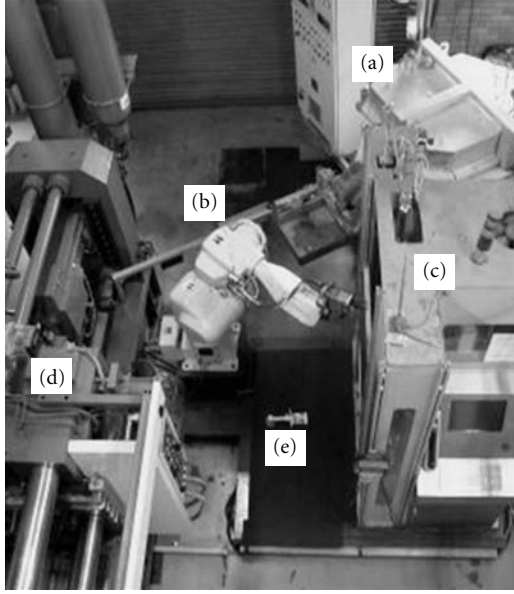


FIGURE 2: The CSIR-RCS-HPDC cell arrangement: automatic dosing furnace with controller (a), automated robotic arm (b), the CSIR-RCS processing unit (c), shot end of the 630 ton HPDC machine (d), and a brake caliper casting for scale (e).

castings) and was kept constant during the remainder of that day's particular run. These minor adjustments to the injection profile were to maintain repeatability. The casting was ejected after solidification and manually removed.

Each casting of a trial was visually examined for cold shuts, short fills, and surface finish. A visual pass was made on grounds of fulfilling the following three criteria: there were no externally visible cold shuts; the component filled properly which included the overflow and a proper biscuit thickness; lastly if the surface finish was macroscopically smooth.

Four visual pass castings were randomly selected from each day's trial. These twenty castings were solution heat treated at 540°C for 1 hour and quenched in water to accentuate porosity before independent X-ray examination. An X-ray examination pass was awarded after a standard combination of nine different positions was inspected in the casting and was found fit to continue to the machining section.

Two other castings were randomly selected from the visual passed castings and heat treated to peak strength (solution heat treated at 540°C for 1 hour and artificial ageing at 180°C for 4 hours [6]) for pressure leak rate tests after full machining. These final machined brake calipers were assembled into a pressure test system where leak rates are measured at both 2 bar and 140 bar.

### 3. Results and Discussion

Aluminum A356 brake caliper casting trials were successfully completed with a trial per day. A breakdown of casting trial results is given in Table 2. Castings produced per day ranged

TABLE 1: Calculated thermodynamic and deduced rheocasting parameters of A356 for the three-coil CSIR-RCS-HPDC cell.

Parameter	Property	Temperature/°C
Thermodynamic	Liquidus	610
	Solidus	548
Rheocasting	Pouring	645
	SSM	590

TABLE 2: Results of the aluminum A356 brake caliper casting runs on different days with the CSIR-RCS and HPDC.

Trial/day	A	B	C	D	E
	/castings				
Castings produced	23	18	31	25	31
Consecutive visual pass	5	8	12	13	13
	Occurrence/%				
Short fills	0	27	3	24	16
Cold shuts	26	6	3	0	16
Surface finish defects	0	0	10	4	6
Total visual pass	74	67	84	72	62

between 18 and 31 castings. The aim was to produce between 25 and 30 castings per day so that comparisons are more meaningful.

The number of consecutive castings that passed the visual test, in any particular trial, was taken as the measure of improvement and an indication of process repeatability. Table 2 shows that there was indeed an improvement over the five days where the last trial produced nearly three times as many consecutive castings that passed the visual examination compared to the first trial. The total visual pass rate as a measure of repeatability is subjective because it is not related to chronological castings in the process.

Common defect classes were identified for reject castings and are shown in Table 2. Short fill defects are related to irregular billet mass delivery to the shot sleeve and cold shut defects are related to the injection piston velocity profile. Surface finish defects with this specific die are related to lubricant, applied intermittently to the sliding core, spilling into the die cavity. The total number of castings that passed the visual evaluation completes the balance.

There is no real trend evident from the short fill rate results, Table 2, between the different days; the cause is intermittent. Short fills such as those in Figure 3 are normally associated with too little material entering the die. In the current casting cell system, this can happen, although not distinguished between in the Table 2, either by an unintended gross underdosing mass from the dosing furnace or by billet material remaining in the cup after billet delivery to the shot sleeve.

Figure 4 shows typical cold shuts which are associated with inadequate joining of the separate metal flow fronts during filling. The rate of cold shuts in Table 2 started off at 26% in Trial A and decreased to 0% by Trial D, this was achieved by manually adjusting the injection piston velocity profile mainly for the minor change in day-to-day mass

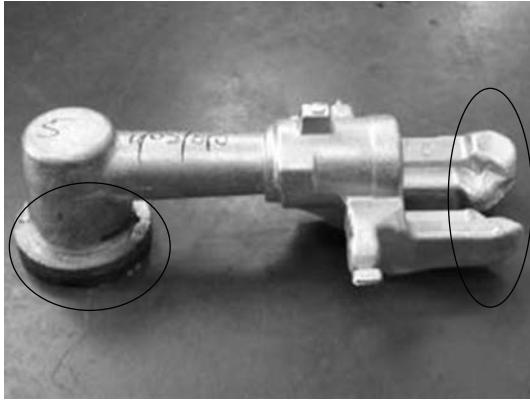


FIGURE 3: An example of a short fill defect brake caliper casting produced during trials with the CSIR-RCS-HPDC cell indicating a thin biscuit in conjunction with an incomplete casting.



FIGURE 4: An example of a cold shut defect brake caliper casting produced during trials with the CSIR-RCS-HPDC cell.

of the billet delivered into the shot sleeve. The cold shut rate increased on the last day because a position value in the velocity profile was initially adjusted towards the wrong direction which exacerbated this defect rate.

Surface finish defects manifest by increased surface roughness due to volatilization of the oily compounds and staining by resulting soot as shown in Figure 5. Surface finish defect rates in Table 2 seem to have suddenly increased from 0% during Trial A and Trial B to in the order of 10% during subsequent trials. This kind of defects goes unnoticed when gross defects like short fills and cold shuts persist.

Visual passed castings in Table 2 all underwent a critical external examination. All these castings properly filled the die cavity into the overflows, and no external cold shuts were perceptible. All castings surfaces were examined and passed if found to be smooth with a bright luster. Figure 6 shows a casting that passed all the visual examinations.

Industrial quality pass rate results of X-ray and pressure tests are given in Table 3 for consecutive visual passed castings produced as the measure of quality that underscribes the stability and repeatability of the CSIR-RCS-HPDC process cell. Other castings were also X-rayed and pressure tested but



FIGURE 5: An example of the rough surface finish of a lubricant defect brake caliper casting produced during trials with the CSIR-RCS-HPDC cell.

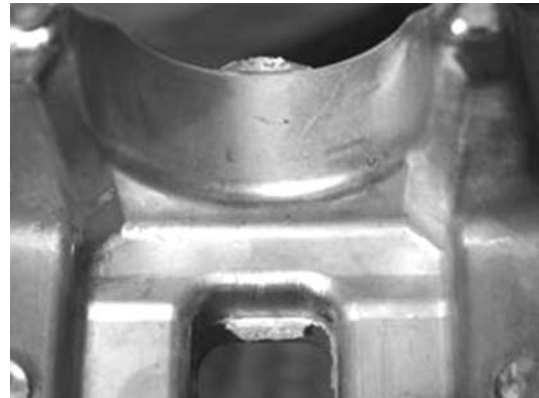


FIGURE 6: An example of a visually inspected and passed brake caliper casting produced during trials with the CSIR-RCS-HPDC cell without any external defects.

bears no meaningful relation to the stability of the process following the argument on the number of consecutive visual passed castings. The total number of castings tested differs between days because the samples for X-ray and pressure tests were initially random chosen from the total visual passed castings and afterwards again combined with the consecutive visually passed casting results.

X-ray tests were done at a local manufacturer that currently makes this brake caliper by another casting process which is set up to do extensive automated positioning evaluations in-house. The question of pass or fail was posed to the manufacturer by deciding if the casting would pass for subsequent machining as if it was one of their own castings, without explanations. This approach was followed to ensure

TABLE 3: X-ray and pressure test quality control sample of consecutive visually passed castings achieved on the different days with the CSIR-RCS and HPDC. X-rayed brake calipers were solution heat-treated at 540°C for 1 hour and quenched. Pressure tested brake calipers were peak aged by solution heat treatment at 540°C for 1 hour, quenched and artificially aged at 180°C for 4 hours.

Trial/day	A	B	C	D	E
	/castings				
X-rayed test	2	2	2	3	3
Pressure test					1
Total tested	2	2	2	3	4
Pass X-ray test	1	1	2	2	3
Pass pressure test					1
Total passed	1	1	2	2	4
Sample pass rate/%	50	50	100	67	100

TABLE 4: Stability and quality summary table for brake caliper casting trials over five days with the CSIR-RCS-HPDC process cell.

Trial/day	A	B	C	D	E
Consecutive visually passed/castings	5	8	12	13	13
Quality pass rate/%	50	50	100	67	100

a higher degree of impartiality. Again it is clear from the sample pass rate in Table 3 that improvement was made over time.

Table 4 gives the summary of the success achieved with the CSIR-RCS-HPDC process cell in these early stages of industrial trials with this rheocasting process en-route to commercialization efforts. Extensive heat treatment optimization and tensile property testing have been addressed for these aluminum A356 brake calipers which show the tensile properties to be 261 MPa yield strength, 317 MPa ultimate tensile strength, and 6.7% elongation [11].

#### 4. Conclusions

Industrial semi-solid casting trials of aluminum A356 brake calipers were successfully completed on five different days with a CSIR-RCS-HPDC process cell where consecutive visually passed castings was used as a measure of process stability because of a chronological time relationship. Common defects between trials were categorized. Short fills, which are erratic and caused by underdosing of metal into the cup or incomplete discharge at the delivery point in the shot sleeve resulting in incomplete filling of the die cavity. Cold shuts are metal flow-related problems, and their occurrence can significantly be reduced by adjusting the injection piston velocity profile during the start of a trial. Surface finish defects are related to the mechanics of this specific die and can be solved with a better die design. None of the defects are reprocessing related but are ancillary equipment related.

Visually passed castings display none of these classified external defects while X-ray examination and pressure testing of heat-treated castings from consecutive visual passed

castings show improvement over the five day trial ending in a 100% quality sample pass rate.

These early successful efforts of industrial trials pave the way for commercialization of the CSIR-RCS.

#### References

- [1] D. B. Spencer, R. Mehrabian, and M. C. Flemings, "Rheological behavior of Sn-15 pct Pb in the crystallization range," *Metallurgical Transactions*, vol. 3, no. 7, pp. 1925–1932, 1972.
- [2] Z. Fan, "Semisolid metal processing," *International Materials Reviews*, vol. 47, no. 2, pp. 49–86, 2002.
- [3] P. Kapranos, "Semi-solid metal processing—a process looking for a market," *Diffusion and Defect Data Part B*, vol. 141–143, pp. 1–8, 2008.
- [4] R. Bruwer, J. D. Wilkins, L. H. Ivanchev, P. Rossouw, and O. F. R. A. Damm, "Method of and apparatus for processing of semi-solid metal alloys," US7368690, 2008.
- [5] L. Ivanchev, D. Wilkins, and G. Govender, "Method and apparatus for rheo-processing of semi-solid metal alloys," in *Proceedings of the 8th International Conference on Semi-Solid Processing of Alloys and Composites (S2P '04)*, pp. 595–601, Limassol, Cyprus, 2004, Paper 15-2.
- [6] H. Möller, G. Govender, W. E. Stumpf, and P. C. Pistorius, "Comparison of heat treatment response of semisolid metal processed alloys A356 and F357," *International Journal of Cast Metals Research*, vol. 23, no. 1, pp. 37–43, 2010.
- [7] E. P. Masuku, H. Möller, R. Knutsen, L. Ivanchev, and G. Govender, "Optimisation of the solution heat treatment of rheo-processed Al-Cu-Mg-(Ag) alloys A206 and A201," *Materials Science Forum*, vol. 618, pp. 353–356, 2009.
- [8] U. A. Curle, "Semi-solid near-net shape rheocasting of heat treatable wrought aluminum alloys," *Transactions of Nonferrous Metals Society of China (English Edition)*, vol. 20, no. 9, pp. 1719–1724, 2010.
- [9] U. A. Curle and L. Ivanchev, "Wear of semi-solid rheocast SiC<sub>p</sub>/Al metal matrix composites," *Transactions of Nonferrous Metals Society of China (English Edition)*, vol. 20, supplement 3, pp. s852–s856, 2010.
- [10] U. A. Curle, H. Mölle, and J. D. Wilkins, "Shape rheo-casting of high-purity aluminium," *Scripta Materialia*. In press.
- [11] H. Möller, G. Govender, and W. E. Stumpf, "Application of shortened heat treatment cycles on A356 automotive brake calipers with respective globular and dendritic microstructures," *Transactions of Nonferrous Metals Society of China (English Edition)*, vol. 20, no. 9, pp. 1780–1785, 2010.

## Research Article

# The Influence of Prior Natural Aging on the Subsequent Artificial Aging Response of Aluminium Alloy A356 with Respective Globular and Dendritic Microstructures

Heinrich Möller,<sup>1</sup> Gonasagren Govender,<sup>1</sup> Pierre Rossouw,<sup>1</sup> and Waldo Stumpf<sup>2</sup>

<sup>1</sup>Materials Science and Manufacturing, CSIR, Pretoria 0001, South Africa

<sup>2</sup>Department of Materials Science and Metallurgical Engineering, University of Pretoria, Pretoria 0002, South Africa

Correspondence should be addressed to Heinrich Möller, hmoller@csir.co.za

Received 1 September 2010; Accepted 14 November 2010

Academic Editor: J. Dutta Majumdar

Copyright © 2011 Heinrich Möller et al. This is an open access article distributed under the Creative Commons Attribution License, which permits unrestricted use, distribution, and reproduction in any medium, provided the original work is properly cited.

Alloy A356 is one of the most popular alloys used for semisolid metal forming. The heat treatment cycles that are currently applied to semisolid processed components are mostly those that are in use for dendritic casting alloys. The assumption has been made that these heat treatments are not necessarily the optimum treatments, as the difference in solidification history and microstructure of SSM processed components should be considered. The objective of this study is to determine whether dendritic A356 behaves in a similar way to globular A356 in terms of its response to artificial aging with or without prior natural aging. The results indicate that the differences in microstructures (globular or dendritic) do not have a noteworthy effect on the heat treatment response. It is also shown that strong linear correlations are found between T4 and T6 hardness and wt% Mg of A356, regardless of the casting technique used.

## 1. Introduction

Semisolid metal (SSM) processing is a unique manufacturing technique to fabricate near-net shape products for a variety of industrial applications [1]. The objective is to achieve a semisolid structure which is free of dendrites and with the solid present in a near spherical form. This semisolid mixture flows homogeneously, behaving as a thixotropic fluid with viscosity depending on the shear rate and fraction of solid [2]. There are two different SSM processing methods, namely thixocasting and rheocasting. With thixocasting, a specially prepared billet of solid material with a globular microstructure is reheated into the semisolid range, followed by a forming process such as high pressure die casting (HPDC). Rheocasting on the other hand involves preparation of an SSM slurry directly from the liquid, followed by HPDC. Rheocasting has become the preferred semisolid process due to the higher costs of thixocasting [3]. The laminar flow during SSM processing during the die-fill avoids the problems of oxide and gas entrapment and also reduces

the shrinkage problems during solidification [4]. Blistering during heat treatment can therefore be prevented.

Large quantities of castings are made annually from aluminium alloy A356 (also known as Al-7Si-0.3Mg). This alloy is one of the most popular alloys used for semisolid metal forming due to its good “castability” [5]. The chemical composition limits of this alloy are shown in Table 1 [6]. The heat treatment cycles that are currently applied to semisolid processed components are mostly those that are in use for dendritic casting alloys [7, 8]. The assumption is that these heat treatments are not necessarily the optimum treatments, as the difference in solidification history and microstructure of SSM processed components should be considered [7–11]. However, a recent paper by the authors has shown that the heat treatment response and tensile mechanical properties of A356 automotive brake calipers are in fact not influenced by having a globular or dendritic microstructure [12]. The same conclusion was also reached by Birol [13, 14].

In addition, the authors have shown before that natural aging (room temperature aging after the solution treatment

and quench) prior to artificial aging has an adverse influence on the subsequent artificial aging response of SSM-HPDC A356 [9, 10]. An artificial aging treatment at 180°C for 4 h can, however, negate the effects of any prior natural aging [10]. A recent review paper [15] on the heat treatment of Al-Si-Cu-Mg alloys (which included alloy A356) has concluded that the influence of natural aging on subsequent artificial aging needs to be studied further in these alloys. Finally, it has also been shown previously by the authors [9, 11] that strong correlations exist between strength and Mg-content of SSM-HPDC A356 (with other element contents kept constant). The objective of this study is to determine whether dendritic A356 behaves in a similar way to globular A356 in terms of its response to artificial aging with or without prior natural aging. Also, the influence of microstructure on the maximum hardness in the T4 and T6 temper conditions is compared that can be achieved with A356 cast using different techniques (with similar Mg contents).

## 2. Experimental

Semisolid metal (SSM) slurries of alloy A356 (chemical composition, as well as the chemical composition limits for the alloy are given in Table 1) were prepared using the Council for Scientific and Industrial Research (CSIR) rheocasting process [16]. Automotive brake calipers were cast in steel moulds with an LK DCC630 HPDC machine, resulting in a globular microstructure. For comparison, automotive brake calipers of similar composition and exact design (shape, size, mass) were cast by a local manufacturer using gravity die casting (GDC), resulting in a dendritic microstructure (see [12, 17] for more details of the casting parameters, size, heat treatments, and tensile mechanical properties of these brake calipers).

In addition, rectangular plates ( $95 \times 30 \times 4 \text{ mm}^3$ ) with composition given in Table 1 were cast using investment casting (IC) to obtain a coarser dendritic microstructure than achieved in the brake caliper cast using GDC. Wax pattern assemblies consisted of 6 of the plates assembled with 3 plates per opposite side, spaced 40 mm apart. A vertical  $25 \text{ mm} \times 20 \text{ mm}$  rectangular runner bar was used (250 mm long) as shown in Figure 1. The plates were assembled at an angle of 75 degrees inclined to the runner bar. The runner bar extended below the lowest plates tip to form a dross trap. A pouring cup was attached to the top of the runner bar. The wax used was Remet 289B green wax. The preferred bottom pouring method for aluminium was not used to simplify the assembly and to ensure symmetry in the mould. Wax assemblies were prepared by washing with Pattern Wash 6 from Remet and rinsed with de-ionised water. The wax assemblies were left for 24 hrs to dry and to stabilise at the dipping room temperature of 21°C. The primary slurry consisted of Ransom & Randolph Primecote, colloidal silica 30% binder and Zircon flour (Zircon silicate) –325 mesh as refractory filler. The secondary slurry consisted of Ransom and Randolph Customcote colloidal silica 25% binder with fused silica (–325 mesh) as the refractory filler. The face coat stucco used was Zircon sand P109 (mean  $109 \mu\text{m}$ ) and



FIGURE 1: Wax pattern assembly used for IC of alloy A356.

the back-up coat stucco was Chamotte (Alumino silicate). The shell making facility was temperature controlled to  $21^\circ\text{C} \pm 1^\circ\text{C}$  and the humidity was monitored—the relative humidity was measured as  $\pm 60\%$ . The dipping procedure is given in Table 2.

Dewaxing (wax removal) was performed using a standard LBBC steam boilerclave with  $200^\circ\text{C}$  steam at 8 bar pressure for 15 min. The moulds were pre-fired in a gas fired furnace with a 5% oxidising atmosphere to a temperature of  $800^\circ\text{C}$ , kept for 2 hrs, and furnace cooled. The mould was inspected and vacuumed to ensure that the mould was clean and preheated to the required casting temperature and soaked for 1 hr in an electric kiln furnace. The metal and mould temperature during casting was  $720^\circ\text{C}$  to ensure a relatively coarse microstructure. Aluminium alloy A356, from the same master melt as was used for the SSM-HPDC plates, was melted in a SiC crucible in an electric furnace. Melting was timed to reach  $720^\circ\text{C}$  as the mould reached the 1 hr soaking time. This was to reduce metal time at temperature to reduce hydrogen pick-up as no de-gassing was done due to the small volume of the melt. The mould and metal were removed from the furnace at the same time. The mould was suspended in still air on a mould stand and the metal surface was skimmed to remove dross and slowly poured into the mould. The mould was left to cool to room temperature and mould removal was done by hand.

Solution heat treatment of all castings was performed at  $540^\circ\text{C}$  for 1 hour, followed by a water quench ( $20^\circ\text{C}$ ) (see [7, 9–12] that shows that 1 hour at  $540^\circ\text{C}$  is sufficient for alloy A356). The time necessary to place magnesium in solid solution by dissolution of the  $\text{Mg}_2\text{Si}$  in the alloy is rapid at  $540^\circ\text{C}$ . It has been suggested that it takes less than 5 minutes in alloy A356 [18]. Homogenisation occurs in approximately 8–15 minutes at  $540^\circ\text{C}$ . The samples were then naturally aged (NA) for either zero hours (artificial aging only) or 120 h (stable T4 temper), before being artificially aged at  $180^\circ\text{C}$  to determine artificial aging curves. Vickers hardness

TABLE 1: Chemical composition limits for alloy A356 [6], as well as the compositions of the alloys used in this study.

	Si	Mg	Fe	Cu	Mn	Zn	Ti	Other (Each)	Other (Total)
Min	6.5	0.25	—	—	—	—	—	—	—
Max	7.5	0.45	0.2	0.2	0.1	0.1	0.2	0.05	0.15
SSM-HPDC	7.0	0.35	0.14	0.01	0.01	0.01	0.14	Sr = 0.020	
GDC	6.6	0.36	0.27	0.03	0.01	0.02	0.06	Sr = 0.024	
IC	6.7	0.25	0.10	0.01	0.01	0.01	0.06	Sr = 0.026	

TABLE 2: The dipping procedure for investment casting of alloy A356.

Coate no.	Slurry	Stucco	Drying time	Drying method
Primary 1	Zircon Primary	Zircon Sand	8 hours	Air dry
Primary 2	Zircon Primary	Zircon Sand	8 hours	Air dry
Secondary 1	Customcote	Chamotte 0.25–0.7 mm	45 Min	Fan
Secondary 2	Customcote	Chamotte 0.25–0.7 mm	45 Min	Fan
Back-up 1	Customcote	Chamotte 0.7–1.2 mm	45 Min	Fan
Back-up 2	Customcote	Chamotte 0.7–1.2 mm	45 Min	Fan
Back-up 3	Customcote	Chamotte 0.7–1.2 mm	45 Min	Fan
Back-up 4	Customcote	Chamotte 0.7–1.2 mm	45 Min	Fan
Seal coate	Customcote	—	24 Hours	Air

numbers (VHN) were determined (using a 10 kg load) from the average of at least four readings per sample. The average hardness values were found to be reproducible within  $\pm 3$  VHN for all heat treatment conditions tested.

### 3. Results and Discussion

The globular microstructure produced with SSM-HPDC is shown in Figure 2(a). In contrast, the dendritic microstructures obtained with GDC and IC are shown in Figures 2(b) and 2(c). Modification of the eutectic from a plate-like to a fine fibrous silicon structure has been achieved by the addition of strontium (Table 1) [19]. It is evident from Figure 2 that GDC produced a finer microstructure than SSM-HPDC and IC. Image analysis revealed a secondary dendrite arm spacing (SDAS) of approximately  $20 \mu\text{m}$  in the GDC calipers, whereas the SDAS of the IC plates was  $32 \mu\text{m}$ . The average globule size in CSIR SSM-HPDC calipers was approximately  $60 \mu\text{m}$ .

Solution treatment at  $540^\circ\text{C}$  for 1 h results in the spheroidisation of the eutectic silicon particles in all the A356 castings (Figure 3).

Figure 4 shows artificial aging curves that were determined for alloy A356 after solution treatment at  $540^\circ\text{C}$  for 1 hour, water quenching, and no natural aging. The artificial aging response is very rapid when no natural aging is applied whether the microstructure is globular or dendritic [9, 10]. Note that the hardness values are significantly lower for the IC plates than for the brake calipers. This is due to the low Mg-content of the IC plates (Table 1), resulting in a lower volume fraction of strengthening precipitates during artificial aging [9, 11, 20]. Artificial aging curves were also determined for alloy A356 after solution treatment at  $540^\circ\text{C}$  for 1 hour, water quenching and 120 hours natural aging (Figure 5) followed by artificial aging. The artificial aging

response is slow when prior natural aging has occurred, regardless of the microstructure of the A356. This slow artificial aging response can be explained by two different mechanisms. Firstly, it has been shown that the precipitates which grow during artificial aging from the clusters (formed during natural aging) are coarser than those that develop in certain 6000 series alloys aged immediately after quenching [21]. This results in a reduction of up to 10% in tensile properties for certain alloys. Secondly, it has been shown that natural aging following the solution treatment reduced the age hardenability of Al-Mg-Si wrought alloy AA6016 [22]. This was ascribed to solute clustering during natural aging, and the dissolution of these clusters during subsequent artificial aging. The extent of the loss was recovered by precipitation of  $\beta''$  particles upon further aging [22]. Taking into account Figures 4 and 5, it is seen that for alloy A356, the hardness values of naturally aged samples are also recovered with further artificial aging. The mechanism of the formation of coarser precipitates that leads to a decrease in tensile properties [21] does not allow for a full recovery in hardness. It is therefore concluded that reversion of the solute clusters is also responsible for the initial slow artificial aging response in naturally aged alloy A356 [9–11].

When no natural aging occurs, a plateau (between  $\sim 1$ –5 h) is maintained once the maximum hardness is reached during artificial aging (Figure 4), whereas a hardness peak is observed after approximately 4 hours when prior natural aging occurs (Figure 5) (also see [10]). The significant conclusion is that the influence of any natural aging prior to artificial aging can be removed by a 4-hours  $180^\circ\text{C}$  artificial aging treatment in both dendritic and globular A356.

Figure 6 compares the hardness values of A356-T6 ( $540^\circ\text{C}$ -1 h, 0 or 120 h NA,  $180^\circ\text{C}$ -4 h) as a function of the Mg-content of the castings (between the upper and lower limits of the specification—Table 1). Figure 6 includes

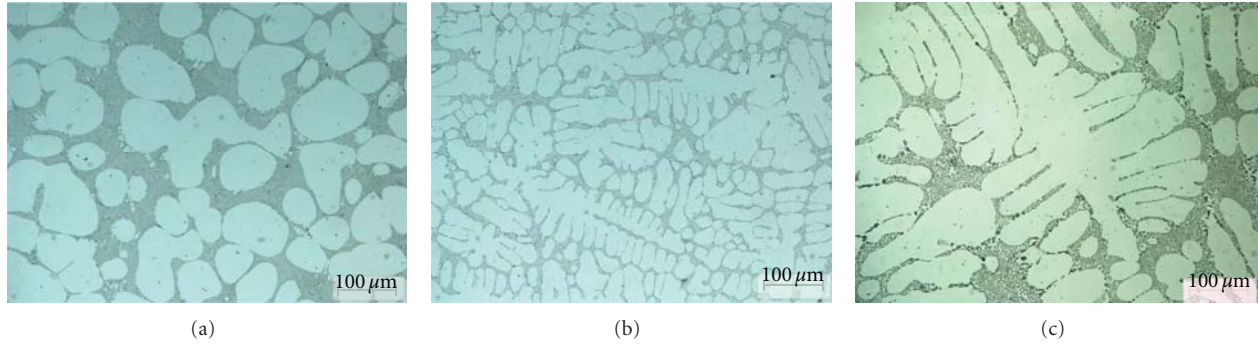


FIGURE 2: Optical micrographs of A356 in the as-cast condition produced by (a) SSM-HPDC, (b) GDC, and (c) IC.

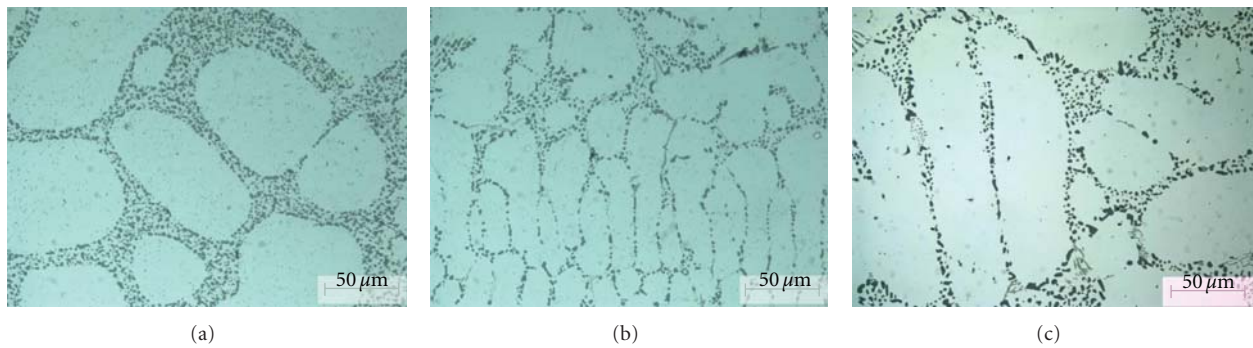


FIGURE 3: Optical micrographs of A356 in the T6 condition produced by (a) SSM-HPDC, (b) GDC, and (c) IC.

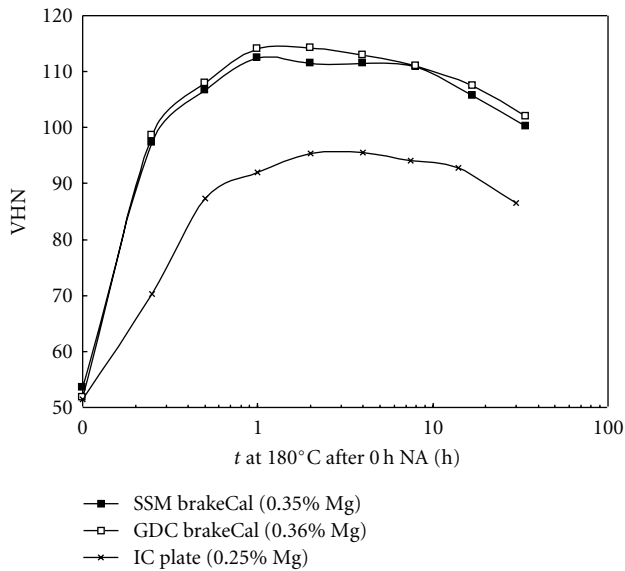


FIGURE 4: Artificial aging curves at 180°C for alloy A356 cast using different casting techniques (after 0 h prior natural aging time).

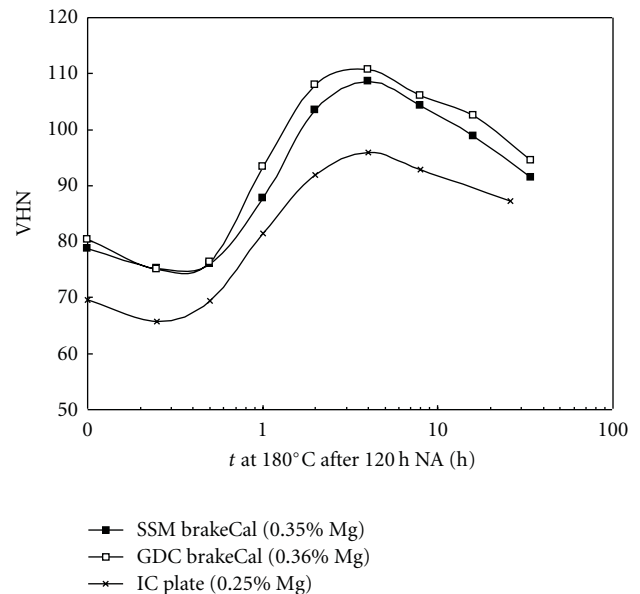


FIGURE 5: Artificial aging curves at 180°C for alloy A356 cast using different casting techniques (after 120 h prior natural aging time).

hardness values of SSM-HPDC plates [9–11] and brake calipers (Figures 4 and 5), GDC brake calipers (Figures 4 and 5), and IC plates (Figures 4 and 5). Globular and dendritic microstructures are, therefore, included as well as variations in natural aging time periods. It is seen

that a strong linear correlation between T6 hardness and wt% Mg exists (especially for the low Mg-concentration range), regardless of the casting technique used (globular or dendritic microstructure) or natural aging time period employed before artificial aging (0 or 120 h NA). This is

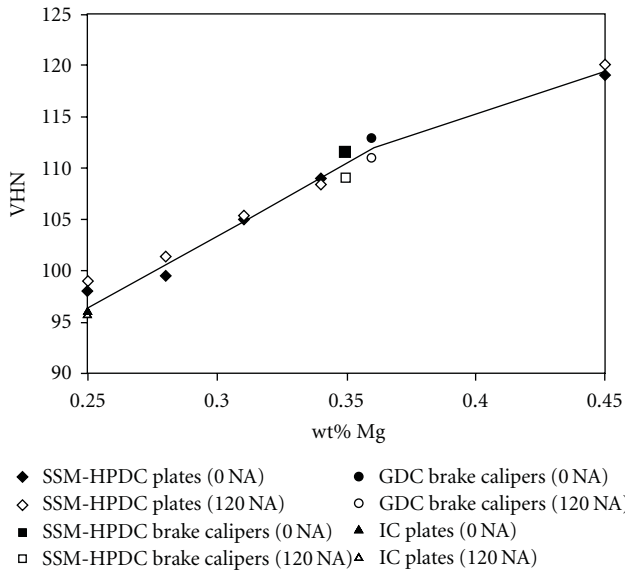


FIGURE 6: T6 (540°C-1 h, 0 or 120 h NA, 180°C-4 h) hardness values as a function of the Mg-content of A356 produced using different casting techniques.

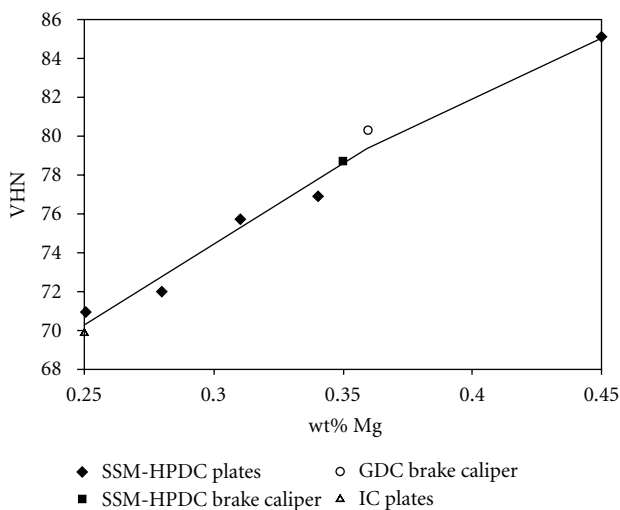


FIGURE 7: T4 (540°C-1 h, 120 h NA) hardness values as a function of the Mg-content of A356 produced using different casting techniques.

a noteworthy finding, given the appreciable differences in microstructures obtained using the different casting techniques (Figures 2 and 3). This suggests that the Mg-content primarily controls the hardening response by controlling the volume fraction of strengthening  $\beta''$ -Mg<sub>5</sub>Si<sub>6</sub> in this alloy. Note that A356 contains an excess of Si that is required to form stoichiometric Mg<sub>2</sub>Si or the strengthening Mg<sub>5</sub>Si<sub>6</sub> [23]. It also reinforces the earlier observation that the effects of any natural aging preceding artificial aging can be removed by a 4-hour artificial aging treatment at 180°C in both dendritic and globular A356. The lower increase in hardness for the high Mg-concentration range in Figure 6 has been studied in

detail by the authors before [20]. It was shown that the Mg-containing  $\pi$ -phase (Al<sub>8</sub>FeMg<sub>3</sub>Si<sub>6</sub>) cannot be fully removed by solution treatment at 540°C in alloys which contain more than ~0.4% Mg. The  $\pi$ -phase removes the strengthening solute Mg from solid solution and this has a detrimental effect on the aging behaviour.

Figure 7 compares the hardness values of A356-T4 (540°C-1 h, 120 h NA) as a function of the Mg-content of the castings. Figures 6 and 7 include hardness values of SSM-HPDC plates [9–11] and brake calipers (Figure 5), GDC brake calipers (Figure 5), and IC plates (Figure 5). The T4 hardness values in Figure 5 are the data points at  $t = 0$  h (i.e., before the start of artificial aging). A strong linear correlation between T4 hardness and wt% Mg is also found, regardless of the casting technique used. The lower increase in hardness at higher Mg-levels in Figure 7 is once again due to the  $\pi$ -phase [20].

#### 4. Conclusions

- (1) The natural aging (T4) and artificial aging (T6) responses of alloy A356 are not influenced by having a globular or dendritic microstructure.
- (2) The influence of any natural aging prior to artificial aging can be removed by an artificial aging treatment of 4 hours at 180°C in both dendritic and globular A356.
- (3) A strong linear correlation is found between T6 hardness and wt% Mg of A356, regardless of the casting technique used (globular or dendritic microstructure) or natural aging time period employed before artificial aging (0 or 120 h NA).
- (4) A strong linear correlation is also found between T4 hardness and wt% Mg of A356, regardless of the casting technique used.

#### Acknowledgments

The contributions of U. Curle, D. Wilkins, M. Grobler (SSM-HPDC), P. Malesa, and S. Papo (IC) are gratefully acknowledged.

#### References

- [1] M. C. Flemings and R. A. Martinez, "Principles of microstructural formation in semi-solid metal processing," *Solid State Phenomena*, vol. 116-117, pp. 1–8, 2006.
- [2] O. Lashkari and R. Ghomashchi, "The implication of rheology in semi-solid metal processes: an overview," *Journal of Materials Processing Technology*, vol. 182, no. 1–3, pp. 229–240, 2007.
- [3] H. V. Atkinson, "Modelling the semisolid processing of metallic alloys," *Progress in Materials Science*, vol. 50, no. 3, pp. 341–412, 2005.
- [4] W. L. Winterbottom, "Semi-solid forming applications: high volume automotive products," *Metallurgical Science and Technology*, vol. 18, pp. 5–10, 2000.

- [5] D. Liu, H. V. Atkinson, P. Kapranos, W. Jirattiticharoean, and H. Jones, "Microstructural evolution and tensile mechanical properties of thixoformed high performance aluminium alloys," *Materials Science and Engineering A*, vol. 361, no. 1-2, pp. 213–224, 2003.
- [6] ASM Specialty Handbook, *Aluminium and Aluminium Alloys*, ASM International, Materials Park, Ohio, USA, 1993.
- [7] M. Rosso and M. A. Grande, "Optimization of heat treatment cycles for automotive parts produced by rheocasting process," *Solid State Phenomena*, vol. 116-117, pp. 505–508, 2006.
- [8] B. Dewhirst, D. Apelian, and J. Jorstad, "Effect of artificial aging on microstructure and tensile properties of semi-solid processed A356 castings," *Die Casting Engineer*, vol. 49, no. 3, pp. 38–44, 2005.
- [9] H. Möller, G. Govender, and W. E. Stumpf, "Natural and artificial aging response of semisolid metal processed Al-Si-Mg alloy A356," *International Journal of Cast Metals Research*, vol. 20, no. 6, pp. 340–346, 2007.
- [10] H. Möller, G. Govender, and W. E. Stumpf, "The natural and artificial aging response of semi-solid metal processed alloy A356," *Solid State Phenomena*, vol. 141–143, pp. 737–742, 2008.
- [11] H. Möller, G. Govender, and W. E. Stumpf, "Investigation of the T4 and T6 heat treatment cycles of semi-solid metal processed aluminium alloy A356," *Open Materials Science Journal*, vol. 2, pp. 11–18, 2008.
- [12] H. Möller, G. Govender, and W. E. Stumpf, "Application of shortened heat treatment cycles on A356 automotive brake calipers with respective globular and dendritic microstructures," *Transactions of Nonferrous Metals Society of China*, vol. 20, no. 9, pp. 1780–1785, 2010.
- [13] Y. Birol, "Response to artificial ageing of dendritic and globular Al-7Si-Mg alloys," *Journal of Alloys and Compounds*, vol. 484, no. 1-2, pp. 164–167, 2009.
- [14] Y. Birol, "Effect of solution heat treatment on the age hardening capacity of dendritic and globular AlSi7Mg0.6 alloys," *International Journal of Materials Research*, vol. 101, no. 3, pp. 439–444, 2010.
- [15] E. Sjölander and S. Seifeddine, "The heat treatment of Al-Si-Cu-Mg casting alloys," *Journal of Materials Processing Technology*, vol. 210, pp. 1249–1259, 2010.
- [16] R. Bruwer, J. D. Wilkins, L. H. Ivanchev, P. Rossouw, and O. F. R. A. Damm, "Method of and apparatus for processing of semi-solid metal alloys," US7368690 Patent, 2008.
- [17] U. A. Curle, J. D. Wilkins, and G. Govender, "Industrial Semi-Solid Rheocasting of Aluminum A356 Brake Calipers," *Advances in Materials Science and Engineering*, vol. 2011, Article ID 195406, p. 5, 2011.
- [18] J. A. Taylor, D. H. StJohn, and M. J. Couper, "Solution treatment effects in Al-Si-Mg casting alloys, part 2," *Aluminum Transactions*, vol. 4-5, pp. 111–124, 2001.
- [19] B. I. Jung, C. H. Jung, T. K. Han, and Y. H. Kim, "Electromagnetic stirring and Sr modification in A356 alloy," *Journal of Materials Processing Technology*, vol. 111, no. 1–3, pp. 69–73, 2001.
- [20] H. Möller, G. Govender, W. E. Stumpf, and P. C. Pistorius, "Comparison of heat treatment response of semisolid metal processed alloys A356 and F357," *International Journal of Cast Metals Research*, vol. 23, no. 1, pp. 37–43, 2010.
- [21] C. D. Marioara, S. J. Andersen, J. Jansen, and H. W. Zandbergen, "The influence of temperature and storage time at RT on nucleation of the  $\beta''$  phase in a 6082 Al-Mg-Si alloy," *Acta Materialia*, vol. 51, no. 3, pp. 789–796, 2003.
- [22] A. K. Gupta, D. J. Lloyd, and S. A. Court, "Precipitation hardening processes in an alloy Al-0.4%Mg-1.3%Si-0.25%Fe aluminum alloy," *Materials Science and Engineering A*, vol. 301, no. 2, pp. 140–146, 2001.
- [23] A. K. Gupta, D. J. Lloyd, and S. A. Court, "Precipitation hardening in Al-Mg-Si alloys with and without excess Si," *Materials Science and Engineering A*, vol. 316, no. 1-2, pp. 11–17, 2001.